

Structure and Grain Coarsening During the Processing of Engineering Ceramics

(NASA-TM-100235) STRUCTURE AND GRAIN
COARSENING DURING THE PROCESSING OF
ENGINEERING CERAMICS Ph.D. Thesis - Leeds
Univ., United Kingdom (NASA) 178 p Avail:
NTIS HC A09/MF A01

N88-11838

Unclas
CSCL 11B G3/27 0107555

Nancy J. Shaw
Lewis Research Center
Cleveland, Ohio

November 1987

NASA

CONTENTS

	<u>Page</u>
Symbols and Abbreviations	vi
CHAPTER 1 INTRODUCTION.....	1
CHAPTER 2 LITERATURE REVIEW.....	4
2.1 Sintering.....	4
2.2 Solid State Sintering.....	5
2.2.1 Driving Force.....	5
2.2.2 Sintering Stages.....	13
2.2.2.1 Initial Stage.....	15
2.2.2.2 Intermediate Stage.....	22
2.2.2.3 Final Stage.....	26
2.2.3 Sintering Diagrams.....	28
2.3 Grain Growth.....	30
2.3.1 In Fully Dense Ceramics.....	31
2.3.1.1 Impurity Drag.....	32
2.3.1.2 In the Presence of Inclusions.....	33
2.3.2 In Porous Ceramics.....	35
2.3.2.1 "Spherical" Pores.....	35
2.3.2.2 During Initial Sintering.....	37
2.3.3 Abnormal Grain Growth.....	39
2.4 Simultaneous Densification and Coarsening.....	43
2.4.1 Densification/Coarsening Ratio.....	45

	<u>Page</u>
2.4.1.1 Cannon and Yan Model.....	45
2.4.1.2 Burke, Lay and Prochazka Model.....	49
2.4.2 Surface Area Reduction.....	52
2.5 Stereology.....	59
2.6 Systems to be Investigated.....	59
2.6.1 Al_2O_3 - MgO	60
2.6.2 Y_2O_3 - MgO	61
2.6.3 SiC - C - B	63
CHAPTER 3 EXPERIMENTAL PROCEDURES.....	66
3.1 Powder Preparation.....	66
3.1.1 Alumina.....	66
3.1.2 Yttria.....	67
3.1.3 Silicon Carbide.....	67
3.2 Annealed Powders.....	70
3.3 Transmission Electron Microscopy.....	72
3.4 Sintering.....	72
3.4.1 Alumina.....	72
3.4.2 Yttria.....	73
3.4.3 Silicon Carbide.....	73
3.5 Density Measurement.....	73
3.6 BET Surface Area Measurement.....	74
3.7 Specimen Polishing.....	75
3.7.1 Alumina.....	76
3.7.2 Yttria.....	76
3.7.3 Silicon Carbide.....	76
3.8 Etching.....	77
3.8.1 Alumina and Yttria.....	77

	<u>Page</u>
3.8.2 Silicon Carbide.....	77
3.9 Scanning Electron Microscopy.....	78
3.10 Stereology.....	78
3.10.1 Volume Fraction.....	79
3.10.2 Surface Density.....	82
3.10.3 Shape Factor.....	83
3.10.4 Triple Lines.....	83
3.10.5 Mean Linear Intercept.....	86
CHAPTER 4 EXPERIMENTAL RESULTS: ALUMINA.....	89
4.1 Sintering.....	89
4.1.1 Density.....	89
4.1.2 Grain Shape Factor.....	89
4.2 Surface Area vs. Density Diagrams.....	91
4.2.1 Surface Area Measurement.....	91
4.2.1.1 Surface Area vs. Density Diagram by BET.....	91
4.2.1.2 Surface Area vs. Density Diagram by Stereology.....	94
4.2.1.3 Comparison of Surface Area vs. Density Diagrams.....	94
4.2.2 Grain Boundary Area vs. Density Diagram.....	94
4.3 Additional Stereological Evaluation.....	98
4.3.1 Length of Triple Lines.....	98
4.3.1.1 Solid-Solid-Pore Triple Lines.....	98
4.3.1.2 Solid-Solid-Solid Triple Lines.....	101
4.3.2 Mean Linear Intercept.....	101
4.3.2.1 Mean Pore Intercept.....	101

	<u>Page</u>
4.3.2.2 Mean Grain Intercept.....	104
CHAPTER 5 DISCUSSION: ALUMINA.....	106
5.1 Effect of MgO on the Densification:Coarsening Ratio.....	106
5.2 Effect of MgO on Coarsening in Al_2O_3	108
5.3 A Model for Grain Boundary Interactions.....	110
5.3.1 Effect of the Two Types of Grain Boundaries on Microstructural Change.....	112
5.3.2 Relationship Between Grain Size and Pore Size.....	116
5.4 Conclusions Regarding the Effects of MgO on the Sintering of Al_2O_3	118
CHAPTER 6 RESULTS AND DISCUSSION: YTTRIA.....	120
6.1 Annealed Powders.....	120
6.2 Sintered Compacts.....	125
6.2.1 Sintered Densities.....	125
6.2.2 Surface Area vs. Density Diagram by BET.....	127
6.2.3 Etching.....	127
6.2.4 Surface Area vs. Density Diagram by Stereology.....	130
6.2.5 Grain Boundary Area vs. Density Diagram.....	134
6.2.6 Triple Lines.....	134
6.3 Conclusions Regarding the Effects of MgO on the Sintering of Y_2O_3	134
CHAPTETR 7 RESULTS AND DISCUSSION: SILICON CARBIDE.....	137
7.1 Sintering.....	137
7.2 Surface Area vs. Density Diagrams.....	139
7.2.1 Surface Area Measured by BET.....	139

	<u>Page</u>
7.2.2 Surface Area Measurement by Stereology.....	144
7.2.2.1 Pore/Solid Surface Area.....	144
7.2.2.2 Comparison of Surface Area vs. Density Diagrams.....	147
7.2.2.3 Grain Boundary Area vs. Density Diagram.....	147
7.3 Evaluation of Dihedral Angles.....	153
7.4 Conclusions Regarding SiC.....	153
CHAPTER 8 CONCLUSIONS.....	156
REFERENCES.....	159

SYMBOLS AND ABBREVIATIONS

a	particle radius (m)
b	magnitude of Burgers vector (m)
BET	Brunauer, Emmett and Teller method of surface area measurement
C	mean curvature (m^{-1})
C_o	bulk concentration (atoms m^{-3})
C (r)	concentration under surface with radius of curvature r (vacancies m^{-3})
C_∞	concentration under a planar surface (vacancies m^{-3})
D	diffusion coefficient ($\text{m}^2 \text{s}^{-1}$)
D_{gb}	grain boundary diffusion coefficient ($\text{m}^2 \text{s}^{-1}$)
D_{gb}^*	diffusion coefficient across grain boundary ($\text{m}^2 \text{s}^{-1}$)
D_l	lattice diffusion coefficient ($\text{m}^2 \text{s}^{-1}$)
D_s	surface diffusion coefficient ($\text{m}^2 \text{s}^{-1}$)
D_v	vapor diffusion coefficient ($\text{m}^2 \text{s}^{-1}$)
F_b	driving force for grain boundary movement due to curvature (N)
F_p	force exerted on pore by grain boundary (N)
F_s	shape factor
g	shear modulus (GN m^{-2})
G	grain size (diameter) (m)
\bar{G}	mean grain size (m)
G_o	original grain size (m)
G	Gibbs free energy (J mol^{-1})
I_L	number of interceptions of features per unit length of test line
J	flux (atoms $\text{m}^{-2} \text{s}^{-1}$ or vacancies $\text{m}^{-2} \text{s}^{-1}$)

k	Boltzmann constant ($1.38 \times 10^{-23} \text{ J } ^\circ\text{K}^{-1}$)
\bar{L}_3^g	mean grain linear intercept in 3-D space (m)
\bar{L}_3^p	mean pore linear intercept in 3-D space (m)
L_o	original length (m)
L_v^{ssp}	length of solid/solid/pore triple line per unit volume (m^{-1})
L_v^{sss}	length of solid/solid/solid triple line per unit volume (m^{-1})
M_b	grain boundary mobility ($\text{m s}^{-1} \text{ N}^{-1}$)
M_p	pore mobility ($\text{m s}^{-1} \text{ N}^{-1}$)
N	pore density at grain boundary (m^{-2})
N_c	number of interparticle contacts
\bar{p}	mean pore size (diameter) (m)
P	pressure (Pa)
\bar{P}_A	average number of intersections triple line makes with unit area of section plane
r	radius of curvature (m)
R	gas constant ($8.3144 \text{ J } ^\circ\text{K}^{-1} \text{ mole}^{-1}$)
RSE	relative standard error
S	surface area
SEM	scanning electron microscopy
S_m	surface area per unit mass ($\text{m}^2 \text{ g}^{-1}$)
S_o	original surface area
S_v	surface area per unit volume ($\text{m}^2 \text{ m}^{-3} = \text{m}^{-1}$)
S_v^{gb}	grain boundary area per unit volume (m^{-1})
S_v^p	pore/solid surface area per unit volume (m^{-1})
t	time (sec., min., hr.)
T	temperature, $^\circ\text{K}$, unless otherwise specified
TEM	transmission electron microscopy
v_b	grain boundary velocity (m s^{-1})

v_p	pore velocity (m s^{-1})
V_m	molar volume (m^3)
V_v	volume fraction
V_v^p	volume fraction porosity
V_v^s	volume fraction solid
x	neck radius (m)
α	drag on grain boundary caused by impurity atoms (N)
γ	solid/vapor surface energy (J m^{-2})
γ_{gb}	grain boundary energy (J m^{-2})
Γ	relative coarsening rate:densification rate ratio
δ	effective width for grain boundary diffusion (m)
ϵ	strain (deformation per unit length)
$\dot{\epsilon}$	strain rate (s^{-1})
ρ	density (kg m^{-3})
ρ_o	original density
ρ_{th}	theoretical density (kg m^{-3})
σ	applied stress (Pa)
ω	effective width for surface diffusion (m)
Ω	volume occupied by a vacancy (m^3)

CHAPTER 1

INTRODUCTION

Ceramic products are usually made by forming a mixture of the ceramic powder and any additives and binders into the desired shape and applying heat (sintering), and possibly pressure, until a hard, dense material is obtained.* The physical and mechanical properties of the finished product are highly dependent upon the characteristics of the starting powder and the details of the processing procedure. This is especially significant in the case of structural and other engineering ceramics where their use requires specific, reproducible, properties.

Two processes occur simultaneously during the sintering of a ceramic powder compact: densification and coarsening (or grain growth). Both processes have as their driving force the reduction of the excess free surface energy of the powder particles. Several different mechanisms of atom transport, operating concurrently or consecutively, may be responsible for the two processes.

The usual aim of sintering is to produce a product as near to theoretical density as possible with a grain size that is optimum for the intended use. Thus most sintering research has been concerned with the effect of changes in the processing variables, i.e., time, temperature, composition and pressure, on the densification rate and the final density and grain size. The question of additive selection and use (an aspect of the composition variable) has in particular been studied because of the several instances where technologically valuable additions have been found. Algebraic, geometric and topological models have been proposed and refined in attempts to determine the mechanism, or mechanisms, responsible

* No references are included in this Introduction because all topics are covered in more detail in later sections.

for densification under defined processing conditions. These efforts have met with varying degrees of success. For instance, most of the geometric models have been criticized as being far too simplistic to apply to very complex, actual powder systems, and yet, they have led to advances in the understanding of the sintering behavior of real powders. For example, it has been determined that for the conditions commonly used in ceramic processing, the densification of Al_2O_3 is controlled by the movement of aluminum atoms through the crystal lattice. Very high density, translucent Al_2O_3 with a fine, uniform grain size can be produced by the addition of ~ 0.25 wt.% MgO , but the mechanism by which MgO acts is still uncertain.

Recently, it has become apparent that more attention must be paid to the coarsening processes during sintering. Early coarsening may severely limit the final attainable density, as with reaction bonded Si_3N_4 . Grain growth at high density, as in Al_2O_3 , will determine the grain size and the size and distribution of any remaining porosity and will influence the eventual material properties. For some applications, for example, bone replacement implants, the requirement is not for very high density, but for strength with porosity carefully controlled as to size and location. For such applications, therefore, the control of coarsening is a key part in the processing.

Little attention has been paid to early coarsening because for many ceramics it is not a serious problem. Even when it is of concern, the transport mechanisms are very difficult to measure and are highly affected by the physical and chemical properties of the particle surfaces. The submicron size of most ceramic powders makes observation of changes during the early stages of sintering extremely difficult.

Grain growth at high densities has been seen to be important in determining the final density and microstructure of many ceramics and has, thus, been the subject of much theoretical and experimental work. Observation of microstruc-

tural change is easier as the grain size increases, but the geometry is still complex and determining the mechanisms controlling those changes is not easy.

In the light of the interest in the coarsening behavior of a ceramic during sintering, the aim of this project is to evaluate possible techniques for measuring coarsening in terms of their sensitivity to processing variables, the usefulness of the information provided, the particular advantages or disadvantages of the experimental procedures and the correlation with model systems. The methods of primary interest are those involving measurement of surface area changes. Three materials systems were studied:

1. Al₂O₃, pure and doped with MgO. MgO, added in amounts below the solid solubility limit, is known to increase lattice diffusion and to decrease surface diffusion in Al₂O₃. These effects are expected, respectively, to increase densification and to reduce coarsening.
2. Y₂O₃, pure and doped with MgO. MgO is known to enhance densification of Y₂O₃, but the controlling mechanisms and effect on coarsening are unknown, thus providing a test case for the usefulness of the evaluation techniques on a relatively unknown system.
3. SiC, pure and doped with C and B. Pure SiC coarsens, but does not densify, while SiC doped with C and B densifies to near theoretical density. These systems, therefore, exemplify the extremes in coarsening and densification behavior.

CHAPTER 2

LITERATURE REVIEW

2.1 SINTERING

Sintering⁽¹⁻¹⁰⁾ can be described as a process in which a compact of a crystalline or non-crystalline powder is heat-treated to form a single, coherent solid. In general, three types of sintering processes are important to the production of ceramics:

i. Vittrification - heat treatment which produces enough viscous liquid at the firing temperature to fill completely the porous spaces in the original powder compact. This process is relatively inexpensive and is of particular importance in the production of porcelain and clay-based ceramics.

ii. Liquid phase sintering - the composition is such that enough liquid forms at the firing temperature to allow easy rearrangement of the particles, but not enough to fill the initial porosity; subsequent solution and reprecipitation of the solid in the liquid phase then allows reshaping of the particles and formation of a dense body. This method is often effective and reasonably inexpensive, but the resulting grain boundary phase may be detrimental to the high temperature mechanical properties (e.g., creep resistance).

iii. Solid state sintering - all constituents of the compact remain solid during the entire process; all densification is achieved by change in grain shape. Sintering aids that will not form a liquid may be added in amounts ranging from a few hundred parts per million to over 20%. This method is preferred for the production of technical ceramics with good mechanical, electronic or optical properties,

particularly where optimum high temperature properties are required.

The important variables in the sintering process are:

1. the processing temperature,
2. the time spent at each stage of the process,
3. the particle size and size distribution of the ceramic powder,
4. the composition of the system, including additives and atmosphere,
5. the processing pressure for cases where hot pressing or a controlled atmosphere is used.

The remainder of this section will be concerned with solid state sintering, which has been chosen as the basis for the present work in view of the fact that it has the greatest interest for the production of technical ceramics; it is also the one for which models and mechanisms have been most widely considered.

2.2 SOLID STATE SINTERING

2.2.1 Driving Force

The primary driving force for sintering is reduction in the free surface energy of the system. This is accomplished by reducing the area of the surfaces and interfaces of the compact: this can be achieved by a combination of two alternative processes (Figure 1), namely, conversion of many small particles into fewer, larger ones (coarsening), or replacement of the gas/solid interface by a lower energy solid/solid interface (densification). Thus the microstructural changes that occur in sintering are brought about by the combined effects of coarsening and densification processes.

Figure 2a represents a portion of the starting powder compact. To densify such a compact, material must be moved from some part of the particles to the

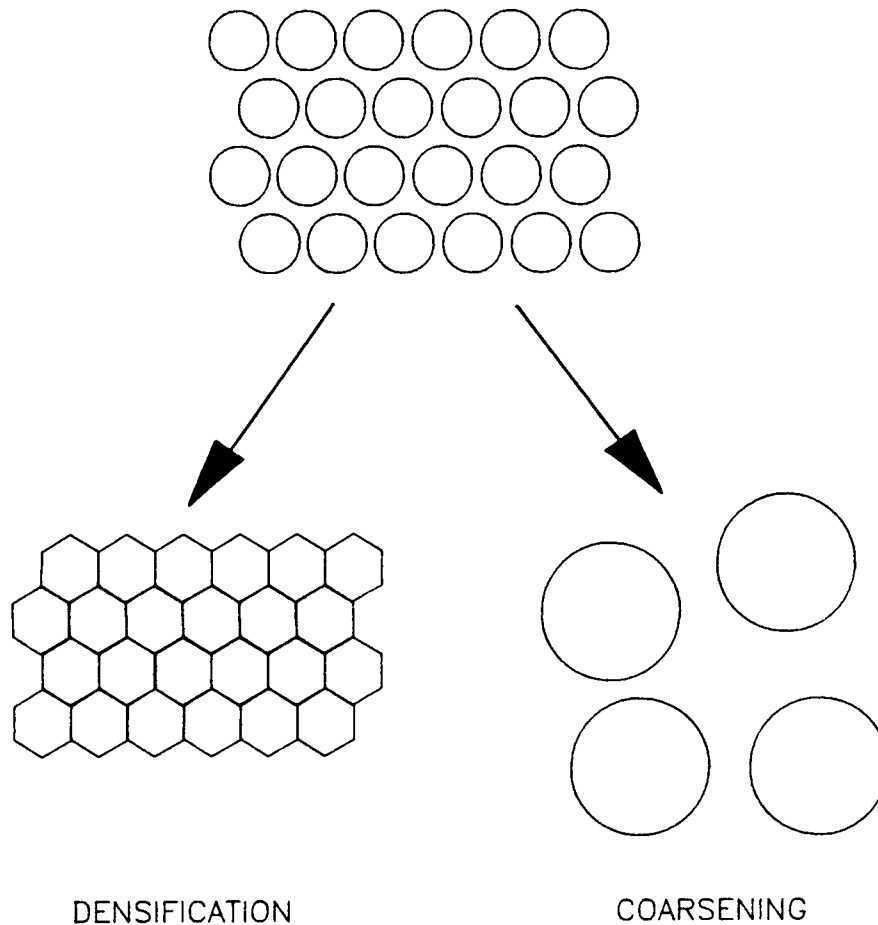


Figure 1. Sintering is a process of microstructural change which involves contributions from two ideal subprocesses: densification (replacement of free surface energy by grain boundary energy) and coarsening (reduction of extent of free surface or grain boundary energy); the relative contributions of the two subprocesses occurring depend on the processing variables, i.e., T , t , composition and particle size.

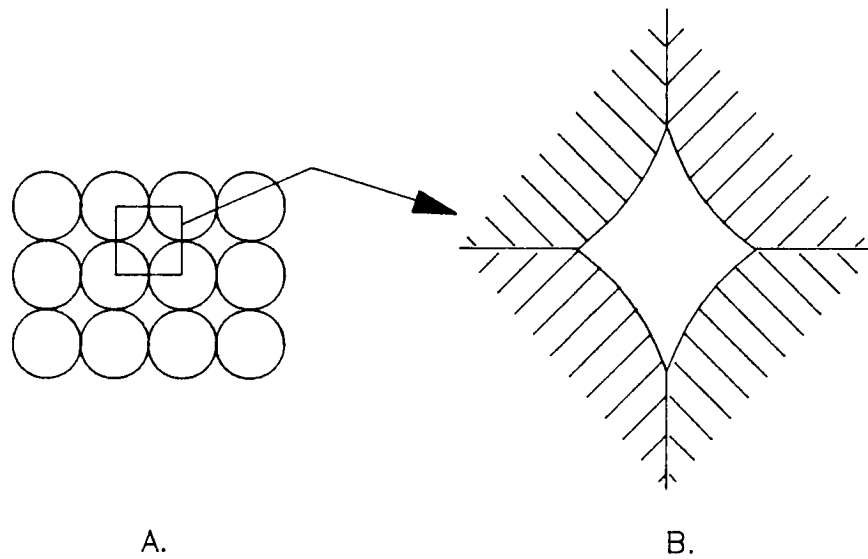


Figure 2. The driving force for sintering, which in a macroscopic view of the sample (A), can be seen to be the large quantity of available surface energy, acts at the atomic level (B) by way of the curvature differences present in the structure. These curvature differences are, therefore, the local mechanism by which the reduction of the thermodynamic driving energy is brought about.

pore space between them. In solid state sintering there is no liquid phase to aid densification by filling the voids or by providing an easy transport path; all of the constituents remain either in the solid state or as a species in the vapor phase.

The driving force for sintering (the reduction in excess surface free energy) is translated into a driving force acting at the atomic level (and thus bringing about atomic diffusion) by means of the curvature differences which necessarily occur in different parts of the three-dimensional compact (Figure 2). These curvature differences create vacancy concentration differences and thus control of the direction of matter transport. The relationship which links surface energy, curvature and concentration difference is the Gibbs-Thomson equation:

$$C(r) = C_{\infty} \exp \left(\frac{2 \gamma \Omega}{r k T} \right) \quad (1)$$

where $C(r)$ is the vacancy concentration under a surface which has a radius of curvature r , C_{∞} is the vacancy concentration under a plane, γ is the surface energy and Ω is the volume occupied by a vacancy. The radius r is positive when it is within the "dense" phase of the species being considered (within the pore for vacancies and within the solid for atoms) and negative when it is within the dispersed phase (Figure 3).

In the powder compact the vacancy concentration will be different at regions of different curvature, resulting in vacancy gradients and, thus, vacancy flow. The rate of mass transport is described by Fick's first law of diffusion:

$$J = -D \frac{dc}{dx} \quad (2)$$

where J is the vacancy flux, D the diffusion coefficient and $\frac{dc}{dx}$ the concentration gradient. During the initial stages of sintering there will be a net flow of vacancies from the neck forming between particles, a region of large negative curvature, as shown in Figure 4. This flow of vacancies is exactly equivalent to a

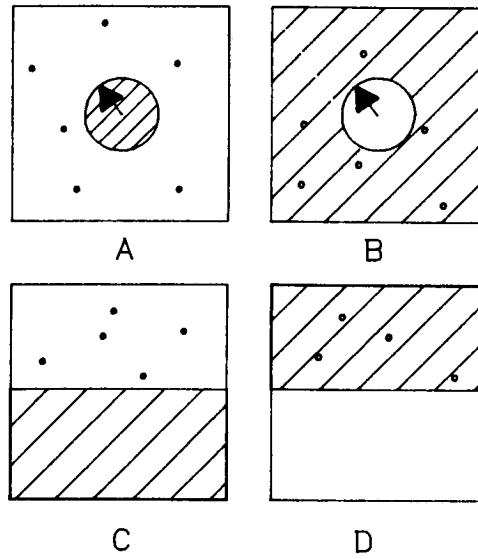


Figure 3. In the equation $C(r) = C_{\infty} \exp\left(\frac{2\gamma\Omega}{rRT}\right)$ r is positive when it occurs in the "condensed" phase, i.e., (A) condensed gas (solid) for the gas pressure case (where gas atoms are the species whose concentration is being considered) or (B) dense vacancies (vacuum) for the vacancy concentration case. In both cases, the concentration in the dispersed phase is greater for a positive curvature than for a planar curvature, (C) and (D). Note that the Gibbs-Thomson equation is applicable to the vacuum/vacancy couple since the mass does not occur in the equation.

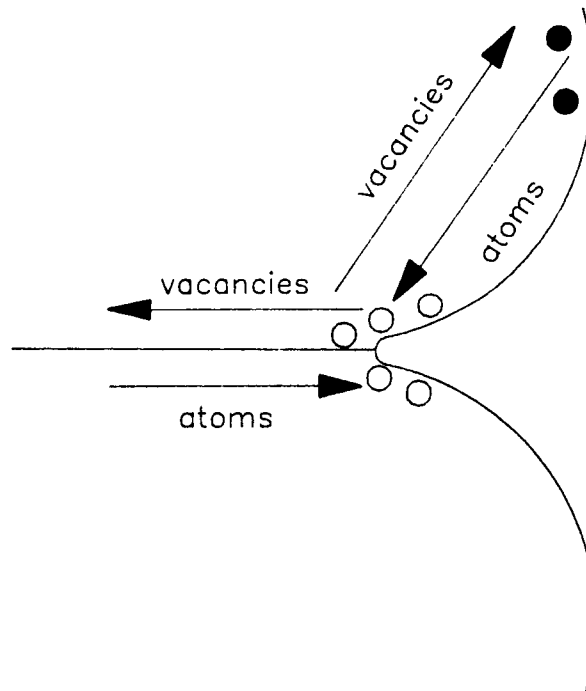


Figure 4. The Gibbs-Thomson equation applies to concentrations of dilute species and is therefore applied to vacancies which are in dilute solution in the solid rather than to the atoms themselves. Once the flow equations are known in terms of the vacancies, the equivalent flow in terms of atoms follows directly.

flow of atoms in the opposite direction, thus resulting in neck formation.

It is often helpful in the case of ceramics to consider an alternative representation for the driving force for atom movement, namely that a flow of atoms stems from the normal pressure differences* which occur in regions of the solid close to surfaces of different curvature. This representation leads to a diffusion flux which can be written as:

$$J = - \frac{D}{kT} \frac{dP}{dx} \quad (3)$$

with $\frac{dP}{dx}$ being the pressure gradient. Atoms will tend to move from regions of high normal pressure to regions of low normal pressure as in Figure 5. This concept avoids reliance on atom movement by vacancies; it therefore also applies to systems in which atoms move by other defect mechanisms. These two approaches are physically equivalent and it is thus a matter of convenience which is preferred.

The approach which links atom movement to pressure differences has the benefit of describing directly the diffusional deformation of dense polycrystalline materials caused by an applied stress (creep);⁽¹¹⁻¹³⁾ sintering rate equations for ceramics have been developed based on the assumption that behavior caused by pressure (curvature) differences during sintering is similar to diffusional creep behavior.⁽¹³⁾ The rate of deformation caused by an applied stress is given by the general equation:⁽¹⁴⁾

$$\dot{\epsilon} = \frac{AD}{kT} \left(\frac{b}{G} \right)^m \left(\frac{\sigma}{g} \right)^n \quad (4)$$

where A is a dimensionless constant, D the appropriate diffusion coefficient, g

* Movement of atoms and associated displacement of interfaces allows the pressure normal to the interface to do work.

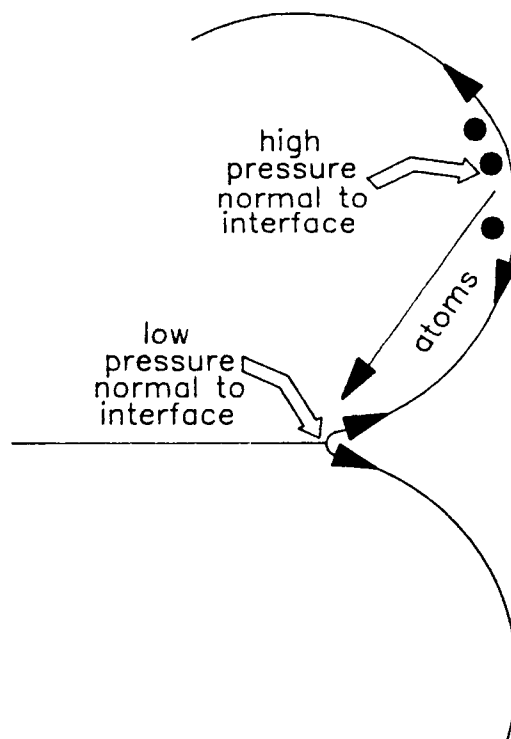


Figure 5. Surface energy forces create regions of different pressure under different curvatures. Atoms will tend to flow from regions of high pressure to regions of low pressure.

the shear modulus, b the magnitude of the Burgers vector, G the grain size, σ the applied stress and m and n are constants dependent upon the transport mechanism. Low temperature (in relation to the melting point) creep of metals is usually controlled by dislocation movement (glide) because their structures contain sufficient active slip systems and have small Peierl's stresses (the force needed to bring about dislocation movement).⁽¹⁵⁾ Deformation can also be controlled by dislocation climb, a process requiring vacancy diffusion. At high temperatures, deformation in metals is usually controlled by diffusional creep mechanisms not involving dislocation movement. In ceramics, however, diffusional creep (Figure 6) may be the dominant mechanism under most processing conditions⁽¹⁶⁾ owing to the small number of slip planes, to the high Peierl's stresses and to the need to move stoichiometric amounts of the different atomic species contained in the material, i.e., both anions and cations for an ionic compound.

2.2.2. Sintering Stages

Investigation of sintering behavior has commonly been simplified by considering the densification to take place in stages. The sintering process is usually modeled in three stages:

- i. Initial - the individual particles of the green compact, which remain readily identifiable, are bonded together by the growth of necks between the particles and a grain boundary forms at the junction of the two particles.
- ii. Intermediate - characterized by interconnected networks of particles and pores.
- iii. Final - the structure is composed of space-filling polyhedra and isolated pores.

There are no clear-cut divisions between the three stages. Swinkels and Ashby,⁽¹⁷⁾ in fact, omit the intermediate stage altogether from their model,

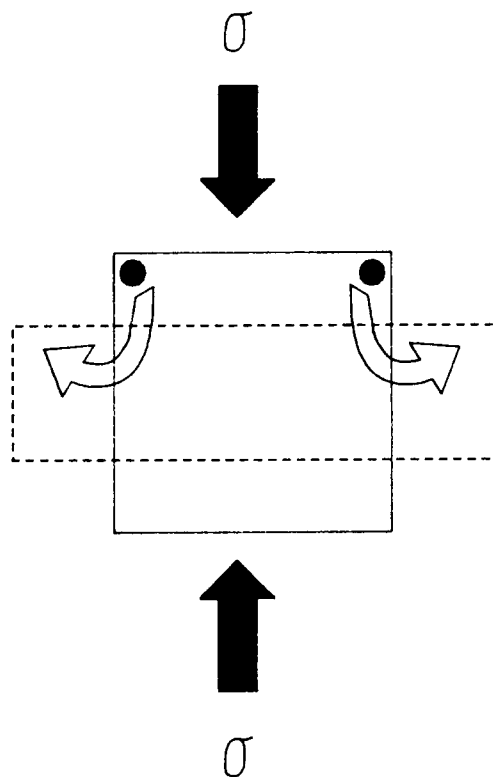


Figure 6. Deformation of a solid caused by atom flow under an applied stress (diffusional creep). The diagram shows one grain in a polycrystalline structure; all other grains behave in a comparable manner.

simply allowing a transition between the equations for behavior during the initial and final stages. Because of the geometric complexities of the intermediate stage, most of the sintering models and rate equations that have been developed are for the initial and final stages.

2.2.2.1 Initial Stage

During the initial stage,⁽¹⁸⁾ the individual particles of the green compact, which remain readily identifiable, are bonded together by the growth of necks between the particles and the formation of a grain boundary at the junction of the two particles (Figures 7 and 8). The initial stage ends when the growing necks begin to impinge on each other or at ~5% shrinkage (if shrinkage occurs).

Kuczynski, in his now-classic 1949 paper,⁽¹⁹⁾ was among the first to consider the use of kinetic analysis to identify the mechanism by which metal powders join together when heated. He assumed four possible mechanisms: viscous or plastic flow, evaporation and condensation, volume diffusion (not differentiating between grain boundary and lattice diffusion) and surface diffusion. Using the model (Figure 9) of a sphere sintering to a plate, he developed neck growth equations of the form:

$$x^m = At \quad (5)$$

where x is the neck radius and A is a constant which includes the surface energy, the atomic volume, the Boltzman constant, the absolute temperature, and the appropriate coefficient of diffusion. His analysis resulted in the following relationships between the radius of the growing neck and time:

viscous or plastic flow	$x^2 \propto t$
evaporation/condensation	$x^3 \propto t$
volume diffusion	$x^5 \propto t$
surface diffusion	$x^7 \propto t$

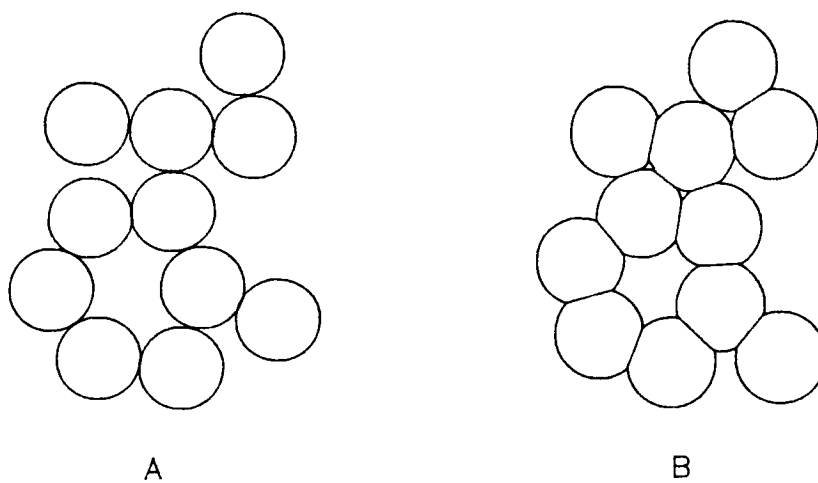


Figure 7. (A) Green powder compact. (B) Grain boundaries are formed at contact points between particles in the compact during initial stage sintering, reducing the total energy of the system.

ORIGINAL PAGE IS
OF POOR QUALITY

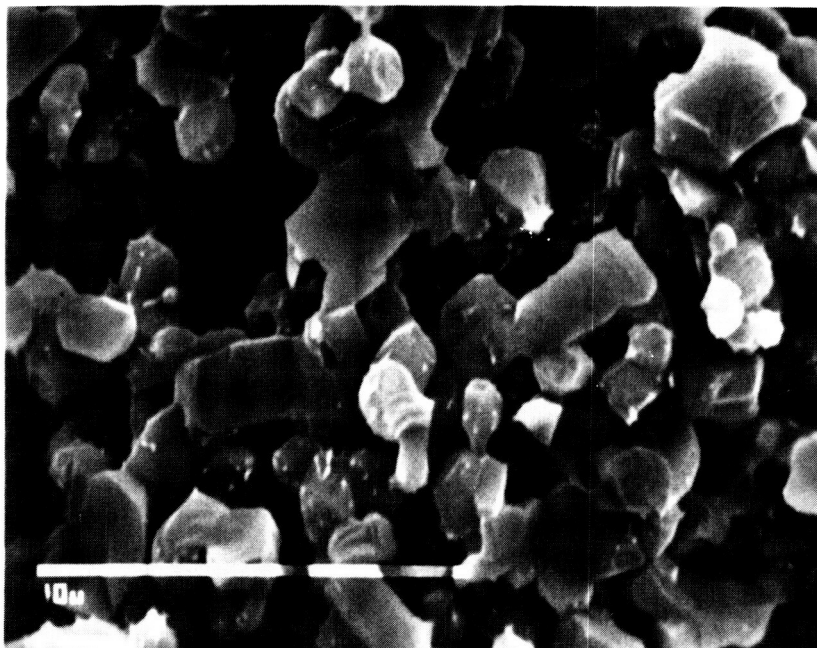


Figure 8. An example of a microstructure during the initial stage of sintering. Necks have formed at contact points, but the original particles are still clearly defined. (SiC sintered in Ar for 60 min. at 2050°C.

He attempted to verify his model by sintering copper and silver spheres ($<10\ \mu\text{m}$ to $350\ \mu\text{m}$) to plates and measuring the necks. Plots of $\log \frac{x}{a}$ vs. $\log t$ for the larger particles had inverse slopes of 4.5 to 5.4 from which he concluded that the predominant sintering mechanism was volume diffusion, while for particles of less than $10\ \mu\text{m}$ at low temperatures, the predominant mechanism appeared to be surface diffusion. He assumed that, in the case of two mechanisms operating simultaneously, the volume of material moved by each mechanism would be additive; however, he apparently did not consider multiple mechanisms to play a significant role in any of these experiments.

Kuczynski was concerned only with the mechanism of neck growth and did not consider either densification or grain growth in his work. Although we now know that the determination of "the sintering mechanism" is not straightforward on the basis of the Kuczynski approach, his work has proved to be the cornerstone for all subsequent attempts to elucidate sintering mechanisms.

Kingery and Berg⁽²⁰⁾ proposed an analysis for two alternative two-sphere models (Figure 10) for neck growth: one considering only neck growth, and a second allowing center-to-center approach, or shrinkage. They considered viscous flow, evaporation/condensation, and diffusion as possible transport mechanisms. Their analysis considered volume diffusion with the neck as the vacancy source and several possible sinks. An advance in understanding came from the suggestion that not only could material flow to the neck region along the particle surface or from the surface through the lattice, but that if the centers of the particles were to approach (Figure 10B), a grain boundary between them would also be a vacancy sink with the nearby lattice as the diffusion path.

They realized that simultaneous sintering mechanisms and similar time dependencies for surface and volume diffusion could make determination of the sintering mechanism difficult. Additional guidance in differentiating mechanisms could come from considering Herring's scaling laws,⁽²¹⁾ the temperature depen-

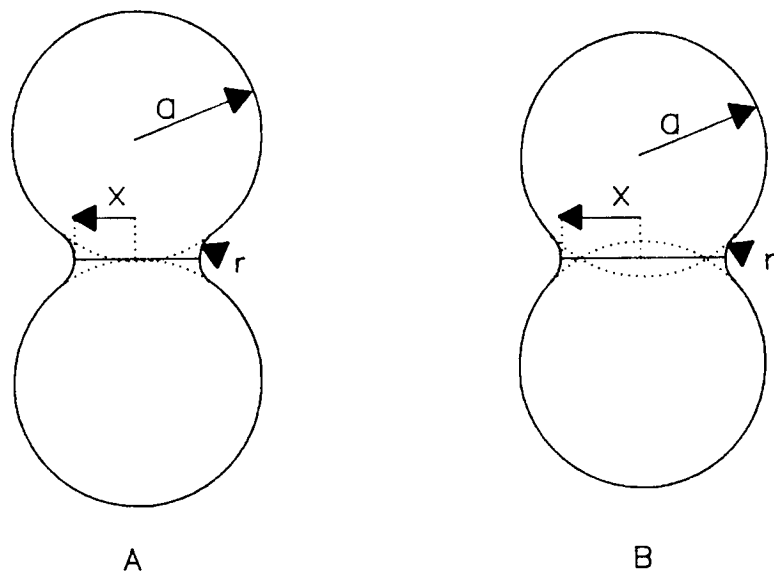


Figure 10. Two-sphere models used to derive initial stage neck growth equations. (A) without densification (B) with densification. (After Kingery and Berg, Ref. 20)

dence of the mechanisms, and calculated values of vapor pressure, diffusion coefficients, etc. Observation of the center-to-center approach would also be important since neither surface diffusion nor evaporation/condensation result in shrinkage.

For the case of no center-to-center approach (Figure 10A), assuming volume diffusion of vacancies from the neck to the particle surface, they calculated the change in volume of each spherical particle as the neck was filled. They assumed that this slight reduction in particle size would result in a small amount of shrinkage of a chain of spherical particles, the exact amount being dependent upon the number of interparticle contacts, N_c .

$$\frac{\Delta L}{L_0} = - \frac{N_c}{8} \left(\frac{40 \gamma \Omega D_l}{r^3 k T} \right)^{4/5} t^{4/5} \quad (6)$$

where ΔL is the length change and L_0 the original length. They expected this equation to be applicable for shrinkages up to $\sim 2\%$. Case B (Figure 10), involving center-to-center approach of the particles, of course, gives considerably greater shrinkage, resulting in an equation with different constants and exponents of $2/5$.

They investigated the three mechanisms by heating rows of touching spheres of glass, NaCl and copper. Results were fairly clear on the mechanism of neck growth for each: viscous flow, evaporation/condensation and volume diffusion, respectively. The first indication of potential problems with extrapolation of these simple models to more complex systems came with the widely varying behavior they observed in groups of Al_2O_3 or ZrO_2 spheres and between loose and pressed powder compacts of these two oxides.

Coble,⁽¹⁸⁾ German and Munir⁽²²⁾ and others have extended and refined such models, all using slight variations of a fundamentally similar geometry. Measurements of neck growth in pairs of relatively large ($100 \mu m - 1/8$ in.) metal and ceramic spheres often fit these equations well. Efforts to extend these

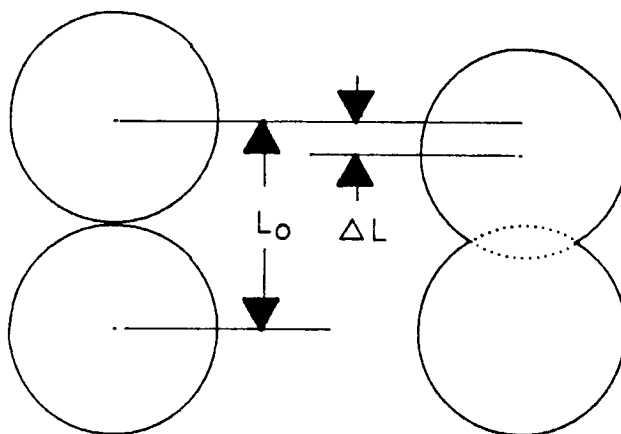
models to the shrinkage of powder compacts (Figure 11) by deriving equations similar to Equation 6, with ΔL now the change in length of the powder compact, have met with less success.⁽²³⁾ The simple models are limited to the early stages of sintering (for $\frac{x}{a} < 0.3$) and are inappropriate as a means to analyze the extreme densification of a powder compact (which, however, has not prevented some researchers from trying). Exner *et al.*⁽²⁴⁾ have shown that inhomogeneities in powder packing will lead to a degree of particle rearrangement that cannot be accounted for by the two-sphere models. Johnson⁽²⁵⁾ noted also the unreliability of extending these two-sphere models to compacts of irregularly shaped particles having particle size distributions and packing inhomogeneities.

In addition to the uncertainties involved in extending these simple models far beyond their strict limits of applicability, there is the serious problem of treating simultaneous contributions from several transport mechanisms. This last feature has proved to be the most difficult aspect of using the kinetic model approach. The most common procedure is to assume that the effect of each mechanism on the growth rate can be treated as simply additive.^(19,26,27)

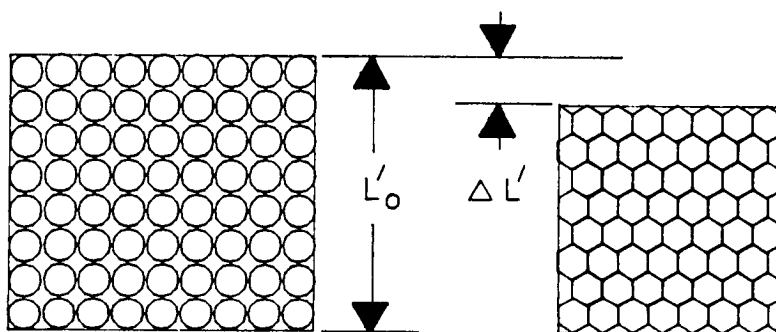
2.2.2.2 Intermediate Stage

The intermediate stage,^(27,28) which lasts until only 5 - 10% porosity remains, is characterized by interconnected networks of polyhedra and pores. The pore network is actually very complex, but in geometric models is considered to be made up of a series of cylinders lying along the three-grain edges (Figure 12). A typical intermediate microstructure is shown in Figure 13.

Coble^(28,29) derived equations to express the change in density, $\Delta\rho$, during intermediate stage sintering by considering the diffusion of atoms from the grain boundary to the adjacent pore either directly along the grain boundary, D_{gb} , or through the nearby lattice, D_l . He modeled the solid as tetrakaidecahedra with cylindrical pores along each three-grain edge (Figure 12). The equations (with A



All basic models calculate $\frac{\Delta L}{L_0}$



Relating this to $\frac{\Delta L'}{L'_0}$ implies no particle rearrangement and that each contact behaves in the ideal manner.

Figure 11

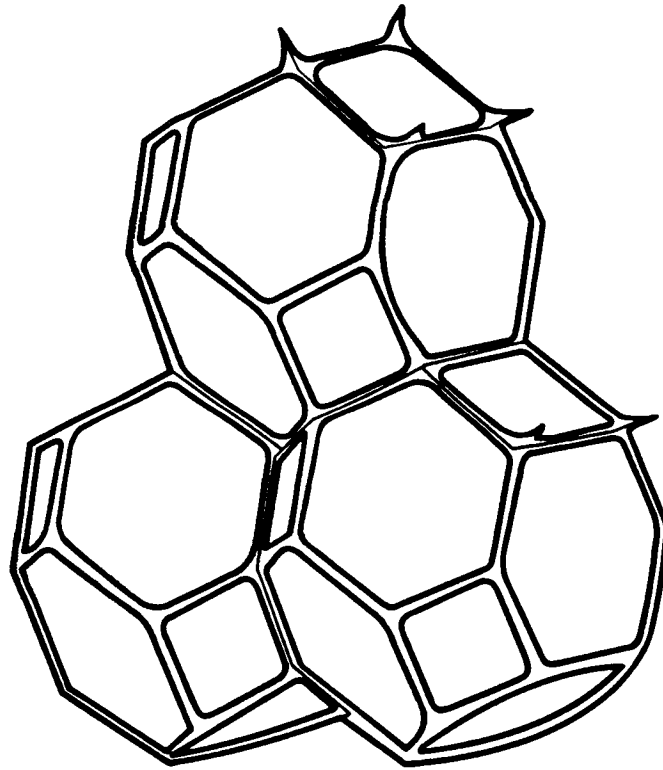


Figure 12. The intermediate stage microstructure is modeled as grains in the shape of space-filling tetrakaidecahedra with pores as channels lying along the grain edges. (After Coble, Ref. 28)

ORIGINAL PAGE IS
OF POOR QUALITY

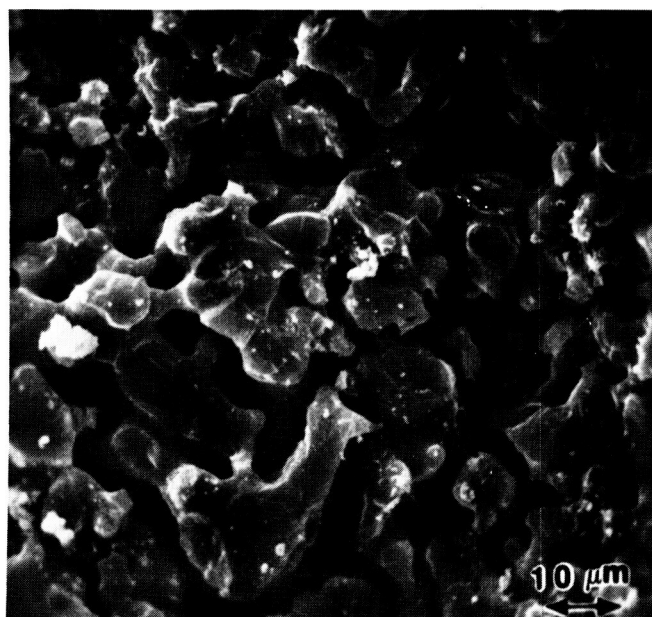


Figure 13. An example of an actual intermediate stage microstructure showing interconnected pore channels and solid phase. (Compare with the idealized structure in Figure 12.) (Si + 1 wt% Fe sintered in He 5 hrs. at 1375°C)

and B representing constants) are:

for lattice diffusion:

$$\Delta \rho = \frac{A D_l \gamma \Omega}{G^3 k T} t \quad (7)$$

for grain boundary diffusion:

$$\Delta \rho = \frac{B D_{gb} \gamma \Omega}{G^4 k T} t \quad (8)$$

Ideally, these equations would make it possible to differentiate between the two densification mechanisms by their grain size dependencies. However, they are only applicable over a density range small enough that no change in grain size occurs. (Sintering rate equations similar to Equation 4 do allow mechanisms to be differentiated by the grain size dependency.⁽³⁰⁾)

The combination of Kuczynski's rate exponents and the rate equations' grain size dependencies have been widely used to establish the predominant sintering mechanism at various intervals in the sintering process.

2.2.2.3 Final Stage

The final stage⁽²⁸⁾ begins when, as a consequence of densification, the pores have become isolated, mainly at four-grain corners. Some pores lie on grain boundaries and, depending on grain growth behavior, some may be within grains (Figure 14). The pores are usually modeled as spherical, but recent attempts have been made to model more realistic geometries.⁽³¹⁾

Coble⁽²⁸⁾ developed equations for the time dependency of density that are identical to Equations 7 and 8 above, except for the constants which derive from the spherical pore geometry. The grain boundary diffusion model assumes vacancy flux from the entire pore surface to the grain boundary. The analysis by Roso-

ORIGINAL PAGE IS
OF POOR QUALITY

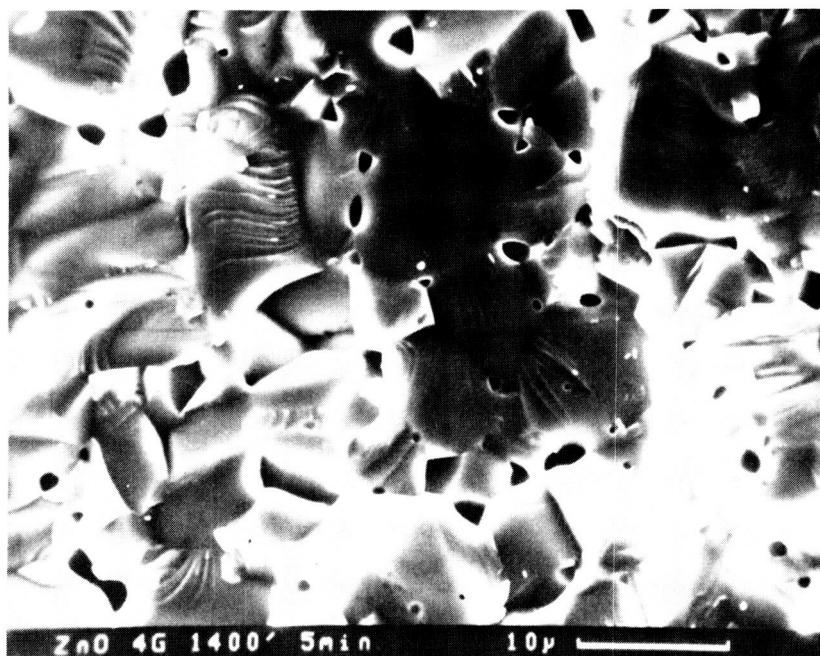


Figure 14. An example of a final sintering stage microstructure showing isolated pores at four-grain corners, on grain boundaries and within grains. Pores are often modeled as spherical; due to surface energy considerations, pores within grains are seen to be spherical, but pores on grain boundaries are not. (ZnO + 1 wt% MgO sintered in air for 5 min. at 1400°C)

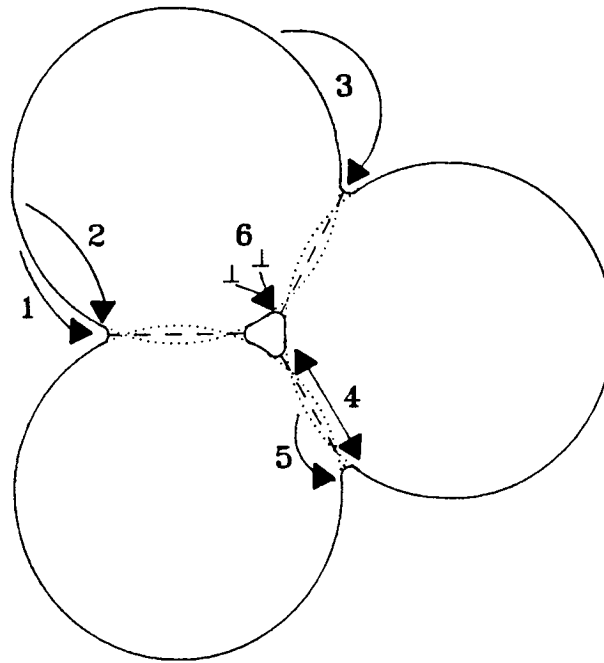
lowski and Greskovich⁽³²⁾ showed, however, that most vacancies move directly into the grain boundary from the edge of the pore.

Much of the experimental work on establishing sintering mechanisms has been done with these nearly dense samples because of the common desire to gain the understanding necessary to eliminate the small amount of porosity remaining late in this stage. Also, at this stage the experiments are a closer fit to the models than during the intermediate stage, and sample preparation and grain size measurement are relatively uncomplicated.

2.2.3 Sintering Diagrams

Ashby developed the concept of sintering diagrams^(33,17) as a way of linking the controlling sintering mechanism or mechanisms throughout the entire sintering process. The early efforts to understand sintering behavior had considered at most three or four possible material transport paths and attempted, as discussed previously, to determine "the sintering mechanism." Ashby⁽³³⁾ listed six distinguishable diffusion-controlled paths of material (or vacancy) transport considered to be the most likely mechanisms in the sintering of metal and ceramic powders; these are described in Figure 15.

He developed the equations necessary to determine the rate of neck growth that could be attributed to each mechanism at each stage of the sintering process for wires, two spheres or aggregates of spheres. He then constructed⁽³³⁾ diagrams that showed the region of neck size or density vs. temperature for which any one mechanism was dominant, and the boundaries between the regions. The equations were later refined,⁽¹⁷⁾ mainly to account for the facts that surface diffusion is necessary to redistribute the material removed from the grain boundary to the pore, requiring that the pores not become exactly cylindrical or spherical and that particle rearrangement must occur as densification takes place. He also



Mechanism			
Number	Transport Path	Source of Atoms	Sink of Atoms
1	Surface Diffusion	Surface	Neck
2	Lattice Diffusion	Surface	Neck
3	Vapor Transport	Surface	Neck
4	Boundary Diffusion	Grain Boundary	Neck
5	Lattice Diffusion	Grain Boundary	Neck
6	Lattice Diffusion	Dislocations	Neck

Figure 15. Alternate paths for atom transport during the initial stages of sintering. (After Ashby, Ref. 33)

expanded the diagrams to show regions where two or more mechanisms were significant.

Use of the diagrams to interpret sintering experiments was illustrated by reanalyzing some previously published data. Kuczynski⁽¹⁹⁾ had measured a value of $n \approx 5$ for the neck growth rate of both copper and silver spheres, leading him to conclude that volume diffusion was the dominant sintering mechanism. Ashby⁽¹⁷⁾ showed that the sintering conditions for the copper spheres fall within the surface diffusion field with large contributions from boundary diffusion at the lower temperatures and from lattice diffusion at the higher temperatures. The conditions for the silver spheres fall within both the surface and boundary diffusion fields with a major contribution from lattice diffusion from the surface. The data of Kingery and Berg⁽²⁰⁾ for the sintering of chains of sodium chloride spheres did fall entirely within the region of vapor transport as they had suggested. Ashby⁽¹⁷⁾ found that the data for the sintering of irregularly-shaped tungsten particles did not fit the calculated diagram at all. He suggested that the sintering behavior of such particles is controlled by the average size of the surface irregularity rather than the average particle size, an important factor to consider when studying the sintering behavior of typically irregular ceramic powder particles. Although still subject to many approximations, the sintering diagram approach to the determination of sintering mechanisms may be more realistic than reliance on the previous simpler single mechanism models.

2.3. GRAIN GROWTH

It was noted in Section 2.2.1 and Figure 1 that the primary driving force for sintering is the reduction in the free surface energy of the system. This is achieved by reducing the area of surfaces in the system by one, or a combination

of three processes: 1. conversion of many small particles into fewer large ones (coarsening) 2. replacement of the gas/solid interfaces by lower energy solid/solid interfaces (densification) 3. reduction in the amount of grain boundary area by grain growth (coarsening). Grain growth occurs at all stages of the sintering process. The initial stage two-sphere models discussed above do not, however, allow for grain growth. Most theories and models of grain growth consider coarsening only during final stage sintering since the primary goal in the sintering of ceramics has been to achieve high density while maintaining a fine, uniform grain size and most ceramics that sinter well do not undergo excessive grain growth until nearly full density is reached.

2.3.1. In Fully Dense Ceramics

The simplest model of grain growth considers the movement of a single grain boundary in a pure, dense material.⁽³⁴⁾ There is a free energy difference ΔG across a curved grain boundary having a surface energy γ and principal radii of curvature r_1 and r_2 :

$$\Delta G = \gamma V_m \left(\frac{1}{r_1} + \frac{1}{r_2} \right) \quad (9)$$

The molar volume of atoms moving across the boundary is V_m . This free energy difference provides the driving force for the boundary to move towards its center of curvature. The rate of boundary movement is proportional to the curvature, and thus inversely to the average grain size, \bar{G} , and proportional to the ability of the atoms to cross the grain boundary, D_{gb}^* . The rate of grain growth is then:⁽³⁴⁾

$$\frac{dG}{dt} \propto \frac{D_{gb}^*}{\bar{G}} \quad (10)$$

and

$$G^2 - G_0^2 \propto t \quad (11)$$

It is often found experimentally that the growth rate is less than this^(34,35) due to factors that inhibit grain boundary movement. Some of these factors will be considered next.

2.3.1.1. Impurity drag

Soluble impurities may segregate either to or away from a grain boundary if the resulting effect is to reduce the free energy of the system. Cahn⁽³⁶⁾ developed equations to describe the complex relationship between the velocity of a grain boundary and the diffusivity of the impurity, and the interaction of the impurity with the grain boundary. Qualitatively, he showed that at high boundary velocities faster diffusing impurities will exert the greatest drag while at low velocities slower diffusing impurities will cause the greatest drag. In the high velocity case, only the fast diffusing atoms can remain with the boundary and affect its mobility. In the low velocity case, the fast diffusing atoms will be able to redistribute themselves quickly enough to maintain the lowest energy distribution while the slower diffusing atoms obstruct boundary movement. Increasing the impurity concentration or decreasing the temperature will change the diffusion behavior and thus increase the impurity drag effect.

Brook^(37,38) has examined the low velocity case thought to be applicable to normal grain growth in single phase ceramics. In this case, the boundary velocity is:

$$v_b = F_b \left(\frac{M_b}{1 + M_b \alpha C_0} \right) \quad (12)$$

where F_b is the driving force, M_b , the boundary mobility, C_0 , the bulk impurity

concentration and α is the drag force on the grain boundary for unit volume and concentration when the boundary velocity or solute diffusion time is small.

For a constant ratio of boundary and bulk concentrations,

$$C_0 \propto G \quad (13)$$

and since the driving force is inversely proportional to the grain size, the grain growth rate is now:

$$\frac{dG}{dt} \propto \frac{1}{G^2} \quad (14)$$

or

$$G^3 - G_0^3 \propto t \quad (15)$$

2.3.1.2. In the Presence of Inclusions

As a grain boundary moves past a particle, the area of the boundary is reduced by an amount equal to the cross-sectional area of the particle (Figure 16). The surface area, and the surface energy, must increase if the boundary is to pull away from the particle. The particle thus exerts a restraining force on the grain boundary⁽³⁹⁾

$$F_{\max} = \pi r \gamma_{gb} \quad (16)$$

The grain growth rate is now

$$\frac{dG}{dt} = F_b - F_p \propto \frac{D_{gb}^*}{G} - \pi G \gamma \quad (17)$$

If there are a number of inclusions at the boundary, the boundary driving force may be insufficient to move it past the inclusions. Zener has calculated (according to Smith⁽⁴⁰⁾) the grain size limit in this case for a volume fraction, V_v , of

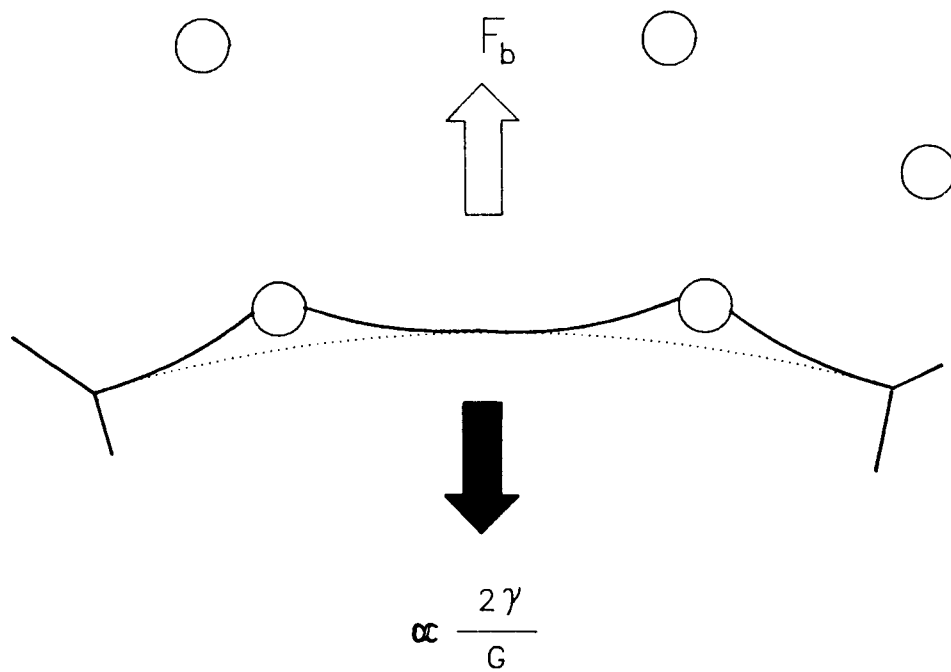


Figure 16. Inclusions will exert a restraining force on the boundary, restricting its motion. (After Porter and Easterling, Ref. 41)

randomly dispersed spherical particles of radius, a ,

$$G_{\text{lim}} \approx \frac{3a}{4V_v} \quad (18)$$

2.3.2. In Porous Ceramics

Pores can behave much like inclusions in retarding grain boundary movement. However, the situation is more complex since, unlike most inclusions, pores can move by diffusion processes. Pores move (Figure 17) by transfer of atoms from the front of the pore to the back. This transfer can take place by any of the diffusion mechanisms with a surface source listed in Figure 15. The effect of a pore on boundary movement will depend upon its mobility, M_p , relative to that of the boundary, M_b , and the geometry of the system.

2.3.2.1. "Spherical" Pores

For simplicity during final stage sintering, pores are often modeled as spherical, however, the pore must actually be nonspherical so that a driving force (regions of different curvature) for diffusion will exist (Figure 17). The pores can remain attached to the moving boundary if the velocities of the pore and the boundary are equal: ^(38,42)

$$v_p = v_b \quad (19)$$

where:

$$v_b = NF_p + \frac{M_p F_p}{M_b} \quad (20)$$

where N is the pore density at the boundary, F_p , the maximum force exerted on the boundary by the pore, M_p , the mobility of the pore, a function of the diffusivity

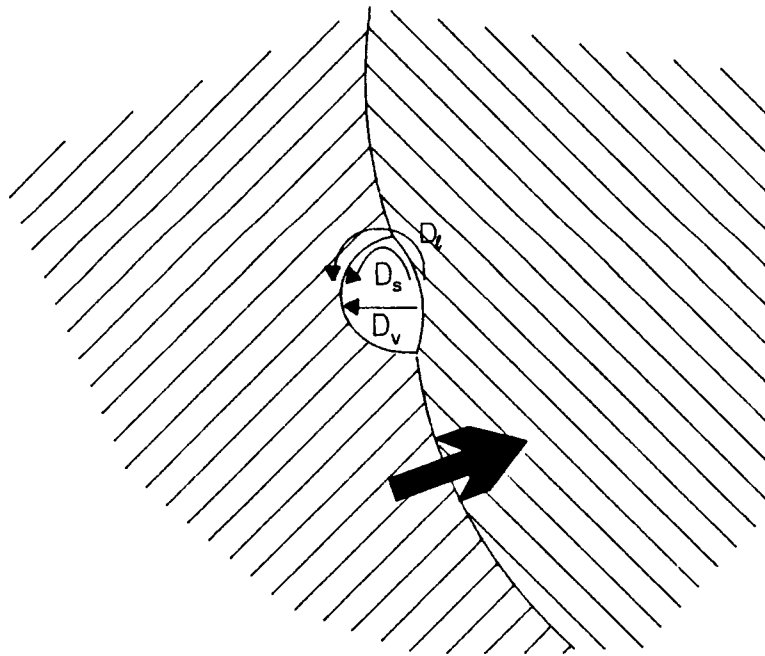


Figure 17. Grain boundary movement, here from left to right, is often controlled by pore mobility. The pore moves by atom diffusion from the front wall to the back.

of the atoms responsible for the pore movement, and M_b , the mobility of a pore-free boundary.

The boundary and pore separate if

$$v_p = F_p M_p < v_b = (F_b - NF_p) M_b \quad (21)$$

$$F_b > NF_p + \frac{M_p F_p}{M_b} \quad (22)$$

Small pores can move faster than large pores. Many large pores will exert a large restraining force on a boundary. During the early portion of final stage sintering both the grains and the pores are small. These small pores will not exert a very large drag on the boundary unless there are many of them. Whether the pores remain attached or not will depend on the relative velocities of the pores and boundary.

2.3.2.2. During Initial Sintering

Little attention has been given to the mechanisms or effects of grain growth during the early stages of sintering. The two-sphere models^(18,19,20) consider only neck growth and do not allow for grain growth. It has often been assumed that little grain growth occurs until quite late in the sintering process. Greskovich and Lay⁽⁴³⁾ observed extensive grain growth in Al_2O_3 compacts even with densities < 40% of theoretical. Concurrently with the grain growth, the microstructure changed from the assembly of isolated particles comprising the green compact to a wormy or chain-like structure of continuous and interwoven solid and pore phases characteristic of the intermediate stage. Greskovich and Lay⁽⁴³⁾ suggested, as shown in Figure 18, that first neck growth occurs between particles of different size. (The important difference from models for densification is that

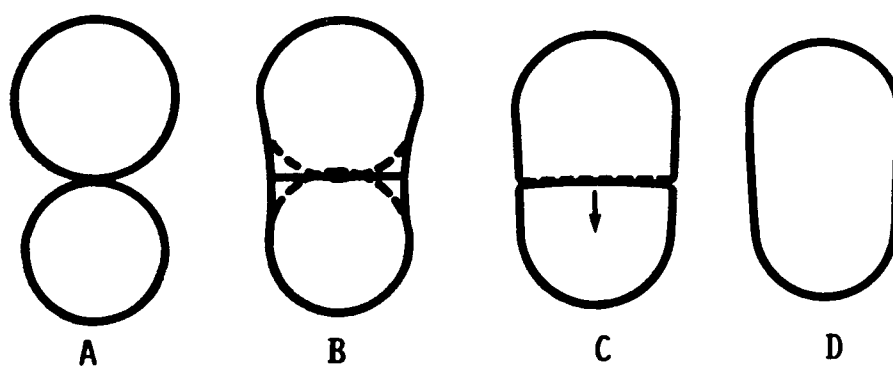


Figure 18. Qualitative mechanism of grain growth in porous compacts. (A) Particles of slightly different size in contact, (B) neck growth between contacting particles, (C) grain boundary migrating away from contact plane, and (D) grain growth. (After Greskovich and Lay, Ref.43)

coarsening requires the presence of particles of different size in contact with one another.) Neck growth continues until the neck is no longer the region of minimum cross-sectional area. The grain boundary is then free to move and will migrate rapidly (Figure 18C) through the smaller particle leaving a single large particle (Figure 18D). Figure 19 illustrates how this mechanism could result in the chain-like structure often observed. They suggested that this mechanism would be the primary means of grain growth until densification led to the space-filling microstructure typical of the final sintering stage.

If the development of the chain-like structure occurs without concurrent densification, the enlargement of **both** the particles and pores, as seen in Figure 20, has the effect of producing interconnected structures in which the scale of the microstructure (channel size, solid phase cross section) progressively increases.

2.3.3. Abnormal Grain Growth

During the later stages of sintering some grains may grow to be much larger than the average grain size if conditions are favorable. A large grain surrounded by small grains will have many grain boundaries, each with a small convex (from the view of the large grain) radius of curvature (Figure 21). Each of these boundaries will have a high driving force, causing it to move away from the large grain, thus further increasing the size of the grain and promoting further growth.⁽⁴¹⁾ Milled powders often have a few very large grains that may grow abnormally. Such growth can also occur in regions of fewer than average second phase particles or lower solute concentration and is very likely to occur when pores have become small enough that they no longer restrain boundary movement.⁽⁴²⁾ Lay⁽⁴⁴⁾ has noted that density variations in a sample may lead to a wide grain size distribution, allowing abnormal grain growth.

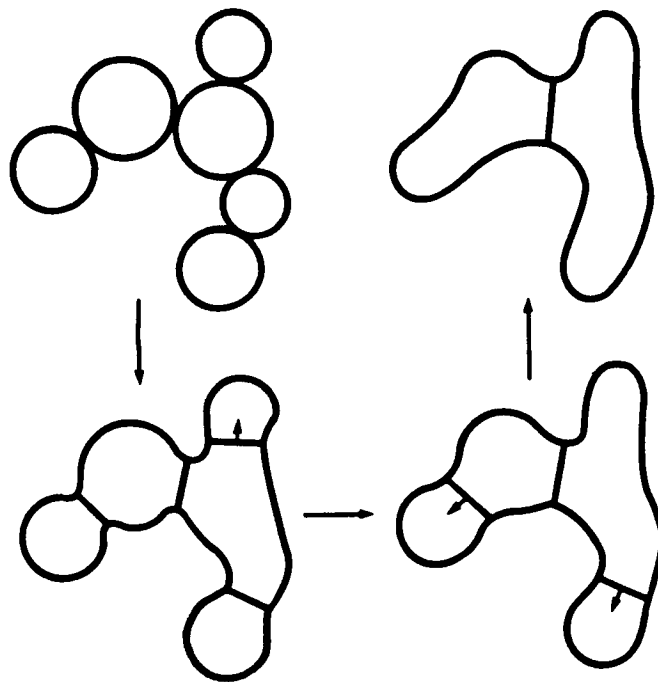
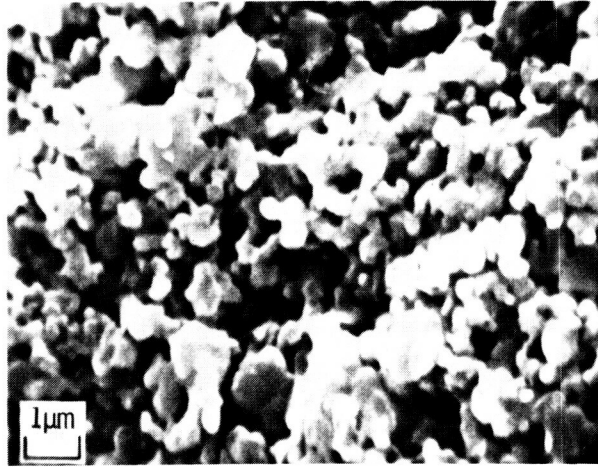
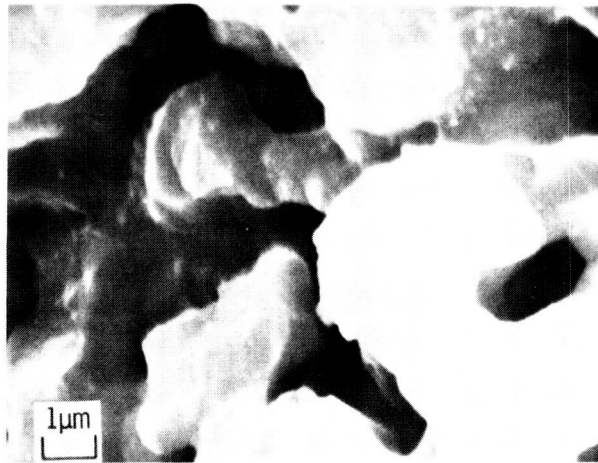


Figure 19. Diagram illustrating grain growth in cluster of particles by surface diffusion. Arrows on grain boundaries indicate direction of boundary movement. (After Greskovich and Lay, Ref.43)



A

ORIGINAL PAGE IS
OF POOR QUALITY



B

Figure 20. Enlargement of both particles and pores due to coarsening without concurrent densification. (Si sintered in (A) H_2 and (B) He 5 hours at $1375^\circ C$)

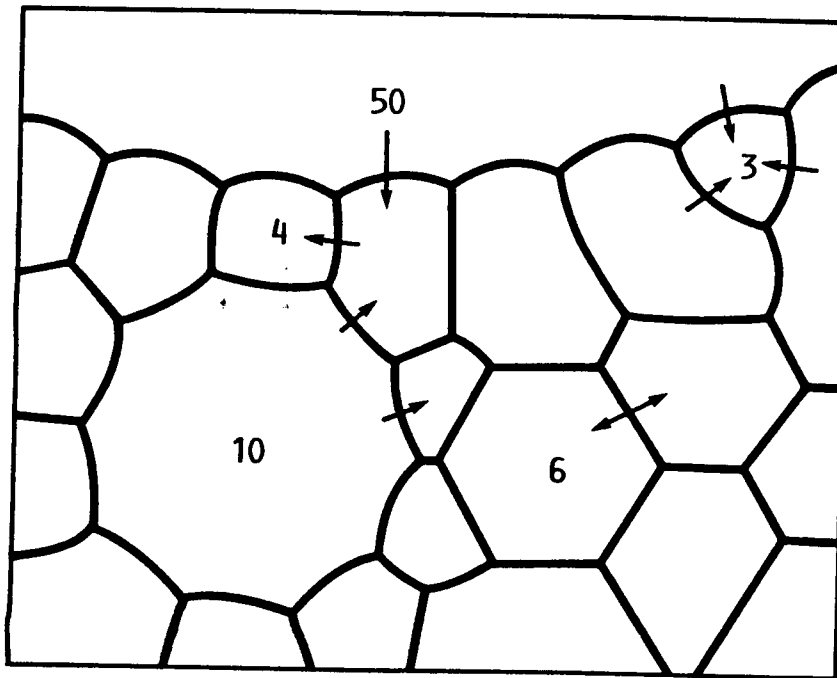


Figure 21. Section of a polycrystalline structure showing grains having various numbers of sides. The 50-sided grain has the most strongly curved boundaries and thus the strongest tendency to grow even larger. Arrows show the direction of grain boundary movement. (After Burke and Rosolowski, Ref. 1)

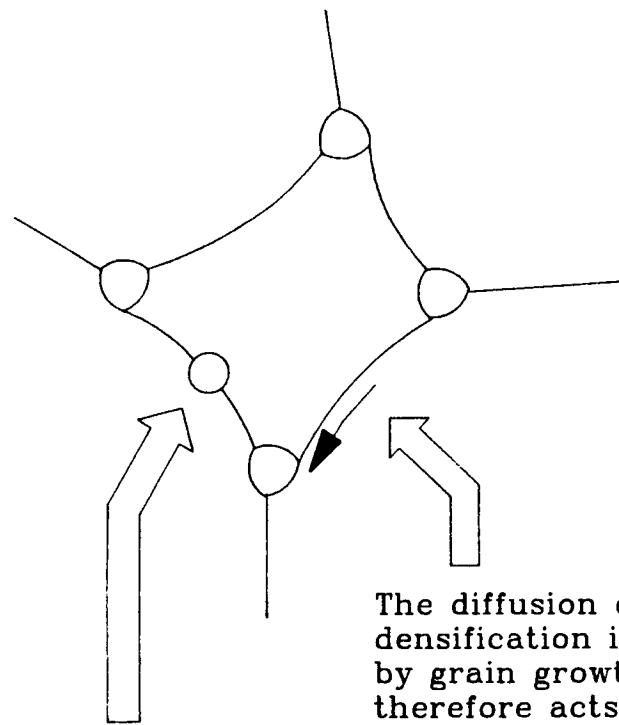
2.4. SIMULTANEOUS DENSIFICATION AND COARSENING

During the sintering of a powder compact, both densification and coarsening occur simultaneously. The extent of each of these processes can influence the rate at which the other is able to proceed (Figure 22). This has been one of the main difficulties in interpreting sintering studies. The extent of interference can vary from system to system. In some materials, such as silicon and other covalent ceramics, grain and, consequently, pore growth may be so great early in the process that little densification occurs at all.^(45,46) Many other ceramics easily approach nearly theoretical density despite concurrent grain growth – the most studied of these being MgO-doped Al_2O_3 .⁽³⁰⁾

It has been recognized that to understand and control the sintering process, both densification and coarsening must be considered and the relationship between them assessed.^(47,48,49) Ideally, to achieve high density, the aim should be to increase the rate of densification relative to that of coarsening. It is consequently important to be able to study densification and coarsening as separate processes (or at least as separable processes) so that the choice of the fabrication variables can be made on the basis of identified mechanisms for each of the separable processes.

To an approximation, pure densification can be studied in porous compacts by the technique of hot pressing, the driving force arising from the applied pressure acting on the densification process but not on coarsening.^(16,50) Using this method simple relations between the densification rate and the processing variables (pressure, grain size, additive content) can be found experimentally⁽⁵⁰⁾ and related to available models.

Similarly, certain aspects of coarsening processes can be isolated by studying materials such as silicon⁽⁴⁵⁾ (where densification is small enough to be neglected as an interfering factor) or fully dense systems⁽³⁵⁾ (where densification has been



The diffusion distance for densification is increased by grain growth which therefore acts to slow the densification process.

The ease of pore movement (inversely related to pore size) is increased by densification which therefore acts to accelerate the grain growth process.

Figure 22

completed and in this way is eliminated as a complicating factor). These examples suggest, however, the limited range of conditions (compositions and microstructures) over which coarsening studies can be made and it remains true that no single technique has emerged capable of examining these processes in the way that has been possible using hot pressing kinetics for the densification process. Since densification and coarsening mechanisms cannot be separately identified and measured during sintering, a method of looking at the ratio between them is needed.

2.4.1 Densification Rate:Coarsening Rate Ratio

Two general approaches to representing the effect of processing variables on the densification rate:coarsening rate ratio have been proposed. The first by Cannon and Yan^(47,48) plots grain size vs. density and compares the resultant curve to those calculated for various combinations of sintering mechanisms. This approach has been used by Eisele⁽⁵¹⁾ in the analysis of kinetic data from hot pressing studies. The second, used in several studies^(52,53,54) plots specific surface area vs. density. Burke, Lay and Prochazka,⁽⁵⁵⁾ and Jernot,⁽⁵⁶⁾ have extended this method to compare the resultant curve to theoretical lines for pure densification and pure coarsening.

2.4.1.1 Cannon and Yan Model

Cannon and Yan^(47,48) developed a model for normal coarsening and densification occurring simultaneously during sintering. They define normal coarsening to be a condition of unchanging topology, that is the number of pores per grain and the ratio of the average pore size, \bar{p} , to the average grain size, \bar{G} , remain constant. It is strictly applicable to final stage sintering, but is considered to be semiquantitative during intermediate stage sintering.⁽⁴⁷⁾ It is assumed that

densification is the result of material transport from grain boundaries to pores by lattice or boundary diffusion and that grain growth is controlled by the pore mobility which is limited by surface, vapor, or lattice diffusion. The extent of grain growth and the final density depend on the rate controlling mechanisms and the densification kinetics. An additional assumption⁽⁴⁷⁾ of this model is that the average grain and pore geometry is a tetrakaidecahedron with a spherical pore at every four-grain junction. The calculations are further based on simple sintering models which require equiaxed particles uniformly packed to a high green density.

The quantity which describes the path of microstructural evolution during sintering when both coarsening and densification may be occurring is $\frac{d\bar{G}}{d\bar{p}}$, the change in grain size with change in pore size.⁽⁴⁷⁾ First it should be noted that the net rate of pore size change is:

$$\frac{d\bar{p}}{dt} = \left[\frac{\partial \bar{p}}{\partial t} \right]_d + \left[\frac{\partial \bar{p}}{\partial t} \right]_c \quad (23)$$

where the subscripts d and c refer to the rates of pore size change during densification (a negative value) and during coarsening (positive), respectively.

Then

$$\frac{d\bar{G}}{d\bar{p}} = \frac{\frac{d\bar{G}}{dt}}{\left[\frac{\partial \bar{p}}{\partial t} \right]_d + \frac{\bar{p}}{\bar{G}} \frac{d\bar{G}}{dt}} \quad (24)$$

Cannon⁽⁴⁶⁾ then defined the parameter Γ , the relative coarsening: densification ratio:

$$\Gamma \equiv - \frac{\bar{p}}{\bar{G}} \frac{\left(\frac{d\bar{G}}{dt} \right)}{\left(\frac{\partial \bar{p}}{\partial t} \right)_d} = - \frac{\frac{d \ln \bar{G}}{dt}}{\frac{\partial \ln \bar{p}}{\partial t}} \quad (25)$$

With this general relationship, Γ can be calculated from sintering models using the starting grain size and density and assumed sintering mechanisms. It is necessary to consider simple cases where only one densification mechanism and one coarsening mechanism are predominant. Figure 23 shows the results to be expected in the case of coarsening controlled by surface diffusion and densification controlled by grain boundary diffusion. If Γ , the coarsening:densification ratio, is large, grain growth will predominate and the density will reach only a limiting value. If Γ is very small, the density can reach 100% with little grain growth. Similar models have been developed for other combinations of material transport mechanisms.^(47,48)

This is the only model available to predict directly the coarsening:densification ratio during final stage sintering; however, there are serious difficulties in using this model to predict the sintering behavior of a real powder compact. The first is the lack of diffusion data needed to make the theoretical calculations: surface and vapor transport data are particularly lacking. Even for a material for which data are available, e.g. Al_2O_3 , there is a wide disparity in the published values.⁽⁵⁷⁾ For other materials, data may not be available at all or are of doubtful reliability. The other problem is, as with the sintering models on which the approach is based, the assumed predominance of only one densification and one coarsening mechanism.

In practice, the lines for several combinations of possible mechanisms may be calculated for starting conditions the same as those of the material being studied. The experimental data can then be compared with the calculated lines to determine

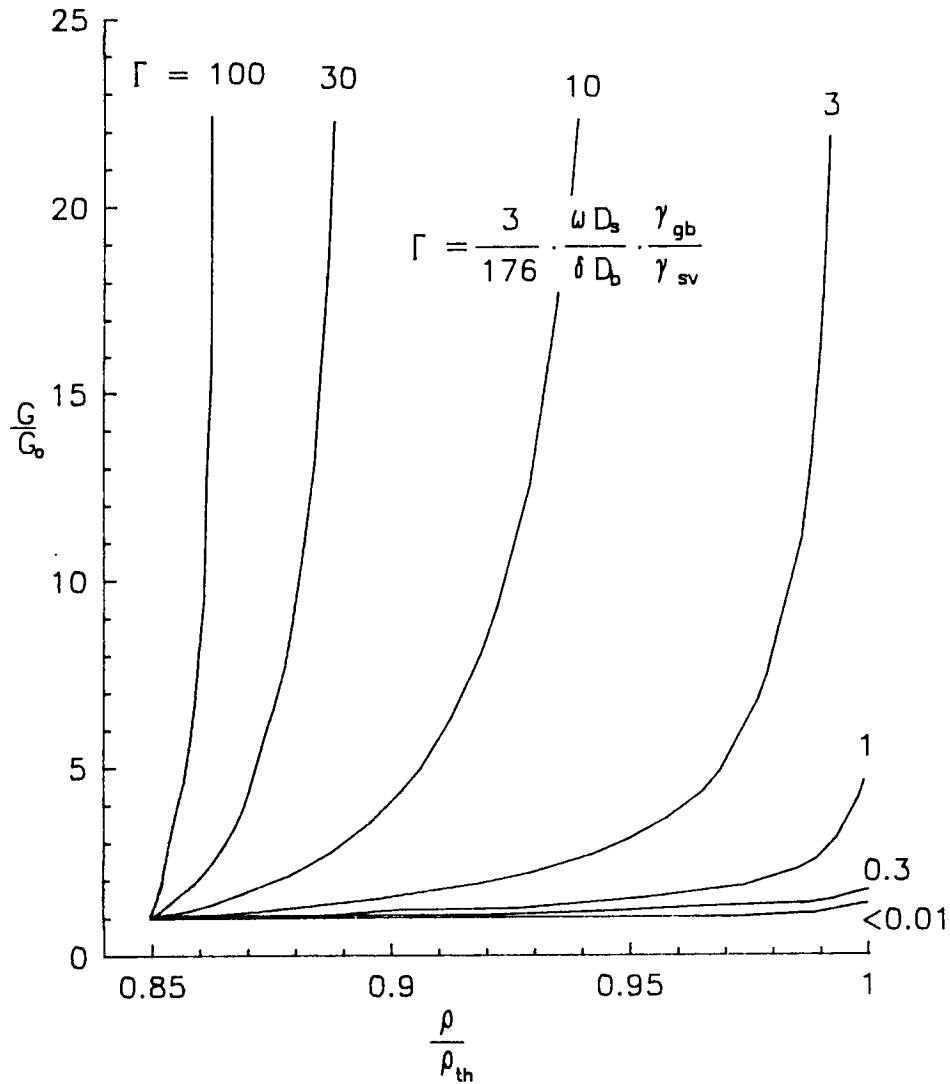


Figure 23. Relation between grain size and density for grain growth controlled by surface diffusion and densification controlled by boundary diffusion. Γ is the coarsening/densification ratio. (After Cannon, Ref. 47)

the actual mechanism ratio. Data from different experiments can be plotted together to show the direction of change in the densification:coarsening ratio caused by changes in processing conditions (Figure 24A).

Eisele⁽⁵¹⁾ used this approach to compare the sintering behavior of undoped and MgO-doped Al_2O_3 . He obtained values for Γ from density vs. time data during hot pressing but found relatively slight change in the coarsening:densification ratio with the addition of magnesia. He derived an expression for the ratio that requires knowledge of only the density and its first and second derivatives with time during sintering, which can be obtained directly by experiment, thus avoiding the problems of lack of diffusion data, unknown mechanisms, etc.

2.4.1.2 Burke, Lay and Prochazka Model

Since the driving force for both the densification and coarsening processes is related to the reduction in interfacial area, it is somewhat surprising that little attention has been given to the direct observation of changes in surface area in developing sintering models and equations.

Burke *et al.*⁽⁵⁵⁾ suggested that such an approach could be used to show the relationship between densification and coarsening during intermediate and final stage sintering by means of the diagram shown in Figure 25 in which pore surface area is plotted against fractional density. Materials with differing coarsening and densification behaviors should be distinguishable by the appearance of their surface area reduction trajectories. In the case of pure coarsening, the surface area will be reduced with no increase in density along a line from the initial to final surface areas parallel to the surface area axis (trajectory C). When all of the surface area reduction is occurring by mechanisms that result in densification, they suggested (based on work by DeHoff *et al.*⁽⁵²⁾) that the trajectory (D) will be a straight line connecting the initial values and the final state of full density with zero surface area. In a powder compact in which both densification

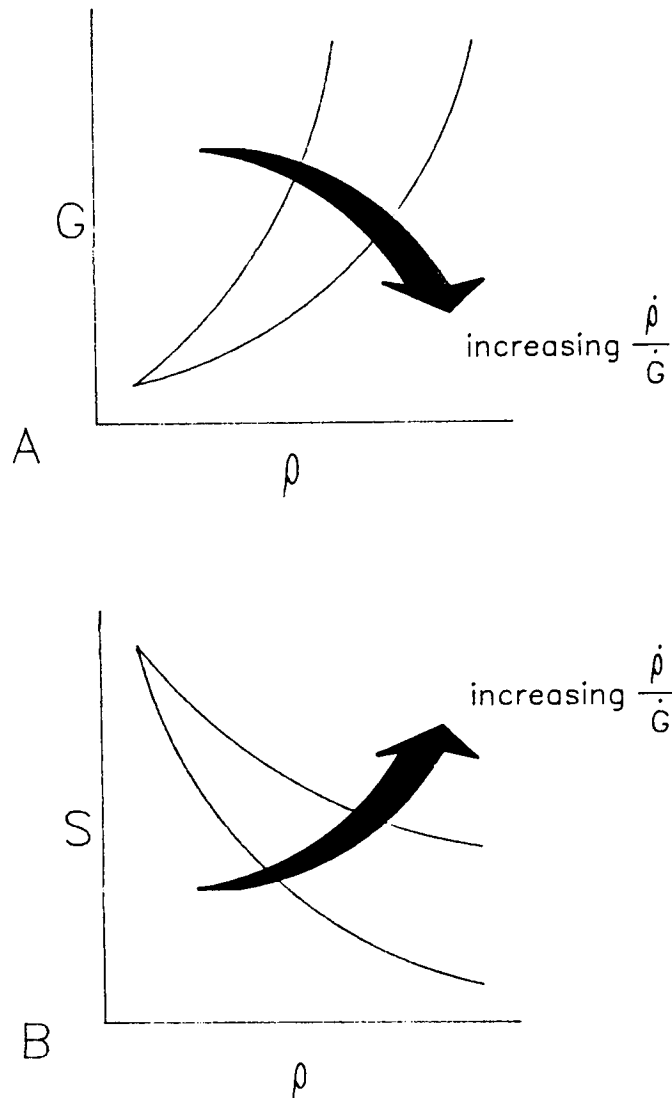


Figure 24. Despite difficulties in using the graphical methods to predict exact trajectories (uncertainty in diffusion coefficients, etc.), they allow, in principle, clear interpretation of experimental results in which changes in the processing conditions have caused changes in the value of the ratio.

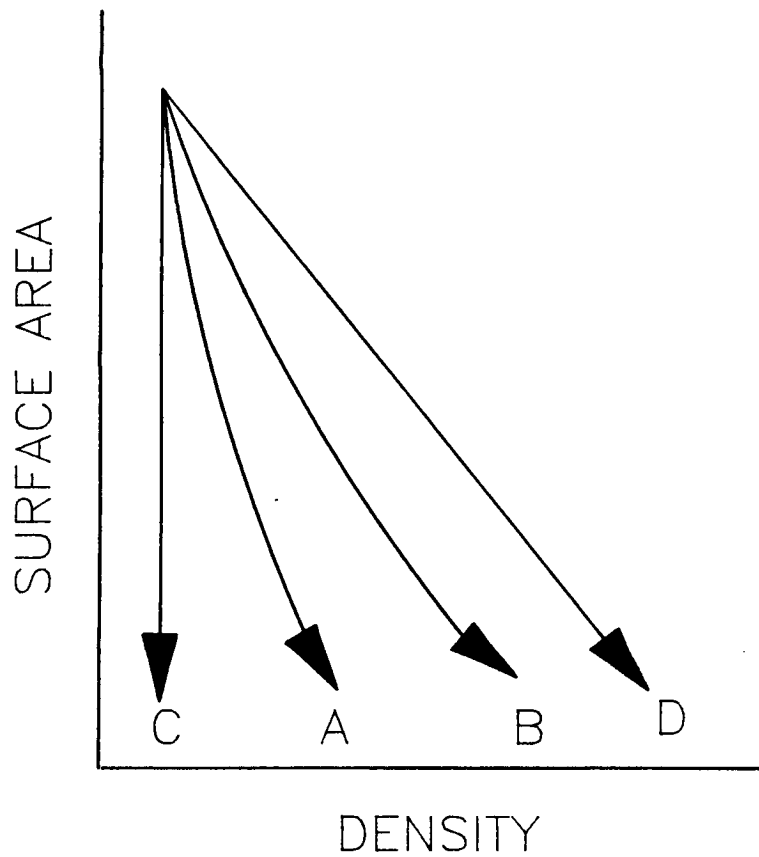


Figure 25. Surface area vs. density relationship during sintering. C is the trajectory of pure coarsening, D the trajectory of pure densification, and A and B represent mixed behaviour with B being more favourable from the point of view of densification.

and coarsening are occurring simultaneously, the plot will be a curve falling between the two extreme conditions (e.g., trajectories A and B).

Burke *et al.*⁽⁵⁵⁾ used this model to investigate the effect of MgO additions (at a level high enough to give second phase particles) on the densification:coarsening rate ratio during the sintering of Al_2O_3 . Since the trajectories of both the doped and undoped materials were the same, they concluded that MgO did not affect the ratio of the controlling mechanisms.

Calculation of theoretical trajectories for possible densification and coarsening mechanisms is subject to the same constraints as the Cannon and Yan model, i.e., limited diffusion and surface energy data and the probability of concurrent mechanisms. However, since measurement of surface area and density is fairly simple, this model is useful for assessing the influence of processing variables in terms of displacements of actual trajectories towards one or the other of the ideal types as shown in Figure 24B.

Since this model offers the possibility of experimentally determining the effect of processing variables on the densification:coarsening ratio, it will be used as the basis for this study.

2.4.2 Surface Area Reduction

There have been several approaches to the consideration of the relationship between the reduction in surface area and densification. Two of these, both with a topological basis, predict a linear relationship. The other approaches to be discussed are based on models of spherical particles and their contact points with adjacent particles.

Rhines *et al.*,⁽⁵⁸⁾ while investigating the sintering of metal powders, examined the topological changes occurring, since this would make it possible to describe the process quantitatively without particle shape, size or distribution restrictions.

They were particularly interested in the changes occurring during the intermediate stage when most of the topological change in a powder compact would be due to densification. They also assumed that surface area, another parameter that can be measured without reference to particle shape, size or distribution, must be related to the density since the driving force for sintering is the reduction of the excess surface energy which is directly related to the surface area. Assuming that "each gram of material transported to increase the density requires the expenditure of a constant amount of energy," they derived a rather complex linear relationship between the density and the surface area. This derivation assumes that the same diffusion mechanism is occurring throughout the process and that constant particle curvature differences are maintained; it has been accordingly criticized.⁽⁵⁹⁾ The relationship later was simplified to⁽⁵²⁾

$$\rho = mS_V^p + \rho_{th} \quad (26)$$

(where ρ and ρ_{th} are the actual and theoretical density, respectively, S_V^p is the surface area per unit volume and m is a constant) and found to apply to the behavior of a variety of copper and nickel powders during intermediate stage sintering ($\rho \sim 65 - 90\%$).^(58,52) In each case, the linear trajectory, when extrapolated to lower densities, reaches a much higher surface area than the actual surface area of those samples, including the green powder compact. The path of surface area change of an antimony powder compact showed considerable curvature due to early coarsening. In developing their model (Section 2.4.1.2 above), Burke *et al.*⁽⁵⁵⁾ followed this essentially empirical linear relationship between surface area and density, measuring the surface area per unit mass, S_m , instead of S_V^p .

Prochazka⁽⁶⁰⁾ has suggested that the linear relationship between surface area and density can also be derived from the topological models of domain and grain structures considered by Cahn.⁽⁶¹⁾ Cahn's model structure is composed of space-

filling, connected grains of two kinds, α and β . These grains are, for simplicity, considered to be polyhedra composed of a number of polygons, P , with an average number of sides or corners, n . Cahn describes two types of structures: 1. the phase or domain structure maintaining only surfaces between unlike domains or phases (Figure 26A), and 2. the "grain" structure keeping all grain or impingement surfaces (Figure 26B). The surfaces between unlike phases ($\alpha - \beta$) considered in the domain structure are analogous to the pore/solid interface measured for the surface area vs. density plots.

All grains have an equal probability, f , of being α , thus requiring that both α and β polyhedra have the same size and shape distributions. The volume fraction of α grains is thus also equal to f . Since all grains have an equal probability, f , of being α , the probability of two adjacent grains both being α is f^2 ; this is thus also the probability of the formation of an $\alpha - \alpha$ interface and the fraction of those polygons of the total number of interfacial polygons. Likewise, the probability of a grain being β is $(1 - f)$ and the fraction of $\beta - \beta$ interfaces is $(1 - f)^2$. The fraction of $\alpha - \beta$ polygons is then $1 - f^2 - (1 - f)^2 = 2f(1 - f)$. In the domain structure (Figure 26A), the fraction of polygons that are $\alpha - \beta$ polygons, P' , is

$$P' = 2f(1 - f)P \quad (27)$$

where P is the total number of polygons in a similar grain structure. In a sintered structure, where α is solid and β is porosity, the pore/solid surface area is a linear function of the volume fraction of α , i.e., the density: the trajectory of pure densification (D in Figure 25) is linear. The relationship expressed by Equation 27 is true for $0 \leq f \leq 1$.

In a series of papers,^(22,62,63,64,65) German and Munir have developed relationships between the change in surface area, the extent of neck growth and the sintering time. All are based on the two-sphere model shown in Figure 10 with

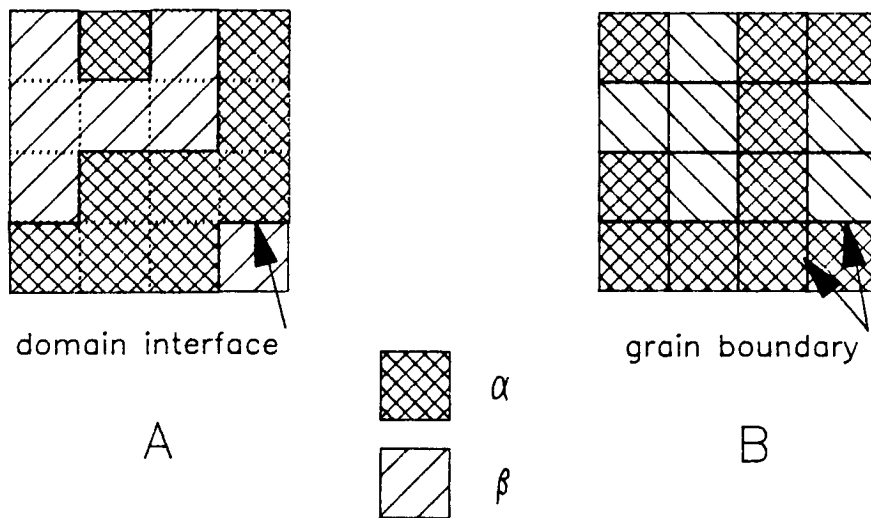


Figure 26. Space-filling polyhedra can form two kinds of structures: (A) the phase or domain structure maintaining only interfaces between unlike phases and (B) the grain structure keeping all interfaces. The pore/solid interface of a sintered structure can be represented by the domain structure.

the neck assumed to have a circular cross-section and the neck curvature defined by a modified catenary curve, which results from the requirement of a minimal surface area (energy). These models are applicable only up to the point when the growing necks begin to interfere with each other: $\frac{\Delta S}{S_0} \approx 0.5$. They developed relationships between surface area, coordination number, and the neck size: particle size ratio for both surface and bulk transport controlled sintering. Their objective was to show that the morphology changes occurring during sintering could be measured by the relatively simple technique of surface area measurement instead of the much more tedious neck size measurement. Based on this geometric analysis, they considered various relationships that might give useful methods of analyzing experimental data and compared calculated curves to actual published data. Based on their equation for bulk transport controlled densification, they derived a relationship between S_V^P and ρ :⁽⁶³⁾

$$\frac{S_V^P}{S_0} = \frac{S_m}{S_0} \rho = \frac{S_m}{S_0} \frac{\rho_0}{\left(1 - \frac{\Delta L}{a}\right)^3} \quad (28)$$

where $\frac{\Delta L}{a}$ is the fractional linear shrinkage and thus $\frac{\rho_0}{\left(1 - \frac{\Delta L}{a}\right)^3}$ is, approxi-

mately, the density. They plotted this equation for possible values of N_c and compared these curves with the experimental data of DeHoff *et al*⁽⁵²⁾ (see above). The calculated lines are highly curved for low values of N_c at low density, but at $N_c \geq 6$ and densities in the range of intermediate stage sintering, the lines become nearly linear; German and Munir⁽⁶³⁾ agreed that DeHoff's proposed linear relationship⁽⁵²⁾ (Equation 26) is a reasonable approximation for intermediate stage sintering.

The analysis by Jernot⁽⁵⁶⁾ has provided further understanding of the nature of the surface area vs. density curves while using a simpler geometry than that of German and Munir. The geometric model is again that of necks growing between

equal-sized spheres in contact. Since the neck area is very small, the surface area of each particle is considered to be reduced simply by the area of each circular contact multiplied by the coordination number. The total surface area reduction per unit volume is then determined by calculating the number of particles per unit volume from the particle size and the volume fraction of solid (relative density), resulting in:⁽⁵⁶⁾

$$S_v^p = \frac{3(N_c - 1)}{a} \left[\left(V_v^s \right)^{\frac{2}{3}} - V_v^s \right] \quad (29)$$

This relationship will give the curves shown in Figure 27A. It can be seen that for low density green compacts (e.g., $N_c = 4$), the trajectory has a slight curvature, but that for higher starting densities, the trajectory is linear. A similar relationship can be developed for the specific surface area per unit mass.

$$S_m = \frac{3(N_c - 1)}{a \rho_{th}} \left[\frac{1}{\left(V_v^s \right)^{\frac{1}{3}}} - 1 \right] \quad (30)$$

The trajectories for this case are shown in Figure 27B. It should be noted that the curvatures of the low coordination number lines of the S_v^p vs. V_v^s (Figure 27A) and S_m vs. V_v^s (Figure 27B) are opposite. Since matter is being pulled into the volume under consideration as shrinkage proceeds, S_v^p does not decrease as rapidly as S_m .

All of these models confirm that the linear trajectory for pure densification chosen by Burke *et al.*⁽⁵⁵⁾ for their surface area vs. density diagram (Figure 25) is justifiable.

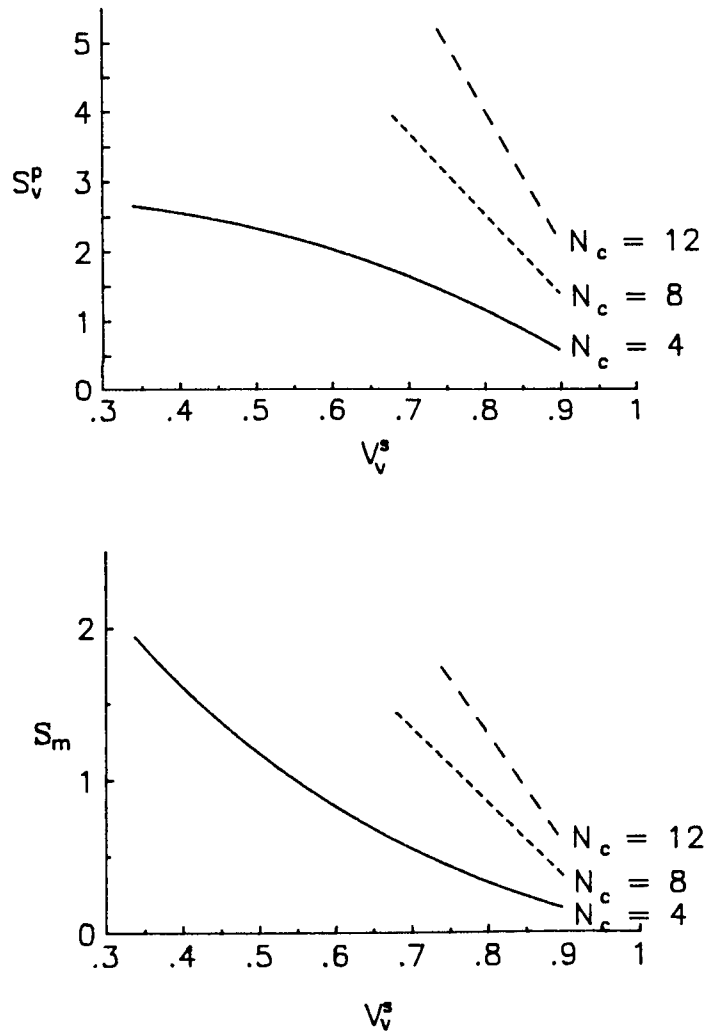


Figure 27. Trajectories of surface area reduction with pure densification predicted by the model of Jernot.⁽⁵⁶⁾ Trajectories of compacts with low coordination number show slight curvature while those with higher N_c are linear. The curvature of the S_v line is reversed from that of the S_m line because additional material is being drawn into the volume unit.

2.5 STEREOLOGY

Stereology has been defined as "a body of mathematical methods relating three-dimensional parameters defining the structure to two-dimensional measurements obtainable on sections of the structure."⁽⁶⁶⁾ The techniques are widely used by biologists and the relationships have been developed by mathematicians, but its use in materials has been more limited. Better known as quantitative metallography, the most common materials application is grain size measurement.

A few researchers have applied stereological techniques to the study of the sintering of metal powders in an effort to quantitatively describe the microstructural evolution. Aigeltinger and DeHoff^(53,67) were particularly interested in the topological properties during the sintering of uncompacted copper powders. Various measurements were made as a function of porosity. Aigeltinger and Exner⁽⁶⁸⁾ characterized the interaction between interfaces, e.g., pore/solid and grain boundary, during the sintering of copper powders. This approach to understanding sintering behavior has not been applied to ceramics.

More details of the use of stereology in this work will be given in Chapter 3.

2.6 SYSTEMS TO BE INVESTIGATED

Since the objective of this work is to evaluate experimental techniques that could be applicable to the study of coarsening during the sintering of any ceramic, the choice of materials to be studied can be made with a view to finding systems in which the extent of coarsening can be varied. The following systems have been elected to be studied: 1. Al_2O_3 - MgO , 2. Y_2O_3 - MgO , 3. SiC - C - B .

2.6.1 Al_2O_3 - MgO

Coble⁽⁶⁹⁾ showed that Al_2O_3 could be sintered to full density by the addition of 0.25 wt.% MgO. In this case MgO acted in solid solution to increase the rate of densification and to prevent discontinuous grain growth, although the mechanism of this action was uncertain. Coble discounted the possibility that MgO reduced the grain boundary mobility, either by solid solution or particulate inhibition, since the rate of normal grain growth was not reduced. The same argument applied to an increase in the grain boundary to surface energies ratio affecting the inhibiting behavior of the pore phase. Extensive investigation into the effect of MgO on the sintering behavior of Al_2O_3 by Peelen^(70,71) reached similar conclusions: first, below the solid solubility limit, the important function of MgO is enhancement of the pore removal rate (which can promote normal grain growth) and not a reduction in grain boundary mobility, and second, no evidence of MgO segregation at grain boundaries was found by Auger spectroscopy. Attempts to determine the mechanism by which MgO allows Al_2O_3 to reach full density without the occurrence of abnormal grain growth continue.

Burke *et al.*⁽⁵⁵⁾ have supported the argument that MgO segregates at the grain boundary, reducing grain boundary mobility with experiments in which grains grew very large laterally in a MgO-depleted near-surface layer of polycrystalline samples, but did not grow into the MgO-rich region below. Estimates of the grain boundary velocities implied that the grain boundary mobility in the MgO-deficient region was ~100 times that in the MgO-doped region. Evidence of such segregation by Auger spectroscopy has been negative.^(70,72,73)

Heuer,^(74,75,76) noting that the important effect of MgO is to prevent exaggerated grain growth, has suggested that MgO instead may act by increasing the pore mobility by increasing D_g , allowing pores to remain attached to migrating boundaries until full densification is achieved. However, Burke *et al.*⁽⁵⁵⁾ concluded,

based on surface area vs. density plots of an alumina containing second-phase spinel particles, that MgO does not change pore mobility. Peelen^(70,71) observed, that the case in which second phase particles are present is different from that in which MgO is present in amounts below the solid solution limit in that the second phase particles do exert a drag force on the grain boundaries. Bennison and Harmer⁽³⁵⁾ measured grain growth kinetics in fully dense undoped and MgO-doped Al_2O_3 samples annealed at 1600°C for various times and determined that MgO decreased M_b by a factor of 5 (or even 50 in an ultrapure starting powder⁽⁷⁷⁾) and increased M_p by a factor of 16. Much of the difficulty in reaching a definitive conclusion results from inadequate experimental methods, especially the sensitivity of instruments that could detect boundary and surface segregation.⁽⁷³⁾

Brook⁽⁴⁹⁾ has suggested again the importance of considering the densification/coarsening ratio. Densification of Al_2O_3 is believed to be controlled by cation lattice diffusion⁽⁷⁸⁾ while grain growth during final stage sintering is believed to be governed by surface diffusion controlled pore drag. MgO has been shown by the study of hot pressing kinetics to increase D_l of Al_2O_3 by a factor of three when added at the solid solubility limit.⁽⁷⁹⁾ Work using the scratch annealing technique⁽⁸⁰⁾ has shown that MgO reduces D_s of Al_2O_3 by a factor of 10 at 1650°C . These two factors result in an increase in the densification/coarsening ratio of 30 times. A ratio increase of this magnitude is then a suitable test case since it would be expected to be apparent on a surface area vs. density plot and to allow evaluation of the sensitivity of such plots.

2.6.2 Y_2O_3 - MgO

Yttria has generated interest for the application of its optical properties, especially in severe environments, e.g., visible light and IR windows,⁽⁸¹⁾ laser hosts,⁽⁸²⁾ and high pressure sodium lamp envelopes.⁽⁸³⁾

Transparent Y_2O_3 of greater than 99% theoretical density has been produced by hot forging,⁽⁸⁴⁾ vacuum hot forging with LiF as an additive⁽⁸¹⁾ and vacuum hot pressing.⁽⁸⁵⁾ Sintering to high density without applied pressure has been more difficult. Early (1966) work by Furlong and Domingues⁽⁸⁶⁾ achieved densities of 60 - 98% with six salt-derived powders at 1600°C for times ranging from 1 to 20 hours. The particle size distribution of the powder and pore size distribution of the green compact were found to be critical factors in achieving high sintered density. All of these powders tended to form agglomerates of some type.

Work was then primarily aimed at finding a sintering aid that would promote greater densification without degrading the optical or mechanical properties of laser hosts. Jorgensen and Anderson⁽⁸⁷⁾ reported that addition of ~10 mole % ThO_2 yielded full densification by segregating at the grain boundaries, reducing grain boundary mobility and thus inhibiting discontinuous grain growth which trapped pores within the grains.

The latest efforts have been directed towards finding additives that will produce a high density during sintering and will maintain optical transparency during exposure to the high pressure sodium lamp environment. Toda *et al.*⁽⁸⁸⁾ used BeO as a liquid phase additive. Lanthanum oxide acts by an unusual transient solid phase mechanism^(89,90) in which, when the material is sintered in a two-phase region, the second phase retards grain growth enough to allow pores to remain on the grain boundaries. The piece is then annealed in the lower temperature single-phase region to produce a dense, pore-free body.

Alumina⁽⁸³⁾, MgO ⁽⁹¹⁾ and MgAl_2O_4 ⁽⁹¹⁾ were each found to develop a liquid phase when added in amounts of < 5 wt%. In the Y_2O_3 - MgO system at temperatures near the eutectic temperature (2110°C), liquid phase sintering was reported to occur by an unknown mechanism considered to be unusual and unique to this system.⁽⁹¹⁾ The authors found a dihedral angle of 135° between the second phase and the yttria grain boundary instead of the usual 0° angle indicative of complete

wetting during liquid phase sintering. The $\text{Y}_2\text{O}_3\text{-MgO}^{(92)}$ phase diagram (Figure 28) indicates that at the sintering temperature used, 2100°C , there should be no liquid phase at less than ~ 1.3 wt% MgO. At lower temperatures no liquid phase would be expected.

The sintering mechanism for pure Y_2O_3 has not been determined. Preliminary experiments in this work showed that Y_2O_3 does coarsen when fired in air and that the addition of small amounts of MgO does increase its density. Study of pure and MgO-doped Y_2O_3 should allow evaluation of the usefulness of the proposed techniques in giving a better understanding of a relatively unknown system. Of particular interest is whether the dramatic effects of small MgO additions to Al_2O_3 are unique to that system or if MgO might behave similarly in other systems.

2.5.3 SiC - C - B

Silicon carbide and other covalent ceramics are prime candidates for high temperature, high stress structural applications, e.g., advanced heat engines. These materials were once thought to be unsinterable, since significant densification could be achieved only under hot pressing conditions.⁽⁴⁶⁾ Prochazka^(93,94) was the first to show that submicron-sized β -SiC could be sintered to high density with the addition of a small amount of boron and that densification could be further improved by the presence of free carbon.

Prochazka suggested that pure SiC does not sinter due to a high grain boundary energy to surface energy ratio.⁽⁹⁵⁾ He attributed the effect of carbon to its ability to remove free Si (remaining from the reaction forming SiC from Si) and SiO_2 (an oxidation product on the surface of the SiC particles) from the system. Removing the silica layer would increase the surface energy. He further suggested that boron segregates to the grain boundaries, reducing the boundary

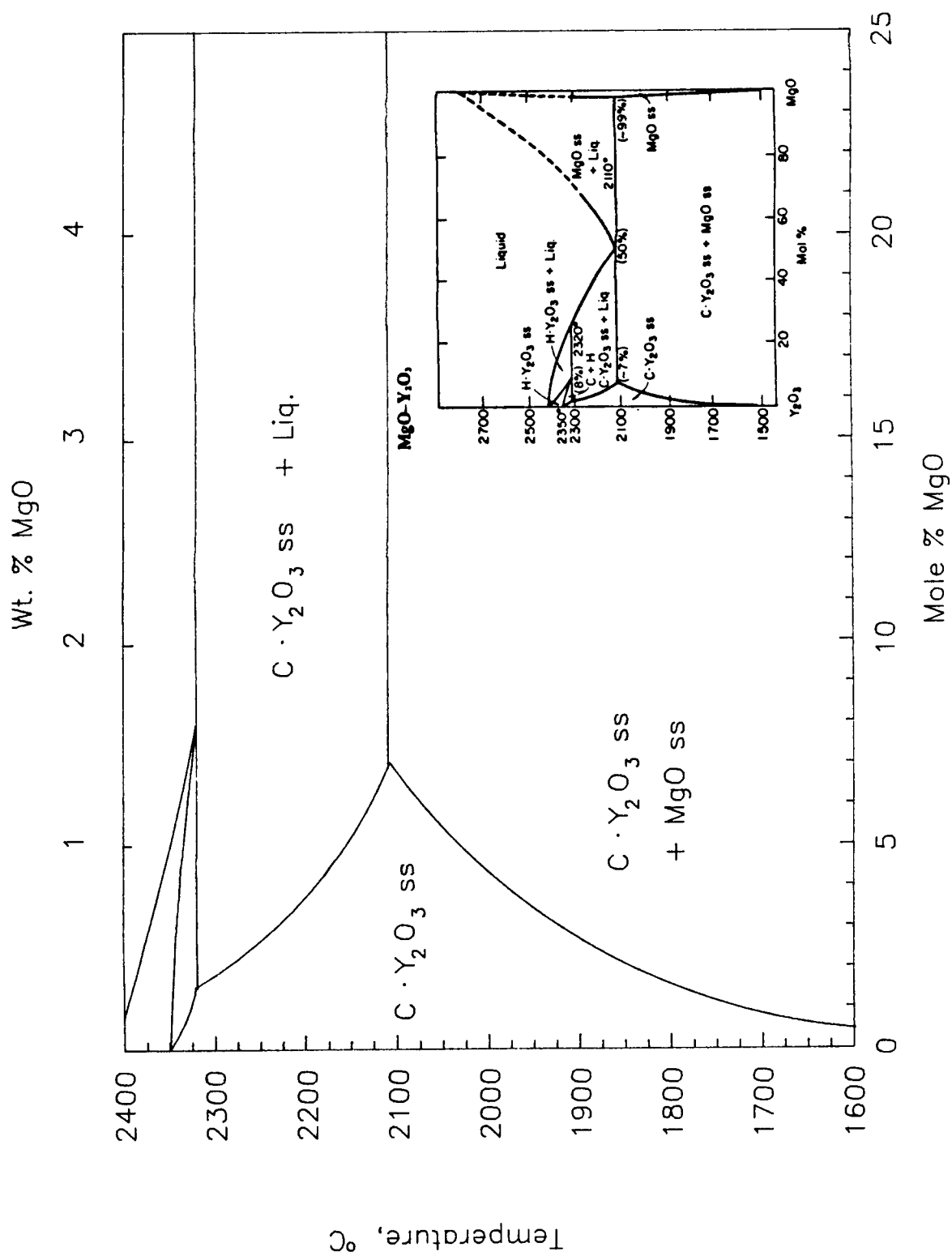


Figure 28. $\text{MgO} - \text{Y}_2\text{O}_3$ phase diagram (Ref. 92)

energy.⁽⁹⁵⁾

Greskovich and Rosolowski⁽⁴⁶⁾ showed that SiC containing only carbon underwent surface area reduction, but no densification, while SiC containing both carbon and boron had both surface area reduction and shrinkage. They attributed this behavior to a reduction in surface diffusion by boron, which would inhibit coarsening at low temperatures but still allow densification at high temperatures. They also observed locally dense regions and dihedral angles $\geq 100^\circ$, implying that densification is possible and may not be energetically limited. It has recently been suggested⁽⁹⁶⁾ that since microanalytical investigations have revealed no evidence of boron segregation at grain boundaries, boron in solid solution in SiC may significantly reduce the activation energy for diffusion and increase the rate of transport contributing to densification. The role of carbon and boron in enhancing densification of SiC is still not certain.

Low sintered densities are also obtained when abnormal grain growth of plate-like α -SiC occurs, due either to the $\beta \rightarrow \alpha$ transformation^(97,98) or to a very high sintering temperature for α -SiC powder.⁽⁹⁹⁾ This problem can be eliminated by control of the sintering conditions, i.e., lower sintering temperature and shorter time.

Since SiC is known to show nearly pure coarsening behavior without sintering additives, and mixed coarsening and densification in the presence of carbon and boron, it should be a good material for evaluation of techniques to measure coarsening during sintering. A better understanding of the microstructural development during sintering is also of great interest because of the impact of microstructure on mechanical properties.

CHAPTER 3

EXPERIMENTAL PROCEDURES

3.1 POWDER PREPARATION

3.1.1 Alumina

The alumina powder used^a was a high alpha content, alum-derived material with a nominal surface area of $6 \text{ m}^2\text{g}^{-1}$. Spectrographic analysis detected 20 ppm Fe, 20 ppm Na and 60 ppm Si in one sample and no impurities above the level of detectability ($<1 \text{ ppm}$) in two other samples. Additions of MgO (100 ppm) were made to the powder using a solution of $\text{Mg}(\text{NO}_3)_2 \cdot 6\text{H}_2\text{O}$ ^b in ethanol; the additive level of 100 ppm was chosen to give a value lying below the solid solution limit⁽¹⁰⁰⁾ of MgO in Al_2O_3 (125 ppm) at the selected firing temperature (1525°C). The alcohol/powder slurry was dried under an infrared lamp and then mixed for 15 minutes in a plastic jar with three 9-mm methacrylate balls in a multidirectional mixer.^c The powder was then passed through a $160 \mu\text{m}$ plastic sieve to help break up agglomerates. It was finally calcined in a covered platinum crucible for one hour at 600°C to convert the nitrate to MgO and again sieved. The undoped powder was treated in an identical manner except that no magnesium nitrate was added to the alcohol.

Some agglomerates remained; however, the particle size calculated from BET

a. Alumine A6Z, Ref. 12-2524, Criceram, B.P. 108, 92303 Levallois Perret Cedex, France.

b. Analar grade, BDH Chemicals Ltd., Poole, Dorset.

c. Spex, Glen Creston, Stanmore.

measurements ($0.2\ \mu\text{m}$) was nearly that observed (Figure 29) by transmission electron microscopy ($0.1 - 0.2\ \mu\text{m}$ for unagglomerated particles).

3.1.2 Yttria

The yttria powder^a contained no detectable (limit of detectability $<1\ \text{ppm}$) cation impurities in two spectrographic analyses and 40 ppm Al, 30 ppm Ca and 30 ppm Si in another. It also contained 0.014% S, as determined by the standard combustion method. The surface area was $6.8\ \text{m}^2\text{g}^{-1}$. This is a highly agglomerated powder as is typical of commercial Y_2O_3 powder⁽¹⁰¹⁾ as a result of the purification process which involves precipitation from solution and thermal decomposition. The particles are $3 - 5\ \mu\text{m}$ in size (Figure 30A) with each particle being composed of ultrafine crystallites $<0.05\ \mu\text{m}$ in size (Figure 30B). Addition of MgO (0.2 mole %) and calcination were carried out as described above for alumina. This amount of MgO would be expected to be below the solid solubility at the sintering temperature of 1850°C (Figure 28).

3.1.3 Silicon Carbide

This α -SiC powder^b contained the following impurities:

Al: 780 ppm	B: 40 - 50 ppm
Ca: 200 - 210 ppm	Fe: 240 - 250 ppm
Mg: 40 - 50 ppm	Ti: 150 - 170 ppm
V: 130 - 170 ppm	O: 0.5%
free C: 1.94 %	

a. Gold Label 99.99% Y_2O_3 , Lot 0506DJ, Aldrich Chemical Co., Milwaukee, WI, USA

b. A10 Type I α -SiC, Hermann C. Starck, New York, NY, USA.

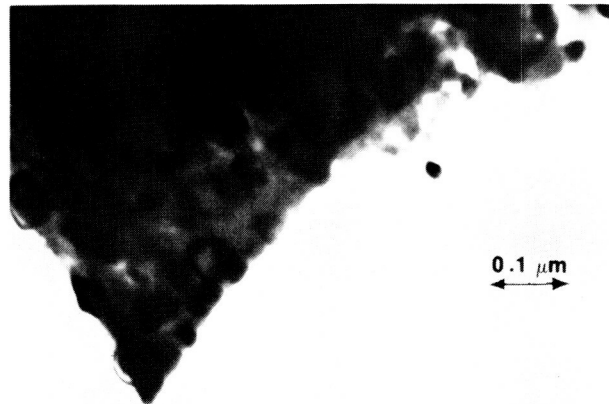


Figure 29. Transmission electron micrograph of calcined alumina powder. (1 hr., 600°C in air)

ORIGINAL PAGE IS
OF POOR QUALITY



A



B

Figure 30. As-received yttria powder. (A) Scanning electron micrograph (B) Transmission electron micrograph showing crystallites within a powder particle.

The cations were determined by spectrographic methods and the oxygen and free carbon by standard combustion methods. The surface area was $20.5 \text{ m}^2\text{g}^{-1}$. Transmission electron microscopy showed many particles to be flake-like with a size from $0.03 - 8.0 \text{ }\mu\text{m}$ (Figure 31A), however, it can be seen in the SEM photograph (Figure 31B) that, in general, the particles are angular and approximately equiaxed.

Carbon^a (0.5 wt.%) in the form of a resin and amorphous boron^b (0.5 wt.%) were added as sintering aids to a portion of the SiC powder. Carbon resin was dissolved in ethanol, boron was added and the mixture was milled for ~10 min. Two hundred grams of SiC were added and the mixture was milled for 72 hours in a 1 liter polyethylene jar containing 400 g of 12 mm diameter \times 12 mm high cylindrical SiC media and 500 ml 200-proof ethanol. The powder/ethanol slurry was dried on a hot plate at $150^\circ - 200^\circ\text{C}$. It was then remilled dry to reduce agglomeration and sieved through a $150 \text{ }\mu\text{m}$ screen. The undoped powder was treated in the same manner except for the addition of the sintering aids.

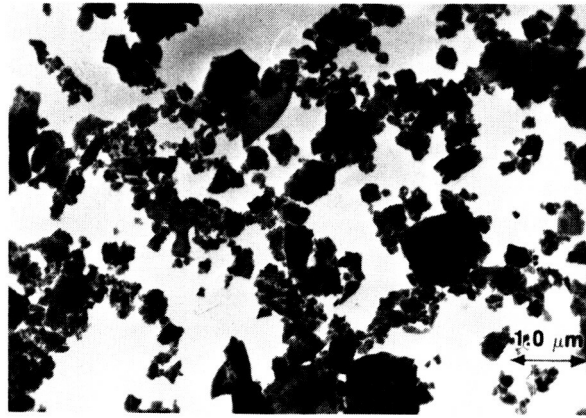
3.2 ANNEALED POWDERS

To assess the degree of coarsening in loose powders at early stages in the sintering process, Y_2O_3 and $\text{Y}_2\text{O}_3/\text{MgO}$ powders were put into high purity alumina tubes, the ends filled with Al_2O_3 fiber and annealed for 1 hour at temperatures of 1100° to 1600°C . Samples were inserted directly into the hot furnace and removed to air cool at the end of the annealing time.

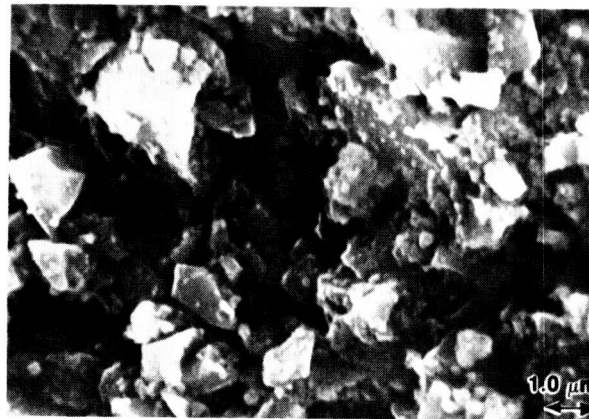
a. 22352 Resin, Hooker Chemical Co., Durez Div., North Tonawanda, NY, USA.

b. 99.5% amorphous boron, Cerac, Inc., Milwaukee, WI, USA.

ORIGINAL PAGE IS
OF POOR QUALITY



A



B

Figure 31. As-received SiC powder. (A) TEM micrograph showing many flake-like particles. (B) SEM micrograph of fracture surface of green compact; most particles are equiaxed. Both photographs show a very wide particle size distribution.

3.3 TRANSMISSION ELECTRON MICROSCOPY

The annealed Y_2O_3 powders were observed by TEM to evaluate early coarsening behavior. TEM samples were prepared by dispersing powder over a glass slide and evaporating a thin layer of carbon (~20 nm) onto the slide. The carbon film enclosing the powder particles was floated off in a beaker of cold distilled water. Sections of the film were then supported on 400 mesh copper grids and examined in a transmission electron microscope^a at 200 kV.

3.4. SINTERING

3.4.1 Alumina

Alumina and Al_2O_3/MgO powders dampened with a small amount of ethanol were isostatically pressed in latex tubing (thoroughly washed to remove any powder applied to prevent the walls of the tubing sticking together) at ~28 MPa to a green density of ~30% of theoretical. Samples were dried under an infrared lamp before sintering. Samples of some 0.65 - 1.0 g were sintered on covered high purity Al_2O_3 boats in a furnace^b with $MoSi_2$ heating elements and a ZrO_2 lining at 1525°C for times of 3 to 270 minutes to achieve a range of densities. They were inserted directly into the hot furnace and removed at the end of the sintering time to air cool.

a. JEOL 200CX, Japan Electron Optics Ltd., Tokyo, Japan.

b. Kanthal Super Rapid High Temperature Furnace, Bulten-Kanthal AB, Hallsthammar, Sweden

3.4.2 Yttria

Yttria and $\text{Y}_2\text{O}_3/\text{MgO}$ powders were isostatically pressed in the same way as the alumina powders except that the pressure was ~ 140 MPa. Samples of ~ 1.5 g were placed on a bed of $\text{ZrO}_2/1$ wt.% Y_2O_3 powder on a high purity alumina boat and sintered in an externally RF heated alumina tube^a furnace at 1850°C for times of 2.5 - 120 minutes. They were inserted into the hot zone in ~ 7 minutes and removed over a similar time to air cool.

3.4.3 Silicon Carbide

Approximately 2.6 g of SiC powder were dry pressed at 83 MPa in a double-acting tungsten carbide-lined die. Pressed bars were vacuum sealed in thin walled latex tubing and isostatically pressed at 423 MPa resulting in a final bar size of $\sim 37 \times 8 \times 5$ mm. Bars were heated at a rate of $50^\circ\text{C min}^{-1}$ in flowing argon in a graphite susceptor induction furnace^b and sintered for hold times of 0 to 40 minutes after reaching 2050°C . At the end of the hold time, the furnace was turned off and the bars allowed to cool slowly.

3.5 DENSITY MEASUREMENT

The densities of sintered Al_2O_3 and Y_2O_3 samples were measured by standard water immersion techniques.⁽¹⁰²⁾ The sample was suspended in a holder of weight H, made of thin platinum wire attached to nylon thread. Specimens were soaked overnight in distilled water with 0.3% by volume wetting agent added to ensure

a. Purox, Morgan Matroc, Ltd., East Mosley, Surrey.

b. Heraeus Inc., W. Conshohocken, PA, USA.

that all open porosity was filled. In this method, the sample is weighed dry, D , suspended in water, S , and saturated with water, W , after excess surface water is blotted off with a damp cloth. The bulk density is calculated by:⁽¹⁰²⁾

$$B = \frac{D}{W - (S - H)} \rho_{H_2O} \quad (31)$$

The density of the SiC bars was measured using a small piece of the bar by the standard pycnometric method involving evacuation of a pycnometer containing the specimen, followed by mercury intrusion and measurement of the amount of mercury displaced by the sample. The calculation is similar to Equation 31.

3.6 BET SURFACE AREA MEASUREMENT

The surface area per unit mass S_m of both the annealed powders and the sintered samples was measured by the standard three-point gas adsorption method.⁽¹⁰³⁾ Two types of instrumentation are commonly employed for such surface area determinations.⁽¹⁰⁴⁾ In one,^a (used here for the Al_2O_3 and Y_2O_3 samples) the adsorbate gas is adsorbed onto the sample at slightly above liquid nitrogen temperature ($-196^\circ C$) from a flowing mixture of adsorbate and an inert nonadsorbable carrier gas (helium). The adsorbate is desorbed at ambient temperature. The process of adsorption and desorption is monitored by measuring the change in the thermal conductivity of the gas mixture.

In the other method,^b (used here for the SiC samples) the volume of the chamber containing the sample is determined by filling the chamber, at liquid nitrogen temperature, with helium and measuring its pressure and comparing that

a. Quantasorb, Quantachrome Corp., Syosset, NY, USA.

b. Accusorb 2100E, Micromeritics, Norcross, GA, USA.

pressure to the pressure of the same volume of helium in a chamber of known volume. After evacuation, the procedure is repeated with the adsorbate gas. The amount of adsorbed gas can be determined from the pressure difference.

The adsorbate gases are usually either nitrogen or krypton. For measurement of very low surface areas, it is recommended⁽¹⁰⁴⁾ that krypton be used, especially in the volumetric type apparatus where the low saturation vapor pressure of krypton allows more accurate measurement since a higher proportion of the gas admitted to the chamber is actually adsorbed. The gas flow apparatus is designed to be particularly satisfactory for low surface area measurements because each measurement is calibrated with a known volume of gas. Nitrogen was used to measure the Al_2O_3 and Y_2O_3 surface areas and krypton to measure the surface area of the SiC.

BET measurements require continuous porosity open to the surface to allow gas penetration and are therefore reliable up to ~90% of theoretical density.

3.7 SPECIMEN POLISHING

In practice, it is very difficult to polish samples without some pull-out or smearing. These polishing artifacts affect the measurement of microstructural features; thus, the volume fraction of porosity measured by quantitative microscopy will not be exactly the same as that measured by the immersion technique. This difference can be accommodated by polishing samples until they measure to within a few percent of the immersion porosity and then normalizing the surface area measurements to the immersion porosity values.⁽¹⁰⁵⁾

3.7.1 Alumina

The sintered Al_2O_3 samples were ground and polished^a for quantitative microscopy. Samples with $>\sim 10\%$ porosity were impregnated with a warm epoxy resin^b under vacuum. All samples were mounted with black wax on aluminum stubs. They were first ground on a 20 μm resin-bonded diamond disk^c followed by rough polishing with 15 μm diamond on a PellonTM lap^d using an alcohol-based lubricant.^e Polishing began with 6 μm diamond spray on an epoxy lap^f using an oil/water emulsion lubricant,^g followed by 3 μm and 1 μm diamond spray on PellonTM. All times were ~ 3 minutes at force settings of 2 or 3.

3.7.2 Yttria

Yttria samples were mounted in epoxy resin^b and ground until flat on 320 grit SiC paper. They were then ground on 600 grit, 10 μm and 5 μm SiC paper for 1 minute each followed by polishing for 1 minute on a textured cloth^h with 3 μm diamond and finally for 1 minute on a flat woven clothⁱ with 1 μm diamond.

3.7.3 Silicon Carbide

Samples at least 80% dense were mounted in epoxy resin^b and ground until flat on, consecutively, 120, 220 and 600 mesh resin bonded diamond disks.^c They were then lapped on a metal/epoxy disk^j using an oil-based lubricant and 15 μm

-
- a. Planapol-2, Pedemax 2, Struers Scientific Instruments, Copenhagen, Denmark.
 - b. Epofix, Struers Scientific Instruments, Copenhagen, Denmark.
 - c. Struers Scientific Instruments, Copenhagen, Denmark.
 - d. Pan W Pellon, Struers Scientific Instruments, Copenhagen, Denmark.
 - d. Struers Blue, Struers Scientific Instruments, Copenhagen, Denmark.
 - f. Petrodisk, Struers Scientific Instruments, Copenhagen, Denmark.
 - g. Struers Red, Struers Scientific Instruments, Copenhagen, Denmark.
 - h. AP-Chemotext, Struers, Inc, Strongsville, Ohio, USA.
 - i. MOL-cotton woven, Struers, Inc, Strongsville, Ohio, USA.
 - j. Petrodisc-M, Struers, Inc, Strongsville, Ohio, USA.

diamond, followed by 9 μm diamond. Next they were lapped on an epoxy disk^f with an oil-based lubricant^g using 6 μm diamond and, finally, on a flat woven cloth using 1 μm diamond.

Specimens less than ~80% dense were mounted in epoxy and ground on, successively, 240, 320 and 600 grit and 10 μm SiC paper. They were polished on 3 μm and 1 μm diamond using the same procedure used for the denser SiC samples.

3.8 ETCHING

For accurate quantitative microscopy, care must be taken to avoid excessive rounding of the grains or other damage to the polished surface.

3.8.1 Alumina and Yttria

All sintered samples were lightly thermally etched in air before grain boundary measurements were made. Alumina samples were etched for 15 minutes at 1400°C; yttria samples were etched for 15 minutes at 1450°C.

3.8.2 Silicon Carbide

Samples at least 80% dense were etched for 5 minutes in a fused salts mixture of 3 parts NaF to 7 parts K_2CO_3 .

Porous SiC is extremely difficult to etch because the etchant tends to dissolve particle surfaces at pores before etching the grain boundaries.⁽¹⁰⁶⁾ The etchant used for the dense samples was very destructive to the porous samples. The most

f., g. see page 76.

successful procedure was to immerse the samples for 3 - 10 minutes in boiling Murikami's solution: 60 g KOH, 60 g $K_3Fe(CN)_6$ and 120 ml H_2O . However, few of even these samples were useful for quantitative microscopy. A molten salt mixture of 1 part NaF to 9 parts K_2CO_3 was successful enough to show some grain boundaries on replicas made for scanning transmission electron microscopy, but the quality was still not good enough for quantitative microscopy.

Thermal etching in pure or Ti-gettered argon has been found in some instances to etch porous SiC,⁽¹⁰⁶⁾ however, the suggested 0.5 hours at 1550°C did not etch these samples. Heating in nitrogen at temperatures of 1850°C or 1950°C for up to 2 hours also did not reveal the grain boundaries.

3.9 SCANNING ELECTRON MICROSCOPY

Due to the small particle and pore sizes, often sub-micron, it was necessary to make measurements on SEM^{a,b} rather than light micrographs. However, the large depth of focus of the SEM makes it difficult to determine with certainty which particles are actually in the plane of polish, especially for samples with >~30% porosity. This problem can be minimized by using a short working distance; high contrast photographs are also helpful.

3.10 STEREOLOGY

Measurements were made on scanning electron micrographs mainly by point counting techniques and values were calculated by standard stereological

a. S700, Hitachi, Tokyo, Japan

b. 1200B, Amray, Inc., Bedford, MA, USA

equations.^(66,107,108,109) Measurements were made either directly on photographs or on projected images of negatives. In either case, a grid of lines and points was overlaid on the micrograph and the requisite points counted. Statistical reliability, of course, requires that each sample area be randomly selected and representative of the entire structure. This also requires that photographs be taken at a magnification that will clearly show all the features to be measured.

Point counting can be done either manually or by use of an image analyzer. The semiautomatic image analyzer used in this work^a consists of a microcomputer, keyboard, monitor, digitizing tablet, transducer pen and software for data acquisition and statistical and stereological evaluation. The photograph was laid on the digitizing tablet and points counted or distances measured by means of interaction between the transducer-containing pen and the electrical or magnetic tablet.

The grid⁽¹¹⁰⁾ overlay used (Figure 32) is a computer generated rectangular pattern of equispaced points connected by lines. The unique feature of this grid that improves counting accuracy is that each point is left open so that the phase at that exact point can be seen clearly. For statistical accuracy, the point spacing, adjustable with this program, should be such that, on average, only one point falls on each feature to be counted or that only one line crosses each feature.⁽¹⁰⁷⁾

3.10.1 Volume Fraction

Using point counting methods, the volume fraction V_v of a phase is simply the ratio of the number of grid points falling on the phase of interest (in this case, pore or solid) to the total number of grid points.⁽¹⁰⁷⁾ For example, in Figure 33, 31 of the 130 grid points fall on pores, giving a volume fraction of porosity of

a. Kontron MOP-Videoplan, Reichert-Junk U.K., Slough, U.K.

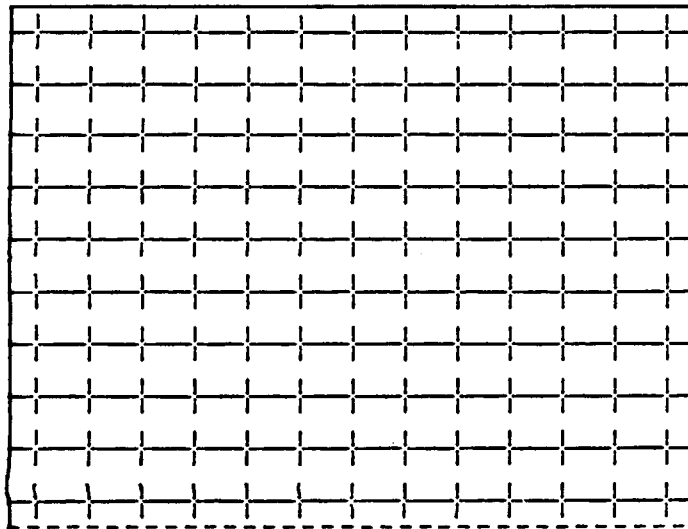


Figure 32. Example of grid used for point counting for stereological analysis. The advantage of this grid is that the points are open, allowing an accurate view of the underlying phase. Computer generation allows the grid spacing to be sized as required.

ORIGINAL PAGE IS
OF POOR QUALITY

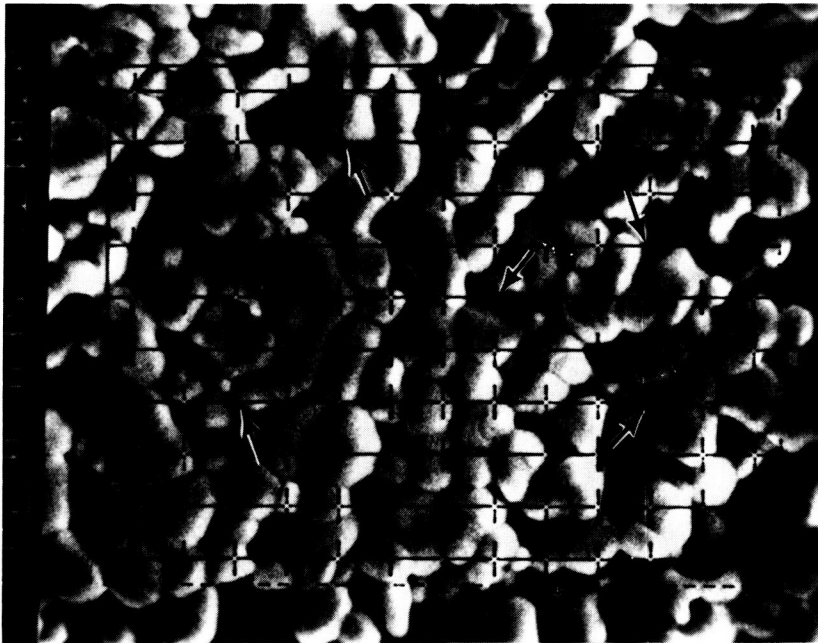


Figure 33. Example of point counting procedure to determine volume fraction. Arrows mark points on pore phase.

0.24; the volume fraction of solid is thus 0.76. Care must be taken to count only points on the plane of polish; that is, solid that is visible within a pore is not counted as solid, but as pore volume. This differentiation becomes more difficult as the volume fraction of porosity increases. Using a short working distance when taking the SEM photographs will help by reducing the depth of focus so that material within the pores cannot be seen so easily.

Weibull⁽⁶⁶⁾ has developed a chart that can be used to determine the approximate number of points that must be counted to achieve the desired relative standard error (RSE)* of the volume fraction measurement, in this work $\sim < 5\%$. For example, to ensure a RSE of 5%, 7600 test (grid) points are needed for $V_v = 0.05$, but only 1200 at $V_v = 0.25$. The required number of test points is divided by the number of points per grid to determine the number of microstructural areas (photographs) to be evaluated. The actual relative standard error is determined upon completion of the point counting by standard statistical methods. Additional areas can then be evaluated if the relative standard error is too large.

3.10.2 Surface Density

The surface density, S_v , is the amount of surface area of a structure in a unit volume. The surface density of any isotropic structure is related to the number of intersections per unit length of test line of the test (grid) line (The points on the grid are not needed in this case.) with the line formed by the intersection of the plane of polish with the surface of interest by⁽⁵³⁾

$$S_v = 2I_L \quad (32)$$

This surface can be entirely interconnected (e.g., that of open, interconnected

* Standard error is another term for standard deviation. The RSE is the standard error as a percent of the mean value being measured.

porosity) or the total surface area of individual particles (e.g., isolated second phase particles or pores). Points such as those labeled A on Figure 34 are counted to measure the pore/solid interfacial area, S_V^p ; points such as those labeled B in Figure 34 are counted to calculate grain boundary area, S_V^{gb} .

The chart developed by Weibull⁽⁶⁶⁾ was used to estimate the total test line length needed to achieve a relative standard error of the value of S_V of $\sim < 5\%$ and then the actual RSE was calculated by standard statistical methods.

3.10.3 Shape Factor

Grain shapes can be compared by evaluation of the form (shape) factor:⁽¹¹¹⁾

$$F_s = \frac{3C}{S/V} = \frac{3\pi^3 NA}{8U^2} \quad (33)$$

where C is the mean curvature and S/V is the ratio of the surface of the particles to the volume of the particles, or in terms of values measured in areal analysis, N is the number of particles in the test area, A the sum of the particle areas and U the sum of the particle perimeters. The value of the form factor approaches 1 as the particle shape approaches spherical.

3.10.4 Triple Lines

Triple lines are formed in a structure by the intersection of three interfaces. In the case of a sintered material, the three interfaces can be either a grain boundary and the two adjacent pore/grain interfaces (e.g., intersection "A" in Figure 35) or the grain boundaries of three neighboring grains (e.g., intersection "B" in Figure 35). The first of these will be designated solid-solid-pore (ssp) and the second solid-solid-solid (sss). The length of such triple lines in a unit

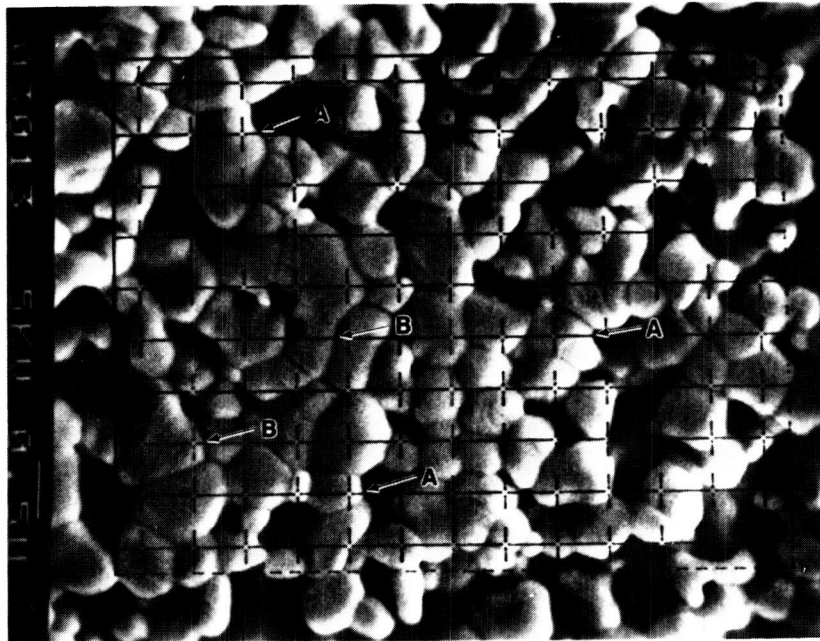


Figure 34. Example of surface area measurement by point counting. Intersections of grid lines with line formed by surface of interest and plane of polish are counted. Points such as those marked "A" are used to determine the pore/solid surface and points marked "B" the grain boundary area.

ORIGINAL PAGE IS
OF POOR QUALITY.

ORIGINAL PAGE IS
OF POOR QUALITY



Figure 35. Triple lines are formed by the intersection of three interfaces: (A) a grain boundary and the two adjacent pore/grain interfaces, and (B) the grain boundaries of three neighboring grains.

volume of structure, L_v^{ssp} or L_v^{sss} , is a measure of the extent of interaction of the interfaces. The length of triple line per unit volume, L_v , of sample is determined by the relation⁽¹⁰⁷⁾

$$L_v = 2P_A \quad (34)$$

where P_A is the average number of intersections the triple line makes per unit area of section plane. A reference area is marked on the photograph as in Figure 36 and all of the intersection points of the triple lines of interest within the area are counted. Points marked "A" in Figure 36 are intersections of two grains and a pore counted to evaluate L_v^{ssp} and points marked "B" are intersections of three grains counted to evaluate L_v^{sss} . Since there may be a large number of these points on a photograph, it is helpful to actually mark the points as they are counted. For these measurements, at least 1000 points were counted.

3.10.5 Mean Linear Intercept

The mean linear intercept in three-dimensional space, \bar{L}_3 , is one measure of particle size. There is no simple relationship between \bar{L}_3 and particle (or pore) "size" for irregularly shaped particles, however, since it is related to surface area and volume fraction by

$$\bar{L}_3^p = \frac{4V_v^p}{S_v^p} \quad (35)$$

(for separated particles - in this case pores), there is a unique value for each system which can be compared to that for similar systems.

The particle mean linear intercept can be determined from a similar equation:

ORIGINAL PAGE IS
OF POOR QUALITY

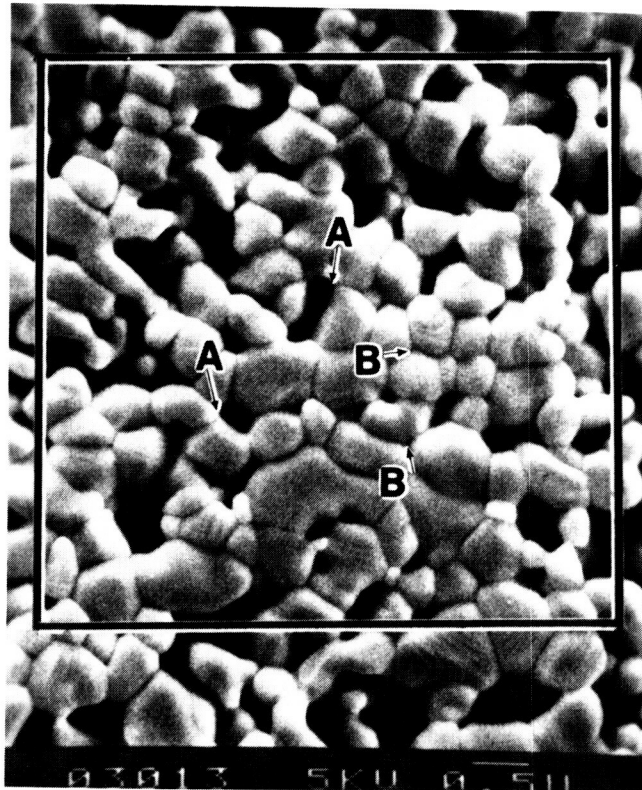


Figure 36. Example of the determination of triple line length by point counting. All points within the outlined area such as those marked "A" are counted to estimate solid/solid/pore intersection length. Points such as "B" are counted to estimate the three-grain intersection length.

$$L_3^g = \frac{4(1 - V_v^p)}{S_v^p + 2S_v^{gb}} \quad (36)$$

CHAPTER 4

EXPERIMENTAL RESULTS: ALUMINA

4.1 SINTERING

Isostatically pressed samples of Al_2O_3 , with and without MgO , were sintered for investigation of the coarsening behavior during sintering. Doped samples contained 100 ppm MgO , an amount within the solid solution limit at the sintering temperature. Samples were isothermally sintered in air at 1525°C for times of 3 to 180 minutes to develop a range of densities.

4.1.1 Density

The density achieved at each sintering time is shown in Figure 37. The MgO -doped sample reached a higher density in a given time than did the undoped sample, although it appears that the density of the doped Al_2O_3 may have reached a limit by 60 minutes whereas the density of the undoped material is continuing to increase even after 180 minutes.

4.1.2 Grain Shape Factor

Undoped alumina sometimes forms highly elongated grains during sintering,⁽³⁵⁾ although it has been shown⁽⁷⁷⁾ that such growth may be the result of the presence of a liquid grain boundary phase during sintering. Grain shapes can be compared by evaluation of the form (shape) factor⁽¹¹¹⁾ using equation 33; the value of the

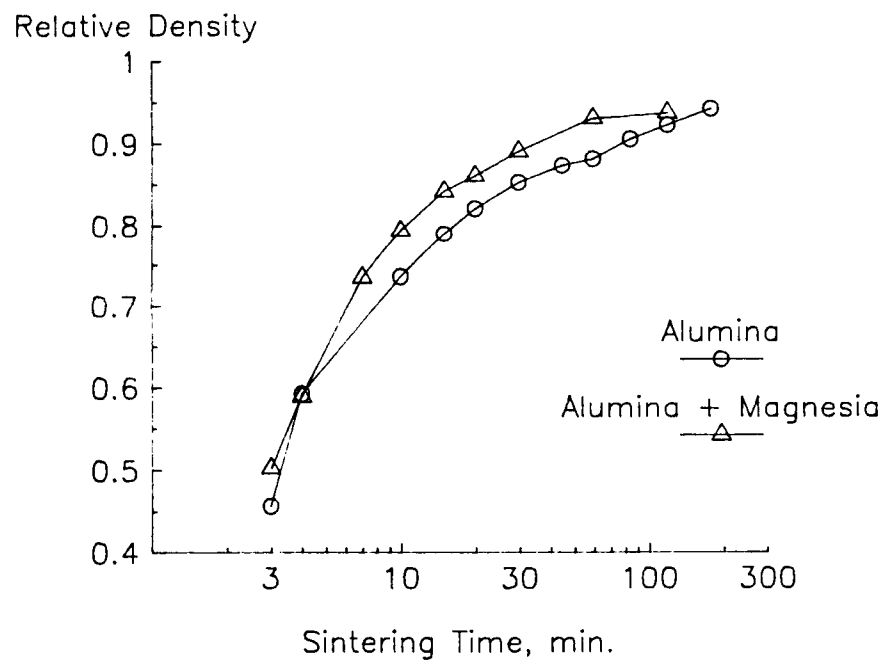


Figure 37. Density of compacts sintered at 1525°C.

form factor approaches 1 as the particle shape approaches spherical. Values of the form factor are plotted against density in Figure 38. It can be seen that the form factors for both MgO-doped and undoped alumina fall on the same line over the range of densities investigated; thus, the two materials are microstructurally comparable. Both grain structures appear to be becoming slightly less "spherical" as the density increases.

4.2 SURFACE AREA vs. DENSITY DIAGRAMS

4.2.1 Surface Area Measurement

The primary experiment in the present work was to explore the surface area/density diagram approach to understanding coarsening behavior. Two approaches to development of the diagram have been investigated: 1. BET gas adsorption measuring surface area per unit mass, S_m , and 2. quantitative stereology measuring surface area per unit volume, S_v^p . In both cases, the surface area measured is that of the pore/solid interface.

4.2.1.1 Surface Area vs. Density Diagram by BET

Surface area measurements by BET require that all porosity be open to the sample surface. This version of the diagram can thus be plotted for densities $< \sim 90\%$. Figure 39 shows that both the MgO-doped and undoped Al_2O_3 follow the same trajectory of decreasing pore/solid surface area with increasing density, indicating that the densification rate:coarsening rate ratio is the same for both materials.

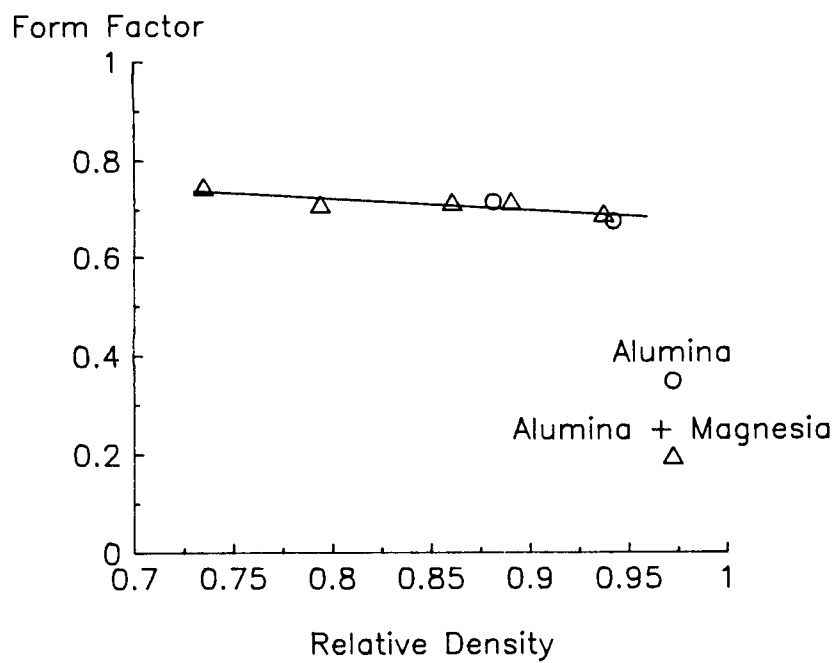


Figure 38. Form (shape) factor evaluated from curvature and specific surface area of grains. The value of the form factor approaches 1.0 as the grains become more spherical.

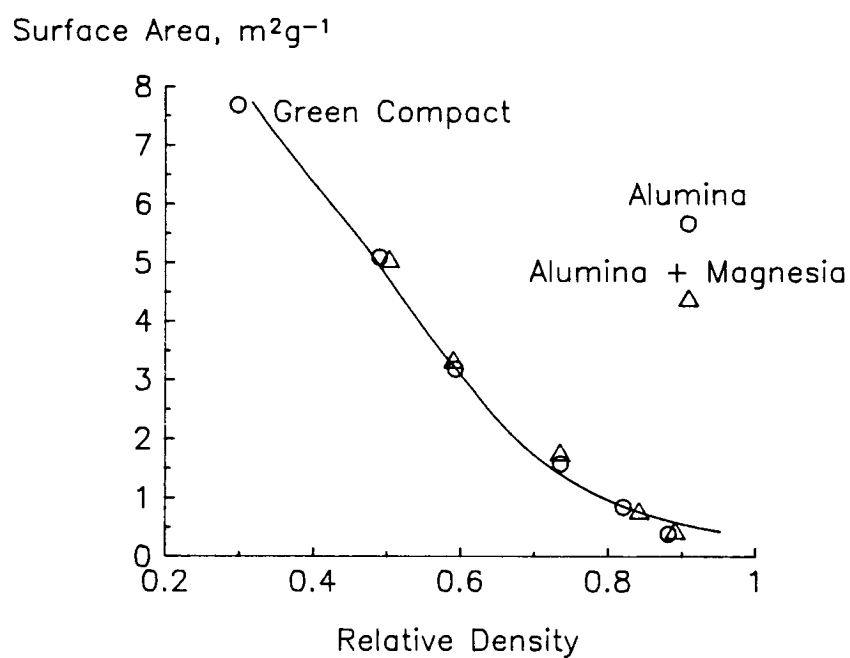


Figure 39. Specific surface area of sintered compacts as measured by gas adsorption. Both the doped and aluminas follow the same surface area reduction trajectory. All samples were sintered at 1525°C.

4.2.1.2 Surface Area vs. Density Diagram by Stereology

This method of measuring surface area uses data obtained from SEM photomicrographs of polished sections. Such measurements are most accurately made at high densities. Despite more scatter in the data than in the BET plot (Figure 39), this diagram (Figure 40) also shows the surface area reduction in both materials following the same trajectory and also suggests that the densification: coarsening ratio is unchanged by the addition of MgO as a solid solution sintering aid.

4.2.1.3 Comparison of Surface Area vs. Density Diagrams

BET gas adsorption measures surface area per unit mass, S_m , and quantitative stereology measures surface area per unit volume, S_v^p . These two values are related by

$$S_v^p = S_m \rho \quad (37)$$

where ρ is the actual density of the sample. Figure 41 shows that while the two techniques are broadly consistent, the values of S_v^p calculated from S_m are ~40% to 70% higher than the measured values with the disagreement being less at higher densities where the stereological measurements are more accurate.

4.2.2 Grain Boundary Area vs. Density Diagram

Another important aspect of coarsening is the reduction in grain boundary area. Quantitative stereology is the only one of the two techniques that can be used to measure the grain boundary area, S_v^{gb} . It is clear from Figure 42 that the extent of grain boundary area is changed by the addition of MgO. Samples with magnesia have a higher grain boundary area at a given density than do the undoped samples. The amount of grain boundary area in the undoped sample

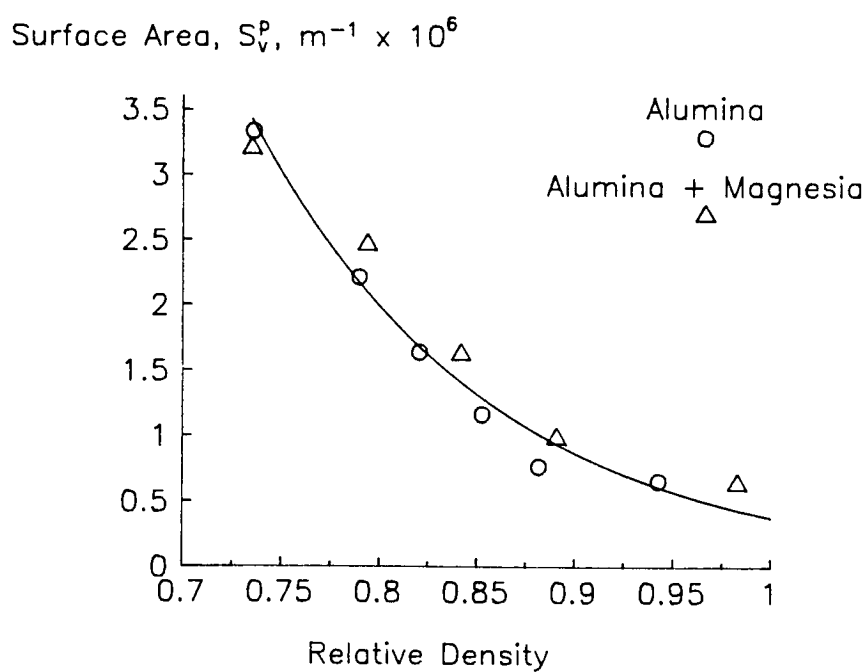


Figure 40. Specific pore/solid surface area per unit volume is not changed by doping alumina with 100 ppm magnesia.

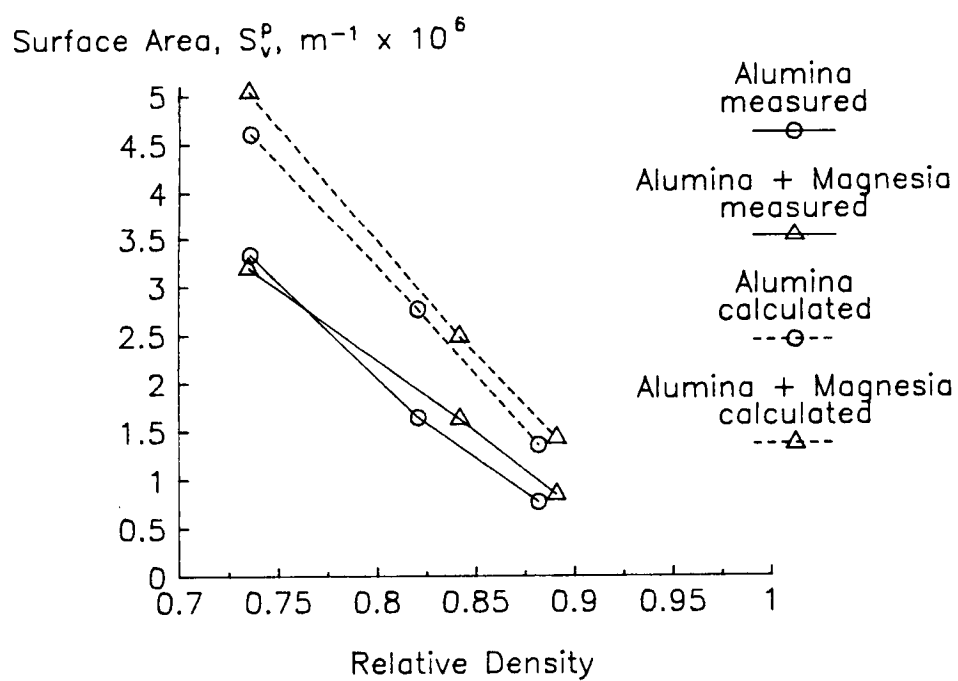


Figure 41. S_v^p measured compared to that calculated by $S_v^p = S_m \rho$

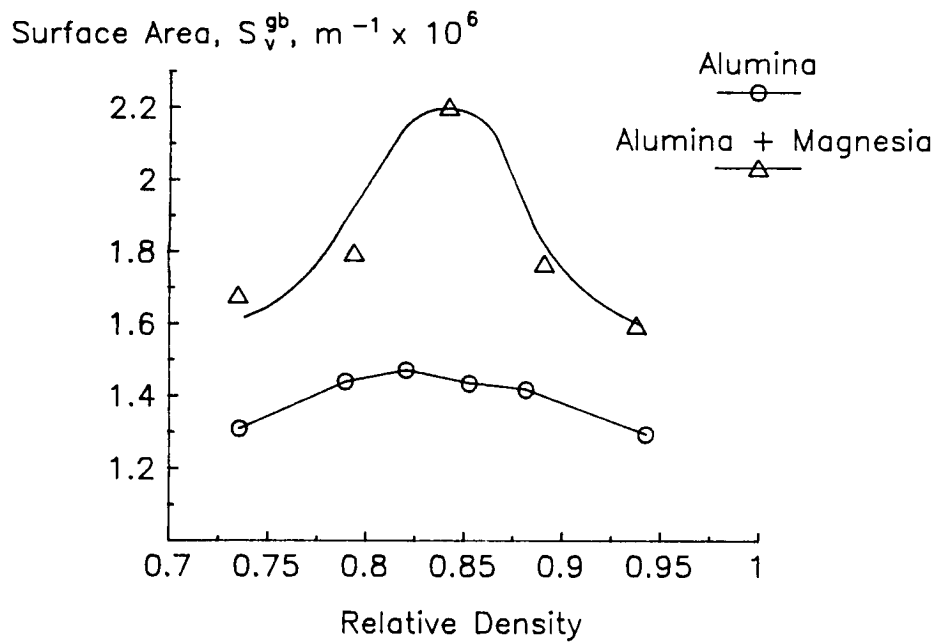


Figure 42. The specific grain boundary area of the undoped alumina is less than that of the MgO-doped alumina and also more constant as the density changes.

remains relatively constant over the range of densities evaluated, whereas the grain boundary area in the MgO-doped sample rises to a peak at 85% density that is nearly 40% greater than the area at the lower and higher densities.

4.3 ADDITIONAL STEREOLOGICAL EVALUATION

4.3.1 Length of Triple Lines

To consider further the effect of the additive on grain boundary area, it is helpful to distinguish between two categories of grain boundary, namely those that intersect pores (and which are consequently active in contributing to densification) (for example, "A" in Figure 43) and those which are entirely connected to other grain boundaries (e.g., "B" in Figure 43). Analysis of the two types of boundaries can be obtained by consideration of the length of triple line intersections they form in the structures, either solid-solid-pore (ssp) or solid-solid-solid (sss). The triple line length is obtained using the procedure in Section 3.10.4 and Equation 34.

4.3.1.1 Solid-Solid-Pore Triple Lines

The length of ssp triple line per unit volume as a function of density is plotted in Figure 44. The length of triple line first increases slightly, reaching a maximum at ~80% density, and then decreases with increasing density and is approximately the same at a given density for both the doped and undoped alumina, indicating that the excess grain boundary area in the MgO-doped alumina is not connected to the porosity and, therefore, does not contribute to densification.

ORIGINAL PAGE IS
OF POOR QUALITY

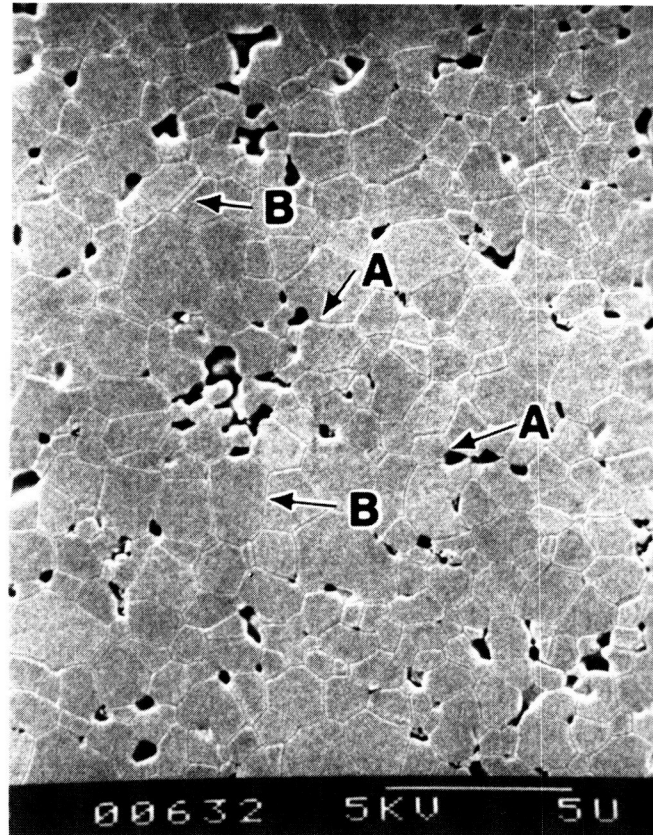


Figure 43. Two types of grain boundaries may be present in a sintered structure: (A) those that intersect pores and, (B) those connected only to other grain boundaries.

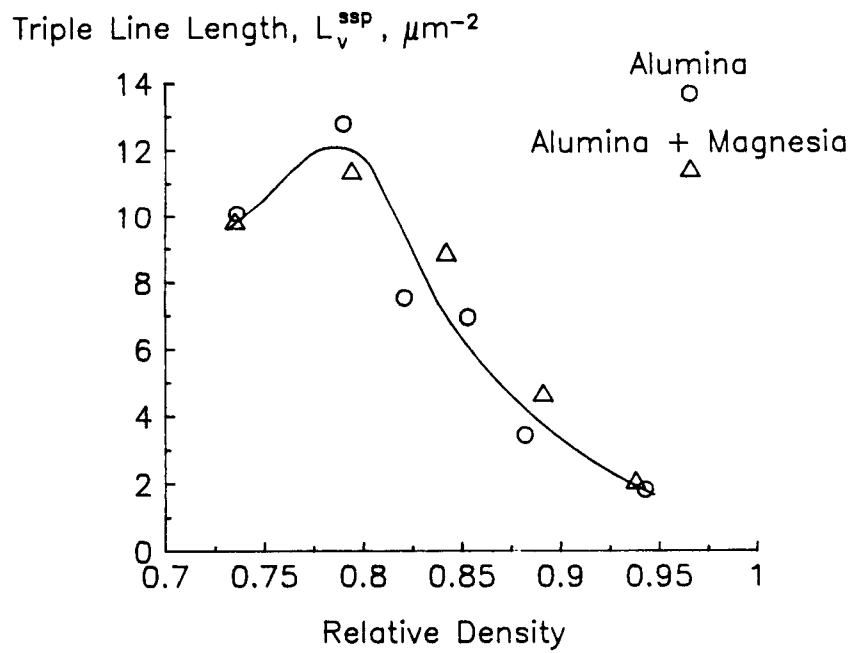


Figure 44. Length of grain/grain/pore intersection line per unit volume is the same for both the MgO-doped and undoped alumina.

4.3.1.2 Solid-Solid-Solid Triple Lines

The length of triple line per unit volume formed by the intersection of three grains is a measure of grain boundaries not connected to pores – those in fully dense regions. Figure 45 demonstrates that the MgO-doped alumina contains a greater length of three-grain triple line per unit volume than does the undoped material. In this case, the triple line length of each type of material increases to a maximum and then decreases with increasing density. The maximum for the undoped material is reached at a density of ~82% while the the maximum for the MgO-doped Al_2O_3 is not reached until a density of ~86%. The triple line length of the doped material decreases much faster until both materials have nearly the same value at ~94% density.

4.3.2 Mean Linear Intercept

The mean linear intercept, \bar{L}_3 , is one measure of particle size. There is no simple relationship between \bar{L}_3 and particle (or pore) "size" for irregularly-shaped particles, however, since it is related to surface area and volume fraction, there is a unique value for each system which can be compared to that for similar systems.

4.3.2.1 Mean Pore Intercept

The mean pore intercept can be evaluated with Equation 35 using the previously measured values for V_V^P and S_V^P . Since both materials have been shown to have the same pore surface area at the same density, values of S_V^P are taken from the solid line of Figure 40. Figure 46 is a plot of mean pore intercept vs. density of both materials, indicating that the pores grow to a maximum size at ~90% density and then begin to shrink.

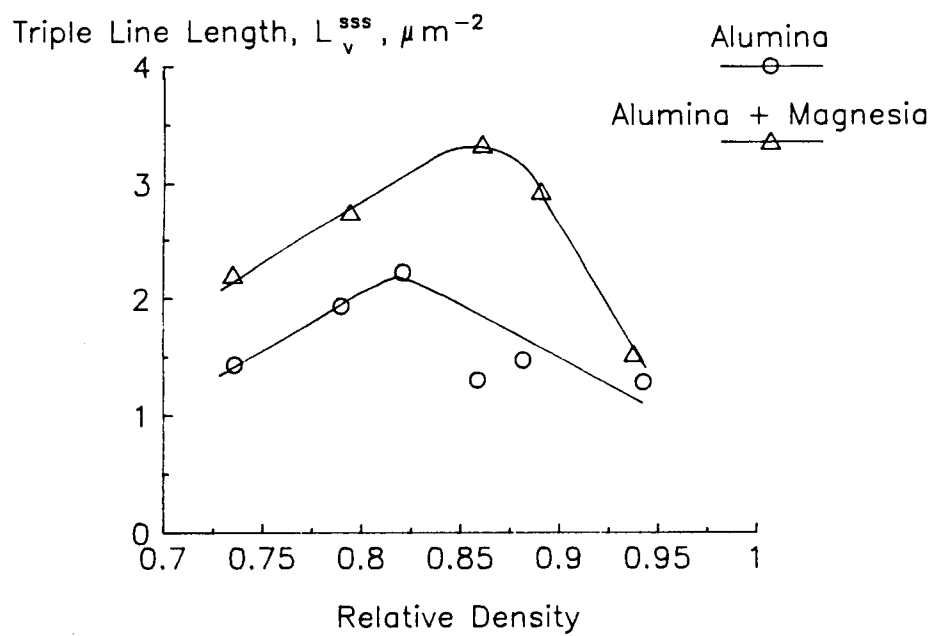


Figure 45. The length of triple line per unit volume formed by the intersection of three grains is a measure of grain boundaries in fully dense regions.

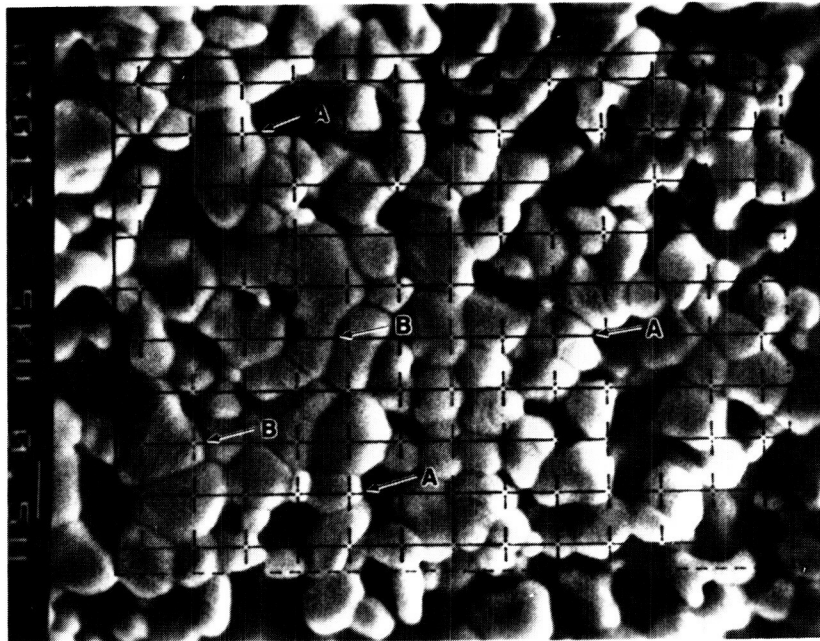


Figure 34. Example of surface area measurement by point counting. Intersections of grid lines with line formed by surface of interest and plane of polish are counted. Points such as those marked "A" are used to determine the pore/solid surface and points marked "B" the grain boundary area.

ORIGINAL PAGE IS
OF POOR QUALITY.

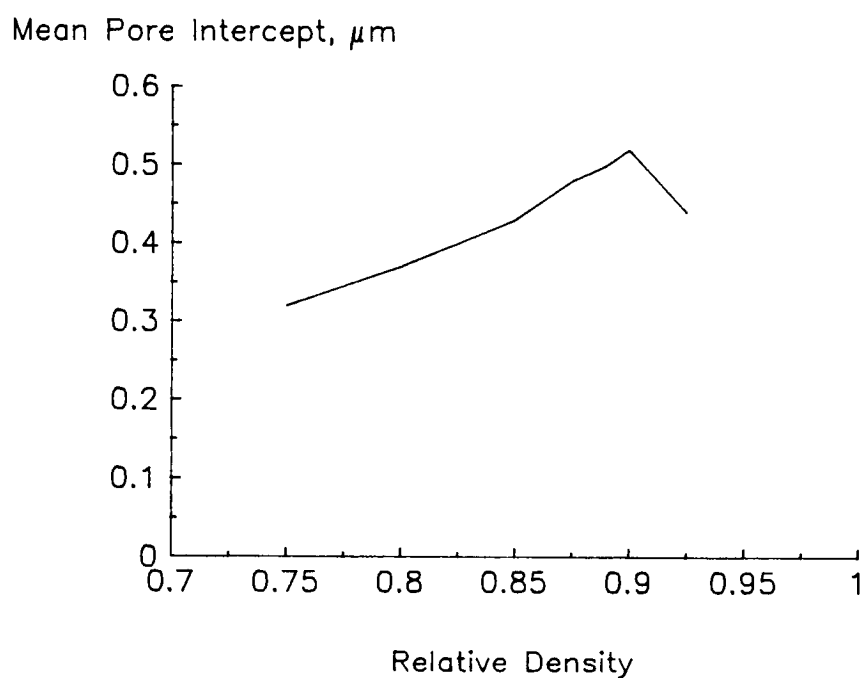


Figure 46. Mean pore linear intercept for both MgO-doped and undoped alumina evaluated by measuring the porosity and surface area. This measure of the pore size shows that the maximum pore size is at ~90% density.

4.3.2.2 Mean Grain Intercept

The mean grain intercept is determined by Equation 36. The values of \bar{L}_3^g for the doped and undoped Al_2O_3 shown vs. density in Figure 47 indicate that while, in both cases grain growth continues as the density increases, the grain size of the undoped alumina at a given density is ~20% greater than that of the MgO-doped material.

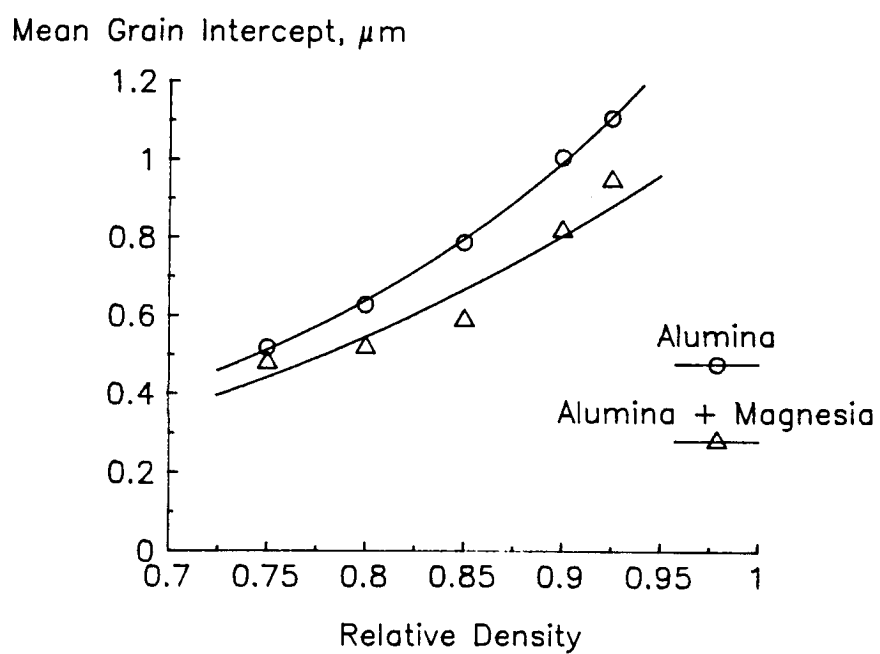


Figure 47. Mean grain linear intercept evaluated by measuring the density, S_v^{sp} and S_v^{gb} . This is a measure of the grain size.

CHAPTER 5

DISCUSSION: ALUMINA

5.1 EFFECT OF MgO ON THE DENSIFICATION:COARSENING RATIO

The dependence of the specific surface area (m^2g^{-1}) as measured by BET on the density of the sintered compact is shown in Figure 39. It can be seen that, just as in the case where the additive is used at levels above the solid solution limit,⁽⁵⁵⁾ no difference is observed between the doped and the undoped materials. The conclusion may be drawn therefore that magnesia does not affect the coarsening:densification ratio in alumina.

In the light of some evidence⁽⁵⁰⁾ that the densification rate is enhanced by the presence of the additive, this conclusion suggests that a similar change must occur in the coarsening rate either because of similar controlling mechanisms for both processes or because of a similar additive dependence of two distinct processes. Consider the mechanism for grain growth in very porous (initial and intermediate stage) compacts suggested by Greskovich and Lay,⁽⁴³⁾ in which a grain boundary moves through the smaller of two adjacent particles after the neck fills to the point that the boundary curvature allows the boundary to become mobile. Grain growth can thus be the result of any neck-filling diffusion mechanism. They present evidence from other work that initial stage neck growth in Al_2O_3 occurs primarily by surface diffusion, a process that cannot account for the increased densification rate. Scratch annealing studies⁽⁸⁰⁾ have suggested that MgO reduces D_s rather than increasing it as required here for an enhanced coarsening rate. In a final stage, nearly dense microstructure, coarsening (grain

growth) may be partially controlled by the ability of pores attached to grain boundaries to move with boundaries. In this case also, densification and coarsening may be controlled by the same process (for instance, lattice diffusion controlled densification and pore drag controlled grain growth where the pores move by lattice diffusion from the front wall to the back⁽¹¹²⁾) or by a similar additive dependence of two different processes (say lattice diffusion for densification and surface diffusion for pore drag). The great uncertainty concerning coarsening processes in alumina compacts and the possibility that the controlling mechanism may change as grain growth occurs preclude closer interpretation.

A plot similar to Figure 39 but with the data now obtained by quantitative microscopy (and therefore in terms of the specific surface area density $\text{m}^2 \text{m}^{-3}$ or m^{-1}) is given in Figure 40. The span of accessible densities is now smaller as a consequence of the need to prepare polished sections, but again the data fail to suggest a clear influence of the additive on the coarsening: densification ratio.

Comparing the paths of surface area reduction shown in Figures 39 and 40 to the possible trajectories in Figure 25, it can be seen that both Al_2O_3 and MgO -doped Al_2O_3 undergo concurrent densification and coarsening. The changing slope of the curves indicate that the ratio of densification to coarsening becomes greater at higher densities.

While the two techniques are consistent in their results, as was shown in Figure 41, the values of S_V^P calculated from the measured values of S_m are ~40 to 70% higher than the actual measured values of S_V^P . Possible reasons for this include: 1. The BET technique is more sensitive to surface roughness than is quantitative microscopy, resulting in a higher measured specific surface area. 2. Stereological measurements are dependent on the magnification and resolution of the photographs; the surface area of very small pores or particles may not be included in the measurement. The magnification must, of course, be chosen to minimize this effect.

5.2 EFFECT OF MgO ON COARSENING IN Al_2O_3

Results are given in Figure 42 for the dependence of grain boundary area, S_V^{gb} , on sample density as measured by quantitative microscopy. Here it can be seen that the specific grain boundary surface density (m^{-1}) is considerably influenced by the additive, samples with magnesia having a higher grain boundary area at a given density value than undoped samples.

The expected trajectory of grain boundary change is shown in Figure 48. For a system in which pure densification is occurring, the trajectory begins at a point given by the initial compact density and zero grain boundary area. It then rises as surface area is replaced by grain boundary area and terminates at the value for the grain boundary area in the fully dense sample. The exact form of the trajectory is strongly dependent on coordination number^(62,113) as was the densification trajectory of the surface area vs. density plots discussed in Section 2.4.2.

For spheres in simple cubic packing, for example, which are considered to convert to cubes of equal volume (no coarsening), one unit of surface area is replaced by 1.18 units of grain boundary area (densification increasing the number of structural units per unit volume). With the initial surface area value estimated from Figure 40 at ~73% relative density as $\sim 3.5 \times 10^6 \text{ m}^{-1}$ (this corresponds to $0.5 \mu\text{m}$ radius spheres in simple cubic packing), the end point in the absence of coarsening would be a grain boundary area of $4.1 \times 10^6 \text{ m}^{-1}$ at the fully dense condition. (Conversion of the same spheres to tetrakaidecahedra would give 1.05 units of grain boundary area or a maximum $S_V^{gb} = 3.7 \times 10^6 \text{ m}^{-1}$.)

In the presence of a degree of coarsening, the boundary area once formed is reduced as a consequence of grain growth. The eventual trajectory is then given by the resolution of the two opposing tendencies, rapid grain growth giving a flatter curve than found for restricted grain growth.

Pure coarsening, with grain boundary area formed by the restructuring of the

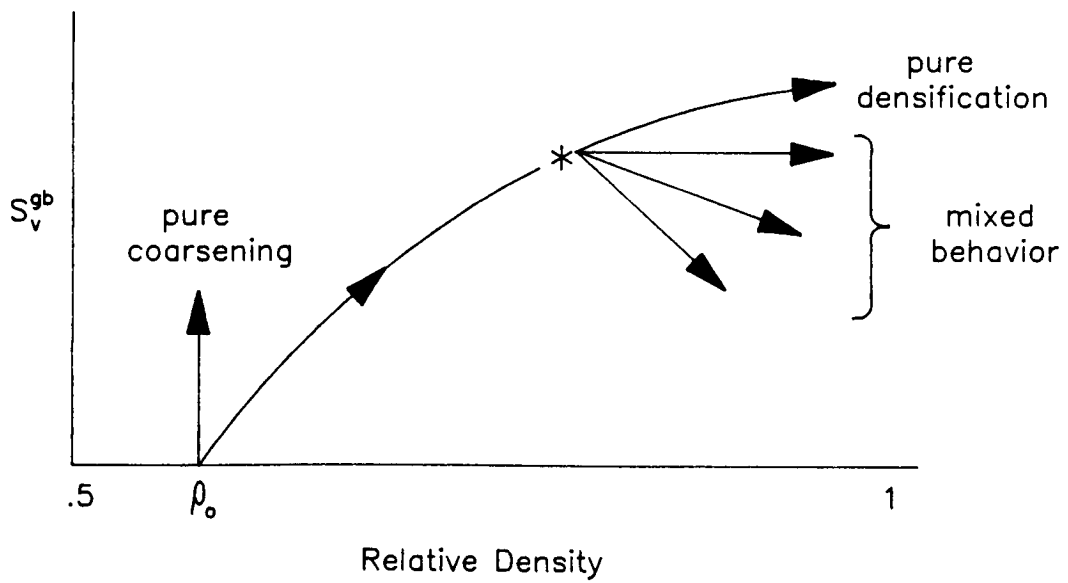


Figure 48. The trajectory of the amount of grain boundary area in a sintering compact is decided by the balance between the densification and the coarsening tendencies.

compact by surface diffusion or gas-phase transport, gives a vertical line on the S_V^{gb} vs. density plot rising (at constant density) to a value dependent on the coordination number, dihedral angle and the relative rates of neck growth and subsequent structural coarsening and then falling back as the neck growth stage ceases. On the approximate basis that the neck grows to $x/a \approx 0.5$, for simple cubic packing with a coordination number of 6, ~40% of the original particle surface area would become grain boundary, or, in the case above, S_V^{gb} could rise to $1.4 \times 10^6 \text{ m}^{-1}$ before falling back.

From Figure 42 it is clear that both doped and undoped materials undergo mixed behavior with contributions from both densification and coarsening. The doped system does, however, show greater resistance to grain growth; at a given density, it retains a higher grain boundary area than the undoped material.

To consider this further, it is helpful to distinguish between two categories of grain boundary (Figure 43), namely those that intersect pores (and which are consequently active in contributing to densification) and those which are entirely connected to other grain boundaries. By inspection of the possibilities, a closer identification of the action of the additive can be made in respect to the two types.

5.3 A MODEL FOR GRAIN BOUNDARY INTERACTIONS

A simple cylindrical model can be used for boundaries of the first type (A in Figure 43) to show the relation between the surface area and the grain boundary area (Figure 49). With the cylinder surface as the surface area and sections normal to the cylinder axis as the grain boundaries, S_V^p is given by $2r^{-1}$, where r is the radius of the unit-volume cylinder, and S_V^{gb} is given by h^{-1} , where h is the grain height.

Data from Figures 40 and 42 for a compact that is 80% dense give the

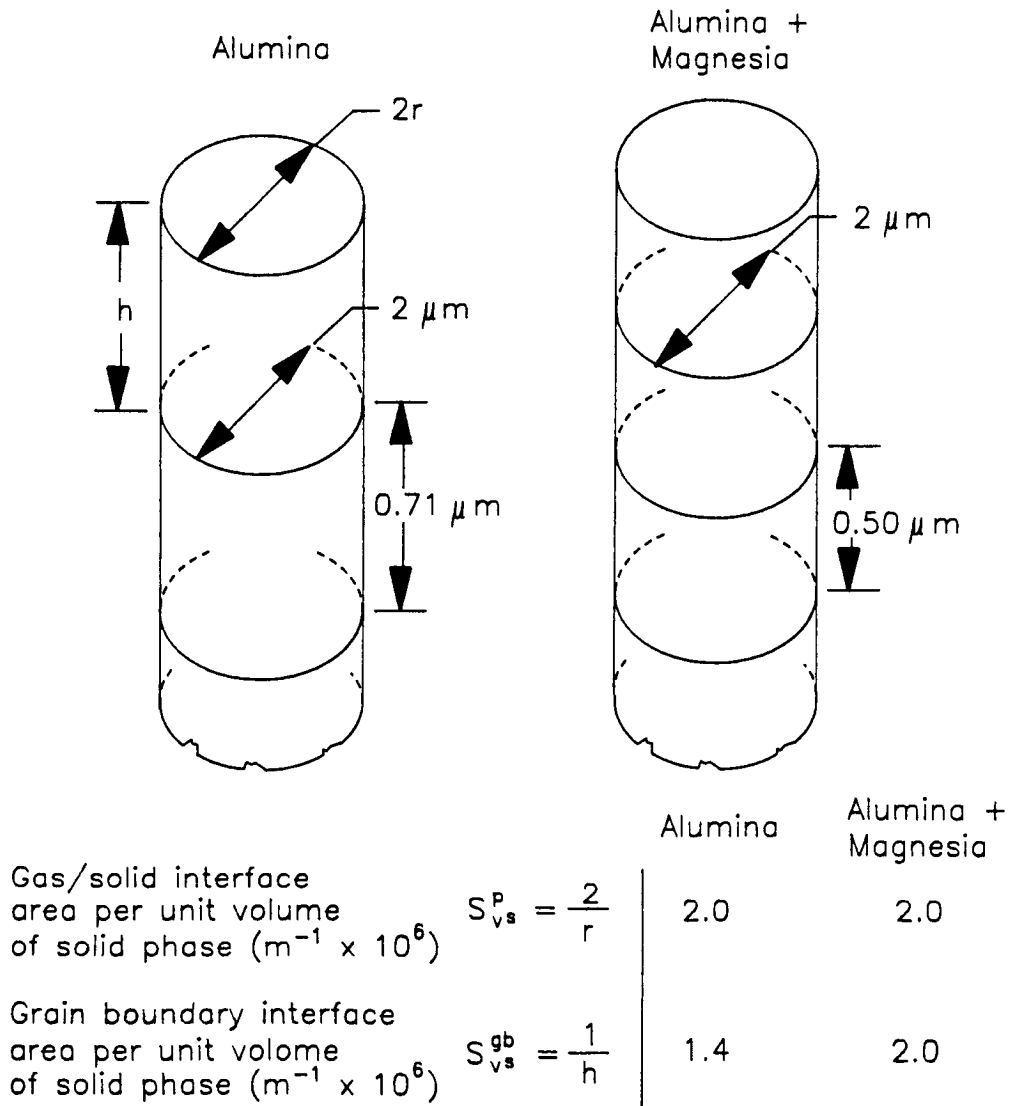


Figure 49. Model to show the relation between the surface area and the grain boundary area. The cylinder surface represents the pore/solid surface area and the sections normal to the cylinder axis represent the grain boundary area. Values for 80% dense alumina from Figures 40 and 42 are used.

dimensions shown in Figure 49. The radius of the cylinder is unaffected by the presence of the additives, i.e., S_V^P , and with it the form of the skeleton solid structure remain the same. The boundaries, however, would occur at greater frequency along the length of the cylinder in the doped material; for such boundaries the 40% increase in S_V^{gb} would represent a 40% greater frequency which should in turn result in a 40% greater densification strain rate at a given degree of skeleton development, i.e., given S_V^P . Since it is known from Figures 39 and 40 that this increase does not occur, the conclusion may be drawn that the additive does not primarily act by influencing the behavior of boundaries of this type, i.e., those intersected by porosity. Confirmation of this result can be made by direct observation of the samples in respect to the length of boundary/pore intersection to be discussed below.

5.3.1 Effect of the Two Types of Grain Boundaries on Microstructural Change

In a sintered structure, there are two types of interfaces, pore/solid and solid/solid (grain boundary), which interact with each other and affect the microstructural development during sintering. If the pore/solid interfaces and the grain boundaries intersect completely randomly, that is, if the pore has no influence on the position of the grain boundaries, the length of triple line formed can be calculated from previously measured values by the relationship⁽⁶⁸⁾

$$L_V^R = \frac{\pi S_V^P S_V^{gb}}{4 V_V^S} \quad (38)$$

If the pore/solid interfacial area and grain boundary interactions were strictly random, the triple line length would be greater for the doped material than for the undoped material due to the greater grain boundary surface of those samples as is shown in Figure 50.

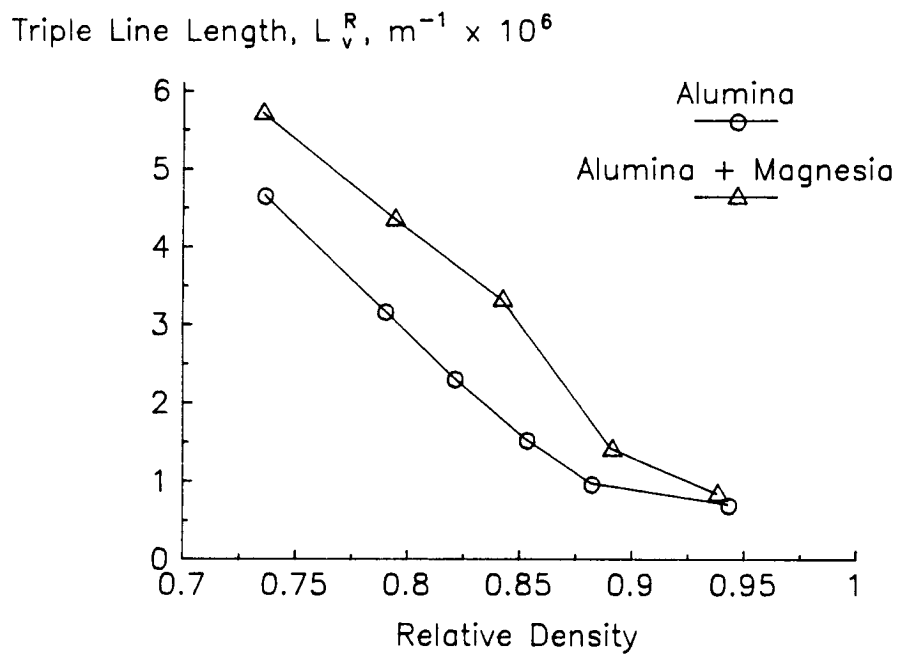


Figure 50. Calculated triple line length for completely random pore/solid interfacial area and grain boundary interaction.

In an actual sintered piece, however, interaction of the two interfaces is not random because grain boundaries can be pinned by pores. The actual length of L_V^{ssp} can be measured by applying Equation 34; it was seen in Figure 44 that, despite some scatter in the data, the extent of solid/solid/pore interface is unaffected by the additive.

Values of L_V^{ssp} (measured) are plotted against those of L_V^R (calculated) in Figure 51. If the pore surfaces and grain boundary surfaces were both placed randomly in the structure, L_V^{ssp} would be equal to L_V^R and the data would lie on the dotted line in Figure 51. The actual values of L_V^{ssp} are up to four times the calculated random values with the increased intersection due to pore pinning of grain boundaries. Whereas Figure 44 (L_V^{ssp} vs. density) shows that the absolute degree of grain boundary/pore interaction is the same for both materials, this figure shows that the interaction relative to the possible random interaction is greater for the undoped material – an expected conclusion due to the smaller amount of grain boundary area for that material.

Figure 50 predicts that the highest value of L_V^{ssp} will be at the lowest density due to the large amount of pore/solid surface area. The measured L_V^{ssp} (Figure 44), however, rises to a peak value at ~78% density and then decreases with densification. This is to be expected since during the early stages of neck growth, the length of grain boundary/pore intersection is very small. The length increases with increasing neck size and then decreases with pore removal and grain growth as densification proceeds.

The existence of the second type of boundary in a porous compact, i.e., that linked directly to other boundaries in a pore-free region of the structure (type B in Figure 43), is most likely to occur as a consequence of inhomogeneous packing in the powder compact. If the original powder packing density shows some local fluctuations, e.g., if some degree of agglomeration is present, then pore-free regions can develop within the structure even when the total bulk density remains

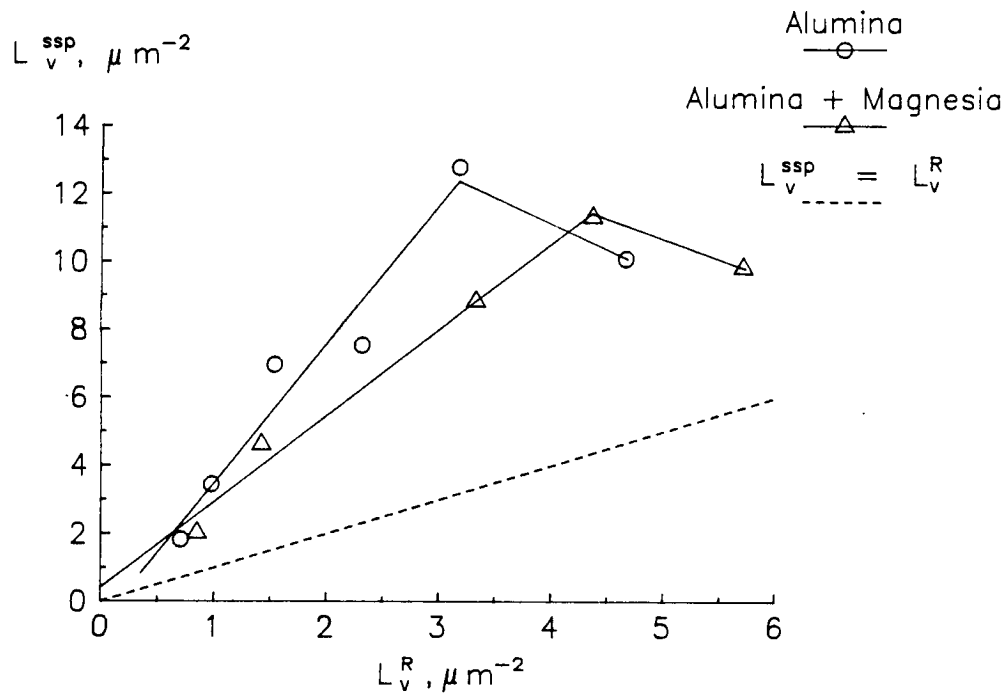


Figure 51. Comparison of calculated (for random interactions) and measured triple line lengths of grain boundary/pore intersections.

small.⁽⁴³⁾ The results of the present work (excess grain boundary area in the doped samples (Figure 42), but the same amount of grain boundary area intersecting pores [Figure 44]) indicate that in the presence of the additive, the ease of boundary movement within such dense regions and, hence the rate of local grain growth, is reduced. Confirmation of this effect can be obtained by measuring the extent of grain boundary/grain boundary intersection in the samples; it is seen in Figure 45 that the MgO-doped samples show a greater extent of grain boundary/grain boundary interaction. The limitation of grain growth within densified regions of the sample has no effect on the instantaneous densification rate (Figures 39 and 40) but gives a higher boundary value at a given value of the density (Figure 42). Evidence^(35,77) for the ability of MgO to slow grain boundary movement in fully dense alumina is consistent with this picture, the mechanism most probably being that of solid solution segregation and drag.⁽³⁶⁾

5.3.2 Relationship Between Grain Size and Pore Size

The relationship between grain mean linear intercept and pore mean linear intercept is given in Figure 52. Assuming a spherical shape, the grain or pore size equals 1.5 times the mean linear intercept.⁽¹⁰⁷⁾ The pore size increases linearly with grain size for both materials to a maximum at ~80% density for the MgO-doped Al_2O_3 and at ~90% for the undoped material; the pore size then decreases due to densification concurrent with continued grain growth. While the maximum pore size is the same for both materials, at a given pore size, the undoped Al_2O_3 has a larger grain size. The pore size/grain size relationship is another indication that the MgO is controlling the Al_2O_3 grain size in dense regions, but not affecting the pore/solid surface structure.

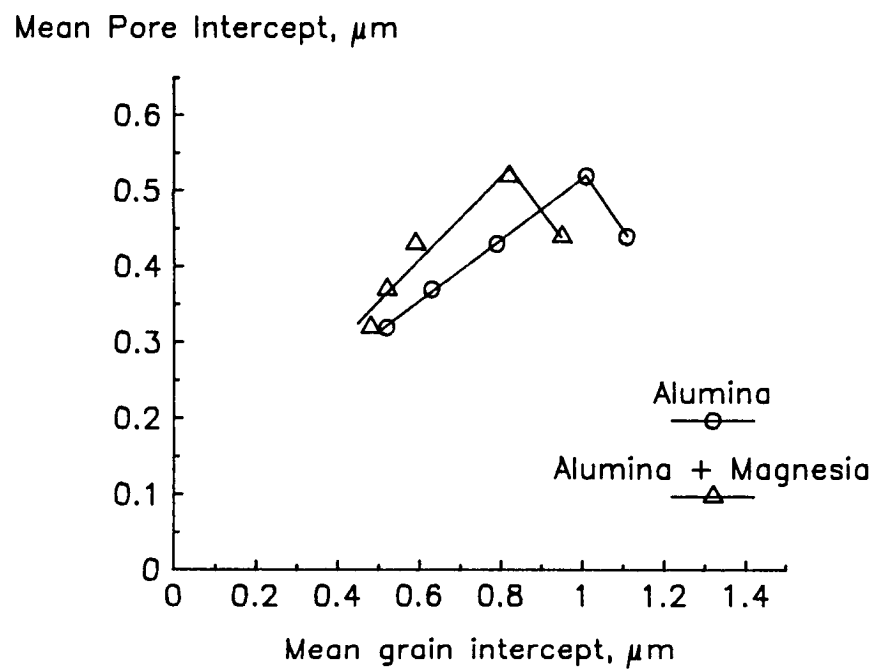


Figure 52. Relationship between mean pore intercept and mean grain intercept.

5.4 CONCLUSIONS REGARDING THE EFFECTS OF MgO ON THE SINTERING OF Al_2O_3

The significance of this result from the point of view of the overall progress of sintering can be seen from two points of view. First, following arguments⁽¹¹⁴⁾ that growth in relatively dense regions of homogeneous microstructures can lead to the onset of abnormal grain growth, any impediment to this process such as that caused by solid solution drag will be helpful in stabilizing the microstructure. Second, following arguments⁽¹¹⁵⁾ concerning the release of stress developed as a consequence of differential shrinkage rates in inhomogeneous systems, the retention of fine grain size in the densified regions and hence of a reduced resistance to local strain is beneficial from the point of view of removing inhomogeneity without crack formation. Both of these processes would be assisted by the ability of the additive to restrain boundaries as evidenced in this work.

A final point concerns the light thrown on the function of the MgO sinter additive on Al_2O_3 by these results. Generally additives acting in the solid state have been considered to be capable of two possible major contributions: the first can be termed ratio control and represents the ability of an additive to modify the ratio of densification rate: grain growth rate in a favorable direction⁽⁴⁹⁾ say by influencing diffusion coefficients for the atomic mechanisms involved; the second can be termed microstructure stabilization and represents the ability of the additive to restrain such processes as abnormal grain growth, say by segregation and pinning of otherwise mobile boundaries.

The indications from the present work are that ratio control is relatively unimportant for the MgO/ Al_2O_3 couple. This finding, which has been obtained by direct measure of the influence of the additive on the ratio, is consistent with results obtained⁽⁵¹⁾ on the same system using the entirely different method for directly determining the ratio which is based on the analysis of densification

kinetics during hot-pressing. The consistency of these separate results together with the clear indication of the ability of MgO to act ^(35,77) as a pinning agent in the Al₂O₃ system suggests significant operation of this additive through the second of the two major roles. It lends support to the growing recognition of the importance of the control of inhomogeneity ⁽¹¹⁵⁾ as a major factor in successful sintering.

CHAPTER 6

RESULTS AND DISCUSSION: YTTRIA

6.1 ANNEALED POWDERS

The early stages of sintering in loose Y_2O_3 powder have been examined using two different techniques, BET surface area analysis and direct observation of the particles using transmission electron microscopy. The relationship of the surface area measurement by BET and the annealing temperature is shown in Figure 53. From the graph it can be seen that the initial surface area of $\sim 7 \text{ m}^2\text{g}^{-1}$ decreases slightly even after annealing at 900°C for 1 h, with the MgO doped material having a slightly higher surface area, possibly due to some fine particulate MgO remaining on the surface from the decomposition of the $Mg(NO_3)_2$.

Annealing at higher temperatures ($900^\circ - 1100^\circ\text{C}$) causes a drastic decrease in the surface area of both the doped and the undoped powders; above 1100°C there is a further decrease in the surface area with increased temperature, but at a much lower rate. The values measured for both the doped and the undoped powders are practically identical over the entire temperature range.

In contrast, the transmission electron micrographs (Figures 54, 55, and 56) indicate a dramatic difference between the doped and the undoped powders. The particle size of the undoped Y_2O_3 grows from an initial size $\sim 0.05 \mu\text{m}$ to $\sim 0.1 \mu\text{m}$ at 1100°C and finally to $\sim 1.0 \mu\text{m}$ at 1600°C , in the process producing clean defect-free grains within aggregates without porosity at the grain boundaries. On the other hand, the MgO-doped sample behaved differently; the particle size after increasing to $\sim 0.1 \mu\text{m}$ at 1100°C , did not grow any further, even when

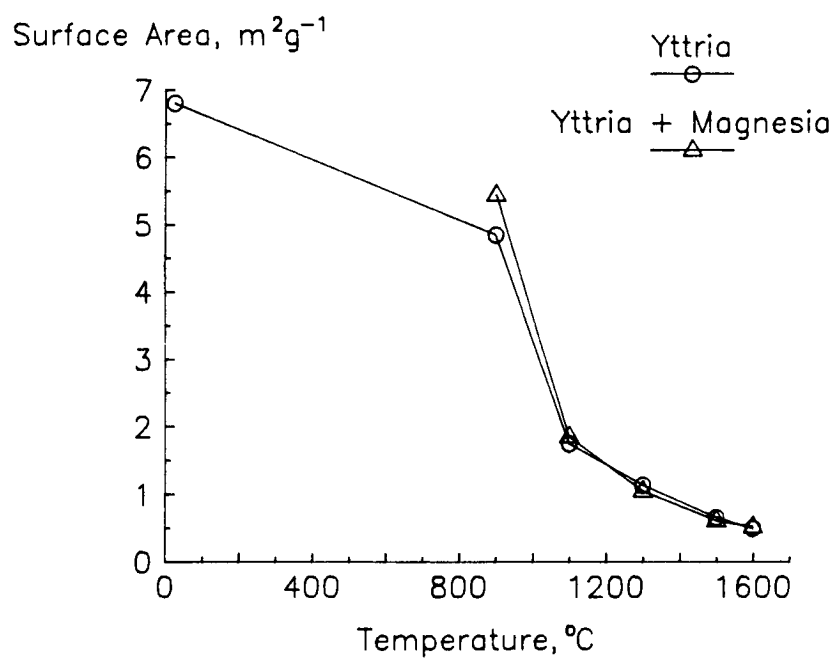


Figure 53. BET surface area vs. annealing temperature for yttria and yttria/magnesia loose powder annealed for 1 hour.

ORIGINAL PAGE IS
OF POOR QUALITY

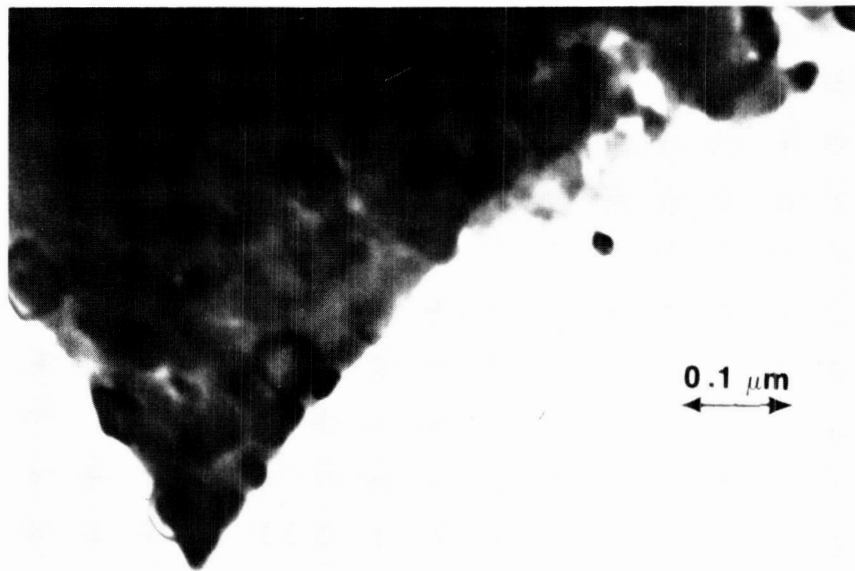
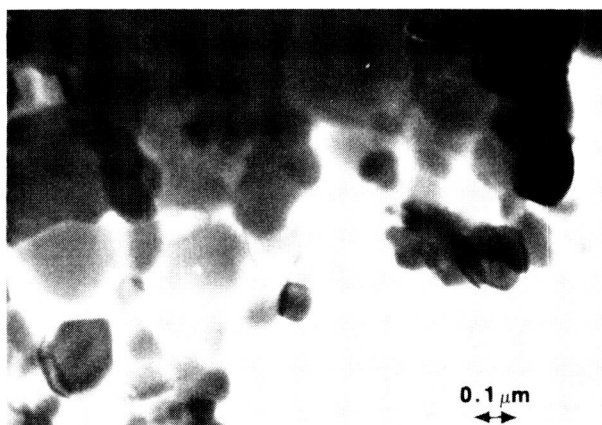
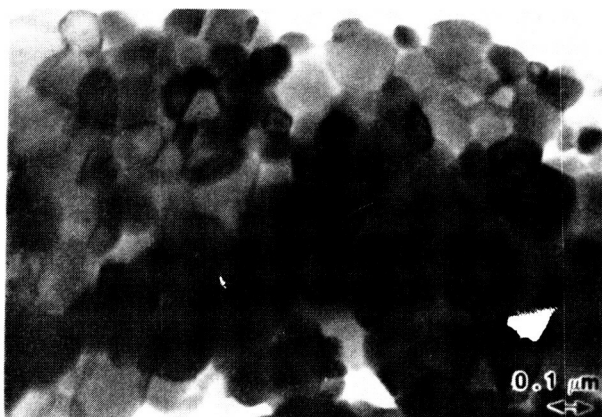


Figure 54. Transmission electron micrograph of unannealed yttria powder.

ORIGINAL PAGE IS
OF POOR QUALITY



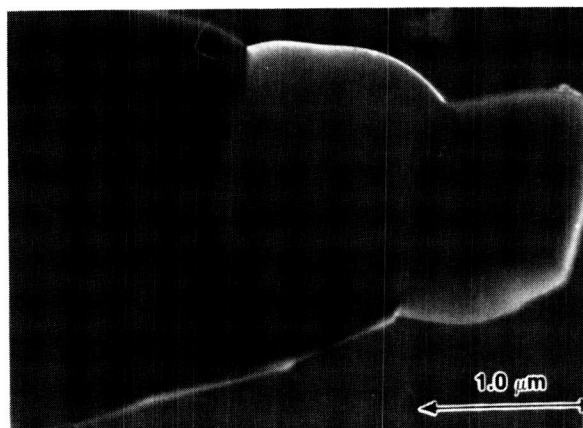
A



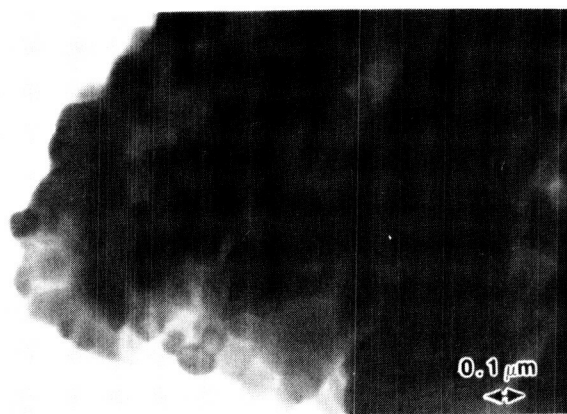
B

Figure 55. (A) yttria and (B) yttria + magnesia powders annealed for 1 hour at 1100°C.

ORIGINAL PAGE IS
OF POOR QUALITY



A



B

Figure 56. (A) yttria and (B) yttria + magnesia powders annealed for 1 hour at 1600°C.

heated to 1600°C. The particles were again made up of defect-free grains with no grain boundary porosity.

The TEM observations together with the BET surface area measurements indicate that the MgO dopant acts by inhibiting grain boundary movement within the aggregate of the Y_2O_3 . The development of the surface morphology of the powder agglomerates remains unaffected by the MgO as evidenced by the BET surface area measurements. It appears that grain boundaries are developed between individual particles in the aggregates; as these localized regions densify, the MgO addition prevents the movement of the grain boundaries, most probably by solid solution pinning.⁽³⁶⁾ Examination of the grain boundaries has not revealed any precipitation, hence it can be concluded that segregation of the MgO as a solute at the grain boundary is the significant effect. The efficacy of MgO as a sintering aid for Y_2O_3 ⁽⁹¹⁾ may in part be explained by retention of a fine grain structure and the consequent avoidance of abnormal grain growth.⁽¹¹⁶⁾

6.2 SINTERED COMPACTS

6.2.1 Sintered Densities

Isostatically pressed samples of Y_2O_3 , undoped and MgO-doped, were sintered for investigation of the coarsening behavior during sintering. Doped samples contained 0.2 mole % MgO, an amount expected to be within the solid solubility limit at the sintering temperature (1850°C) (Figure 28). Samples with green densities of ~55% were sintered in air for times of 2.5 to 120 minutes to develop a range of densities. The sintered densities are shown in Figure 57. While the densities of both the doped and undoped compacts increased rapidly at first, the MgO-doped samples reached a higher density in even the shortest measured time

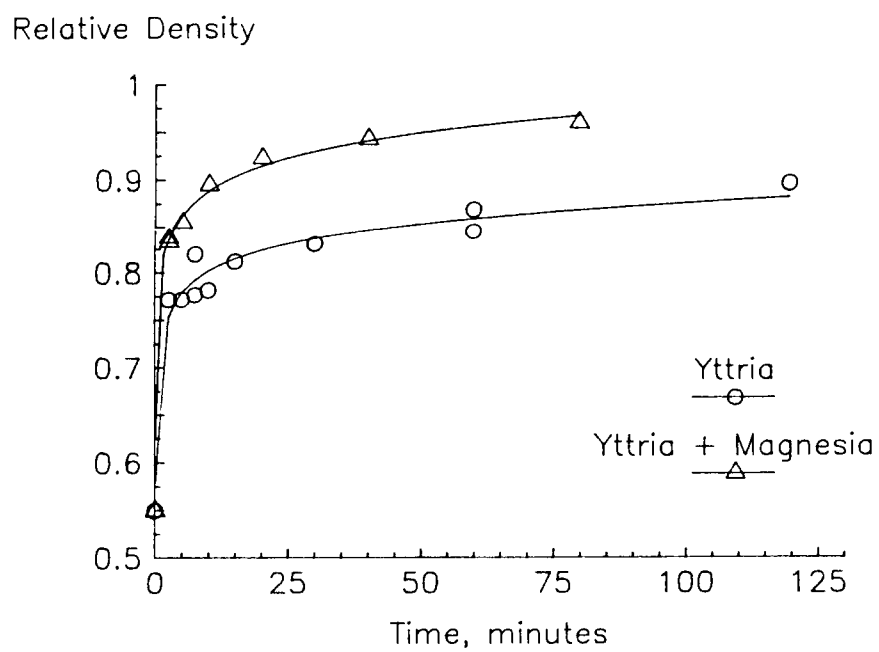


Figure 57. Sintered density of yttria and magnesia-doped yttria. All samples were sintered in air at 1850°C.

than did the undoped samples and remained at a higher density for all sintering times, indicating an increase in the densification rate of yttria in the presence of MgO. This does not provide sufficient information to determine the mechanism by which this increased rate is accomplished.

6.2.2 Surface Area vs. Density Diagram by BET

Since the samples densified so quickly, there were only a few samples with open porosity so that the pore/solid surface area could be measured by BET gas adsorption. (Preliminary experiments suggested that sintering at 1850°C would provide a wider range of densities than was actually obtained, however, the range was thought to be sufficient for this analysis.) The surface areas (Figure 58) of both the doped and undoped samples decreased to very low values and appear to all lie on the same curve, suggesting that addition of MgO does not change the densification:coarsening rate ratio of Y_2O_3 during sintering. The evidence is less clear than for the case of the MgO-doped Al_2O_3 , but again this behavior implies that, if MgO does increase the densification rate, then it must also similarly increase the coarsening rate; additional information on the coarsening behavior is needed to confirm this. This result is comparable to that for the loose powder in that MgO does not appear to affect the measured pore/solid interfacial area.

6.2.3 Etching

Polished samples were thermally etched to delineate grain boundaries for measurements needed for the stereological evaluation. The results were not uniformly good and efforts to repolish and re-etch or to prepare new samples generally created more problems. The lower density samples (e.g. Figure 59) etched well, but many appeared to have some kind of surface contamination; this

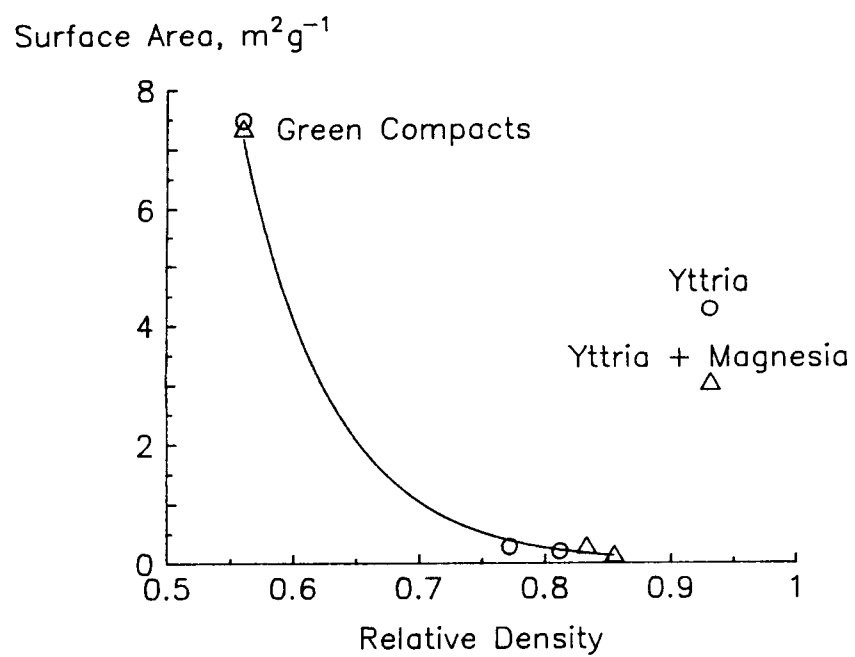


Figure 58. Specific surface area measured by gas adsorption of green compacts and compacts sintered in air at 1850°C.

ORIGINAL PAGE IS
OF POOR QUALITY

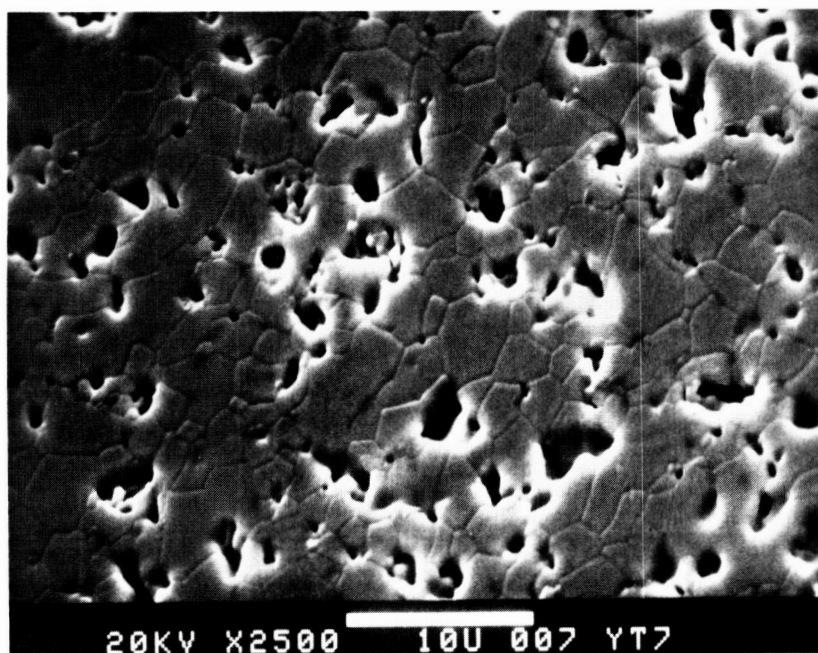


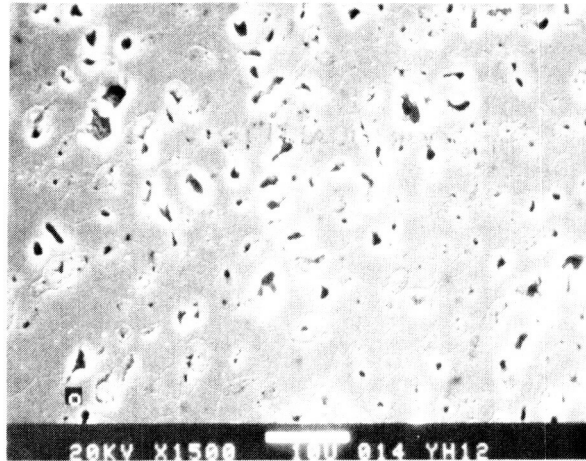
Figure 59. Yttria samples with densities $< \sim 90\%$ etched well by heating in air for 15 minutes at 1450°C .

did not affect the measurements. The densest samples appeared to have "bubbles" around many of the pores (Figure 60A and B). Energy dispersive x-ray analysis of these "bubbles" indicated the presence of Al, at first thought to be x-ray scatter from the aluminum mounting stub, but later suggested to possibly be contamination from the Al_2O_3 tubes in which the samples were sintered or etched.⁽¹¹⁷⁾ A non-wetting solid second phase, $\text{Y}_2\text{Al}_4\text{O}_9$, can form at temperatures below 1940°C .⁽¹¹⁷⁾ (The sintering temperature was 1850°C and the etching temperature was 1450°C .) The "bubbles" appearance in only the densest samples could be due to the need for an exposure time to Al_2O_3 long enough for a visible amount of the reactant to form. Attempts were made, unsuccessfully, to chemically etch these samples. The results of an attempt to etch another piece of the compact shown in Figure 60 with boiling HCl is illustrated in Figure 61. Polishing scratches are well delineated, but the grain boundaries are very difficult to see. There is no sign of the "bubbles" around the pores or of any grain boundary phase. Thus, whether the "bubbles" are a thermal etching artifact or a sintering product that is dissolved by the acid is unknown.

Due to a furnace malfunction, further attempts to thermally etch samples were made in a furnace that had probable metallic contamination. Even covered Y_2O_3 samples were badly contaminated. Yttria apparently reacts quite easily with many different species.

6.2.4 Surface Area vs. Density Diagram by Stereology

Due to the poor quality of many of the polished and etched sections, there is considerable scatter in the measured values of the pore/solid surface area. Figure 62 shows the measured values of the specific surface area and an indication of the reliability of those numbers, suggesting no difference between the doped and the undoped material at a given density.



A



B

Figure 60. Yttria samples (both with and without magnesia) with densities $\geq \sim 90\%$ appeared to have "bubbles" around many of the pores after thermal etching. The presence of Al was detected by EDX. (Yttria, density = 89.6%)

ORIGINAL PAGE IS
OF POOR QUALITY

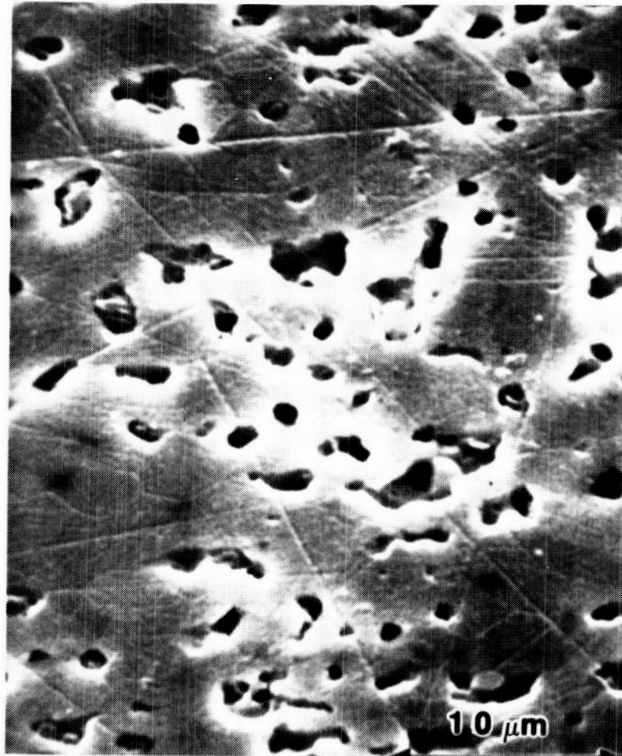


Figure 61. Attempts to chemically etch yttria (boiling 20% HCl) resulted in well etched polishing scratches, but little etching of the grain boundaries.

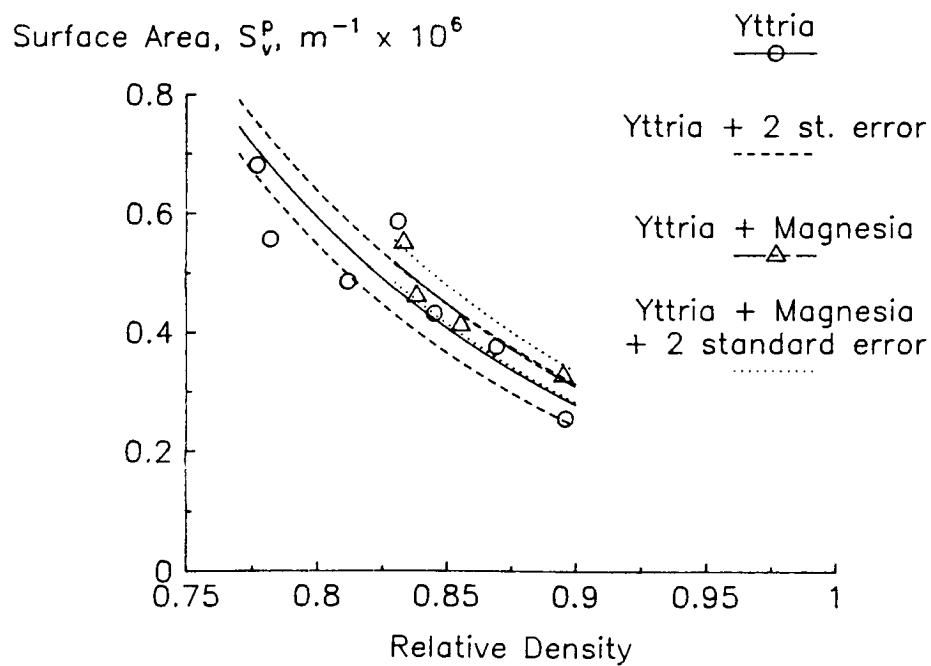


Figure 62. Specific surface area measured by quantitative microscopy shows considerable scatter due to the poor quality of the etched samples.

doped and the undoped material at a given density.

6.2.5 Grain Boundary Area vs. Density Diagram

It appears from Figure 63 that the extent of grain boundary area is unchanged by the addition of MgO to the Y_2O_3 , in both cases decreasing as the density increases over the density range evaluated (~82 - 90%). This result is inconsistent with the results of the TEM observations of the annealed Y_2O_3 powders (Figures 54 - 56) which indicate that MgO pins the Y_2O_3 grain boundaries, resulting in a much finer grain size, i.e., much more grain boundary area. It is also surprising that the amount of grain boundary area would already be decreasing (Figure 63) at densities below ~90%.

The SEM photographs of the sintered Y_2O_3 samples (Figure 60) clearly reveal contamination problems during sintering and/or etching. It appears that the results being measured are a consequence of the presence of contaminants and that these effects are much greater than any influence of the MgO. This conclusion applies also, of course, to the pore/solid surface area analysis.

6.2.6 Triple Lines

Not enough sections could be polished and etched to a sufficient quality to allow the evaluation of triple line lengths.

6.3 CONCLUSIONS REGARDING THE EFFECTS OF MgO ON THE SINTERING OF Y_2O_3

This portion of the study was included to evaluate the usefulness of the pro-

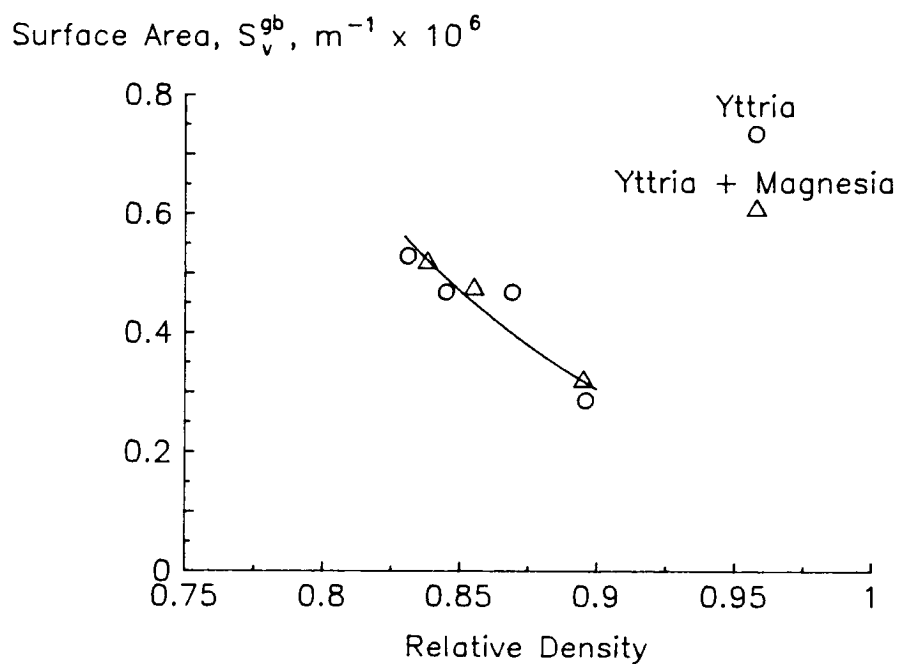


Figure 63. Specific Grain boundary area appears to be the same for both the undoped and the MgO-doped yttria. This is due to large effects of contaminants masking the effect of magnesia.

posed techniques in giving a better understanding of a relatively unknown system. It was known that MgO acts as an effective liquid phase sintering aid for Y_2O_3 above $1900^{\circ}C$,⁽⁹¹⁾ but would be expected to act by a solid solution mechanism at the selected sintering temperature ($1850^{\circ}C$).

It is clear from the TEM analysis of annealed Y_2O_3 powders that magnesia added as a dopant to Y_2O_3 powder has the effect of restricting grain boundary movement within readily densified regions (aggregates) of the powder, while not having any effect on the gas/solid interfacial area of the powder during heat treatment. This suggests that the limitation of such grain boundary movement can be an important objective in the control of sintering allowing densification to proceed uninhibited by either excessive normal grain growth or abnormal grain growth. Based on analysis of annealed loose powders, MgO appears to have the same effect on the sintering behavior of both Al_2O_3 and Y_2O_3 : inhibiting grain boundary movement within fully dense regions of the compact while not affecting the development of the gas/solid surface morphology.

Supporting these conclusions with further observations of sintered samples highlighted some of the difficulties that may be encountered in obtaining the data needed for the surface area/density analysis. The yttria apparently reacted with Al_2O_3 at some stage in the processing, either during sintering or thermal etching. The presence of the reactants completely masked any effects of the MgO dopant so that no conclusions regarding the effect of MgO on the sintering of Y_2O_3 could be made from these samples. Another difficulty was the limited range of densities obtained during sintering; a wider range would have been preferable for an adequate analysis of the additive effects.

CHAPTER 7

RESULTS AND DISCUSSION: SILICON CARBIDE

7.1 SINTERING

Bars of α -SiC, with and without boron and carbon sintering additives, were sintered for investigation of the coarsening behavior during sintering. Bars were sintered in flowing argon at 2050°C for hold times at temperature of 0 - 240 minutes; the resultant densities are plotted in Figure 64. (In all of the density vs. time plots, the green compacts are plotted at 0 minutes and the samples with no hold time at the sintering temperature are plotted at 1 minute.) As anticipated, the SiC without the carbon and boron additives did not densify; the density actually decreased slightly due to loss by decomposition and/or vapor transport. The SiC with added boron and carbon began to densify during heat-up, increasing from 67% to 80% dense by the time the sintering temperature was reached. After 30 minutes of sintering time, the density was still 80%. Densification continued with additional time, finally reaching 95.3% of theoretical.

The step in the densification curve is unusual and the cause is unknown. It may be a result of inhomogeneous mixing of the sintering aids or of an incorrect sintering cycle, although that did not appear to be the case. Additional samples would need to be sintered in the time range 0 - 60 minutes to clarify the densification behavior. The step will be treated as genuine in this analysis because the data for that sample is consistent throughout.

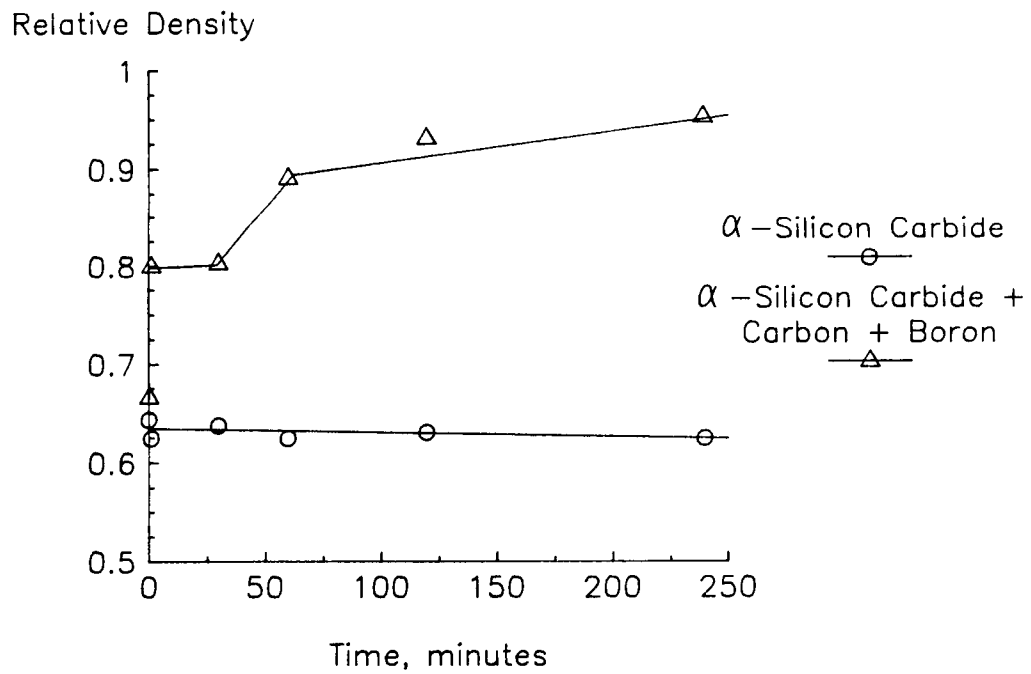


Figure 64. Sintered density as a function of hold time at 2050°C. Heat-up time was ~40 minutes.

7.2 SURFACE AREA vs. DENSITY DIAGRAMS

7.2.1 Surface Area Measured by BET

The surface area v. density plot is given in Figure 65. This is almost an ideal example of the diagram suggested by Burke *et al.*⁽⁵⁵⁾ and clearly shows the distinction between a material that densifies during sintering and one that only coarsens. The path of surface area reduction for the undoped SiC is very close to the vertical pure coarsening trajectory of Figure 25. The SiC containing carbon and boron has, overall, a highly curved trajectory indicative of concurrent densification and coarsening. However, this trajectory, unlike the ideal case, has a break in it at 80% density (also seen in the densification plot above) where the structure appears to be coarsening without additional densification. Comparing the unetched polished sections in Figure 66, the 0 minute hold time sample (A) has a "particle size" on the order of 5 μm , whereas the 30 minute sample (B) has a "particle size" on the order of 10 μm . Additional confirmation of this coarsening behavior comes from the mean pore intercept measurements (Figure 67). The "pore size" of the 30 minute sample is larger than that of the 0 minute sample. The "pore size" then decreases again as further densification occurs.

Since the density of the undoped SiC samples changes little during sintering, additional information on the material's behavior may be obtained by considering the relationship between surface area and sintering time (Figure 68). It can be seen the the greatest surface area reduction for both materials occurs during the heat-up to the sintering temperature — a period of ~40 minutes. After undergoing the large surface area reduction during heat-up, the surface area of the undoped material, interestingly, remains nearly constant with additional sintering time. Particle coarsening (and thus reduced surface area) would be expected to continue with increased sintering time. While the original SiC (Figure 31) had a wide

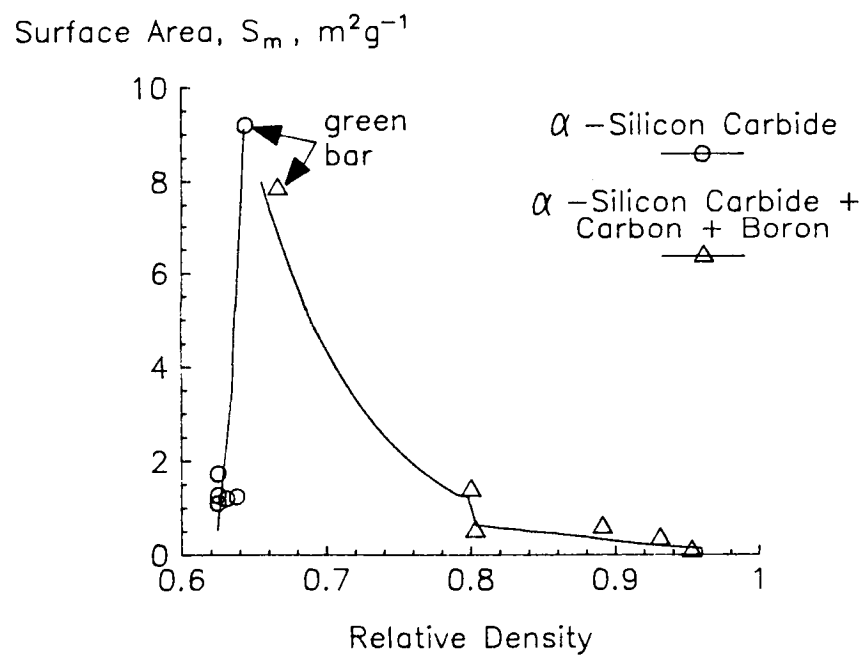
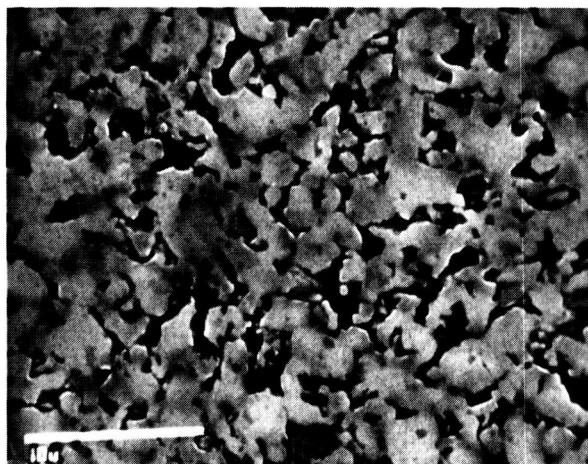
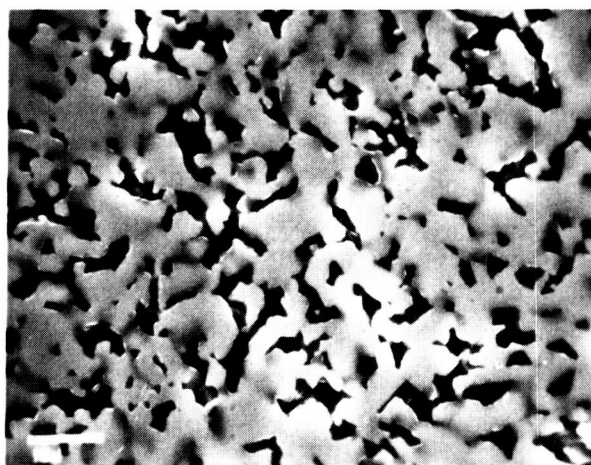


Figure 65. The distinction between materials that only coarsen and those that have concurrent densification and coarsening is clearly demonstrated by the surface area vs. density plots of SiC.



A



B

Figure 66. SEM micrographs of SiC with carbon and boron sintered to 80% density. (A) 0 minutes time at temperature has "particle size" $\sim 5 \mu\text{m}$ (B) 30 minutes at temperature has "particle size" $\sim 10 \mu\text{m}$.

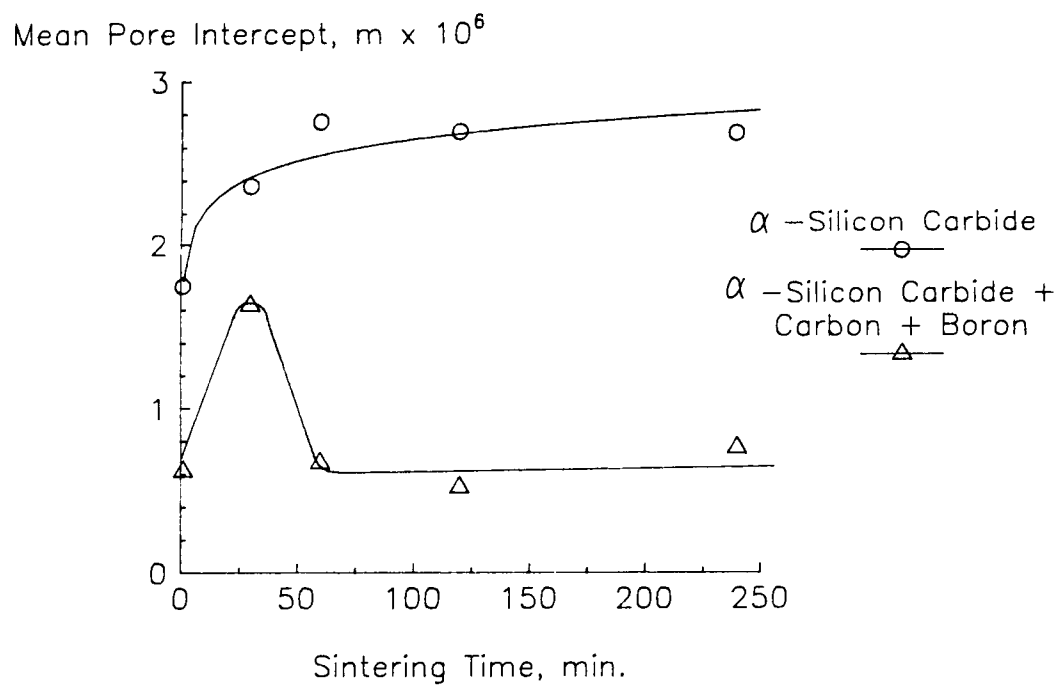


Figure 67. The mean pore intercept length is largest for the sample of SiC with B and C.

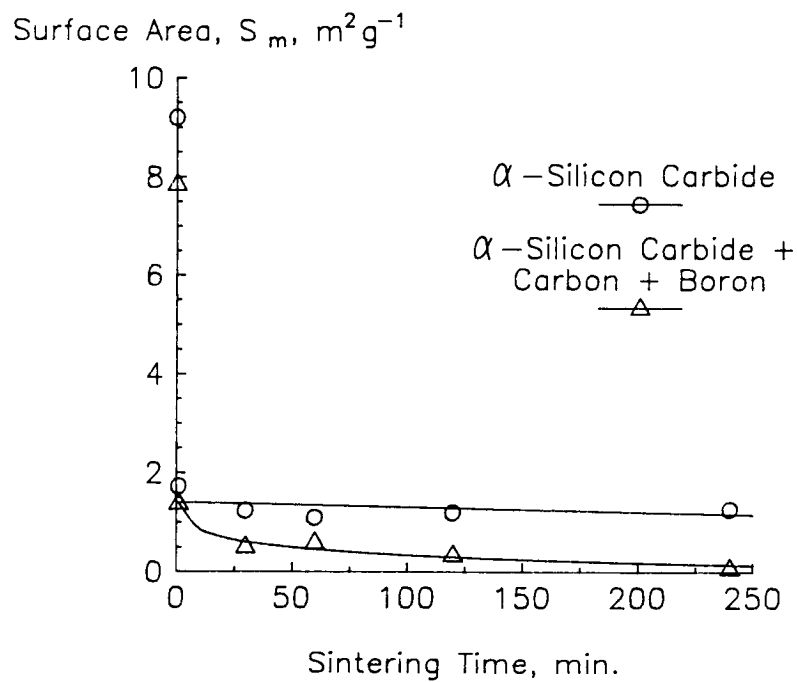


Figure 68. Both materials undergo a large reduction in surface area during heating to the sintering temperature. The surface area of the undoped SiC remains nearly constant. The surface area of the SiC with sintering aids continues to fall gradually.

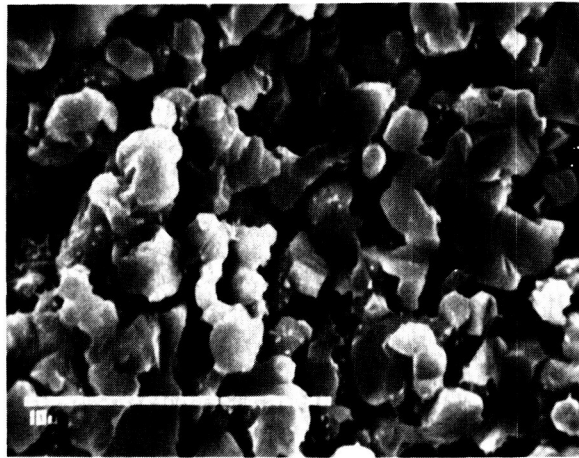
particle size distribution and included many grains that were flake-like, the particles of a sample with no hold time at the sintering temperature can be seen in Figure 69A to be nearly equiaxed and have a fairly narrow size distribution. This is the behavior predicted for grain growth in porous compacts by the Greskovich and Lay model⁽⁴³⁾ (see Section 2.3.2.2) Some of the grains appear to be faceted and others have more rounded surfaces. These may be low energy configurations that act to retard further coarsening. A similar sample, after being sintered for 240 minutes, (Figure 69B) appears to be nearly identical in grain size and shape. In contrast, after the initial reduction, the surface area of the carbon and boron doped SiC decreases from 1.4 to 0.5 m²g⁻¹ and then continues to decline at a slower, fairly constant rate with additional sintering time. Note that the samples at 0 and 30 minutes whose behavior appeared to be unusual in the previous two graphs (Figures 64 and 65), exhibits normal behavior in this representation.

7.2.2 Surface Area Measurement by Stereology

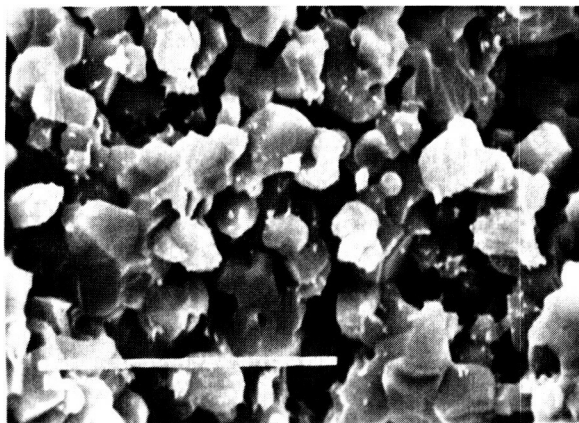
Surface areas were measured on SEM photomicrographs of polished sections of the samples.

7.2.2.1 Pore/Solid Surface Area

As discussed previously for the Al₂O₃ samples, it is very difficult to accurately measure the pore/solid surface area of low density samples. Because of the great depth of focus of the SEM, it is often hard to differentiate particles in the plane of polish from those within pores. Despite these difficulties, the results seen in Figure 70 compare well with the BET measurements in Figure 65. The higher density samples of SiC with sintering aids are easier to measure and the trajectory of surface area reduction obtained (Figure 70) is comparable to the S_m trajectory of Figure 65.



A



B

Figure 69. The morphology of the SiC grains does not appear to change as the sintering time increases from (A) 0 to (B) 240 minutes.

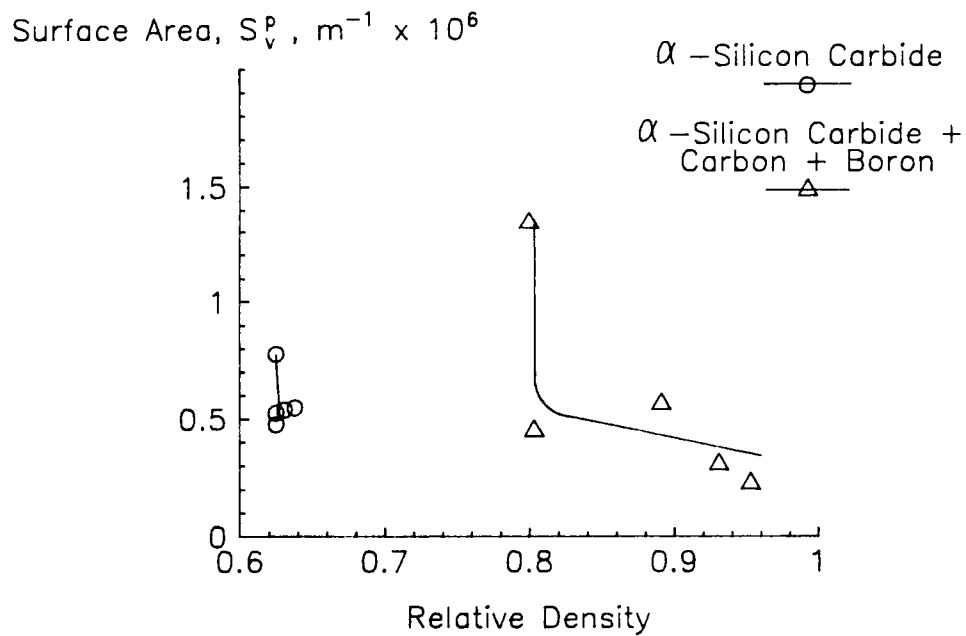


Figure 70. The surface area reduction measured by quantitative microscopy again shows the nearly pure coarsening behavior of the undoped SiC and the mixed coarsening and densification behavior of the SiC + C + B.

7.2.2.2 Comparison of Surface Area vs. Density Diagrams

The values of the surface area obtained by the two techniques are compared in Figure 71. The comparison is similar to that for Al_2O_3 with the values of S_V^p calculated from S_m being higher than the measured values — in this case, as much as nearly 400%. The values are again much closer at higher densities where the stereological measurements are more accurate. As can be seen in Figure 72, the doped sample with 0 minutes hold time at the sintering temperature still contains many extremely small particles that will contribute to the BET surface area, but probably not be measured by quantitative microscopy.

7.2.2.3 Grain Boundary Area vs. Density Diagram

Evaluation of the grain boundary area requires microstructures with well-defined grain boundaries. As discussed in Section 3.8.2, the more porous SiC samples could not be etched satisfactorily. Figure 73 is an example of the results for the undoped SiC. Many grain boundaries can be seen, but the lack of consistent etching combined with the uncertainty as to which grains are in the plane of polish, makes obtaining accurate grain boundary area values impossible. The samples seemed to etch better after longer sintering time and an estimate (still only approximate) of the grain boundary could be made of the 240 minute sample.

The SiC containing sintering aids, in most cases, etched well. Again the difference between the 0 and 30 minutes samples appeared. The 0 minute sample did not etch well enough for accurate measurement with polishing scratches etching as well as or better than grain boundaries (Figure 74A). The 30 minute sample (Figure 74B) etched clearly enough that the grain boundary area could be measured. Denser samples etched well and accurate values were obtained without difficulty.

The grain boundary area vs. density plot is shown in Figure 75. Unfortunately,

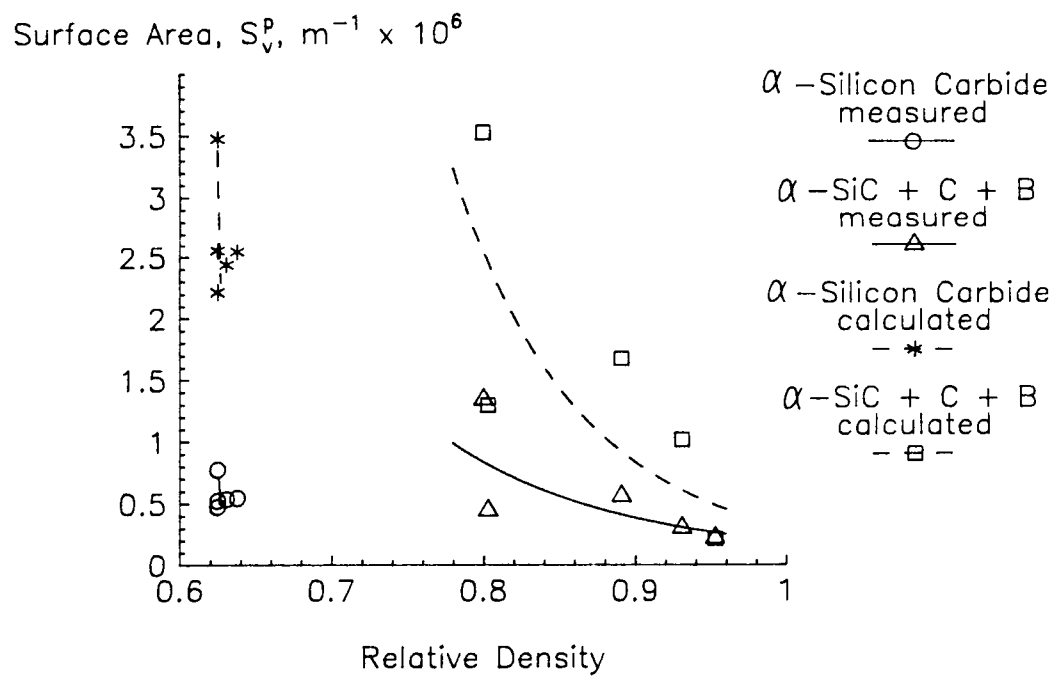


Figure 71. S_v^p measured compared to that calculated by $S_m = S_v \rho$

ORIGINAL PAGE IS
OF POOR QUALITY

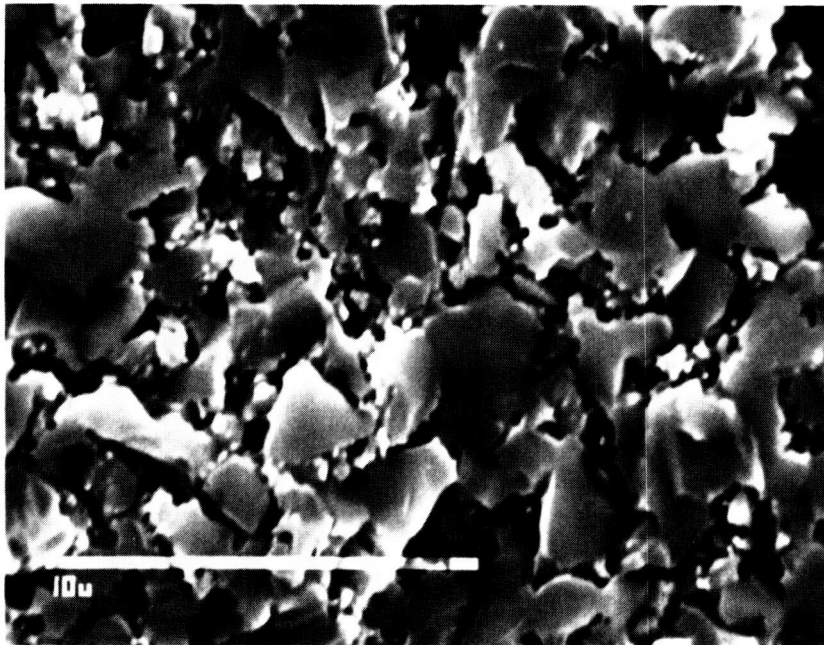


Figure 72. The very small particles will contribute to the surface area measured by gas adsorption, but may not be included in the value obtained by quantitative microscopy.

ORIGINAL PAGE IS
OF POOR QUALITY

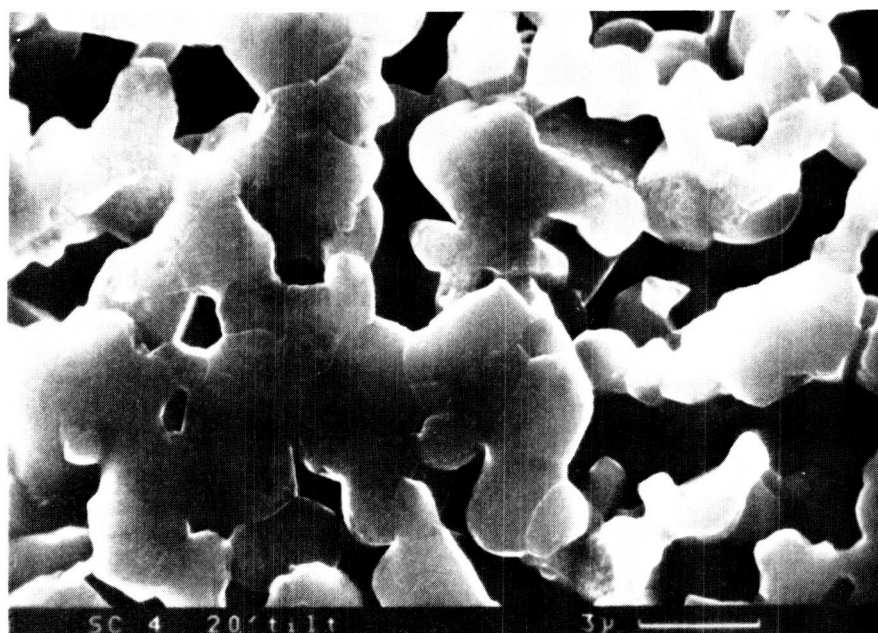
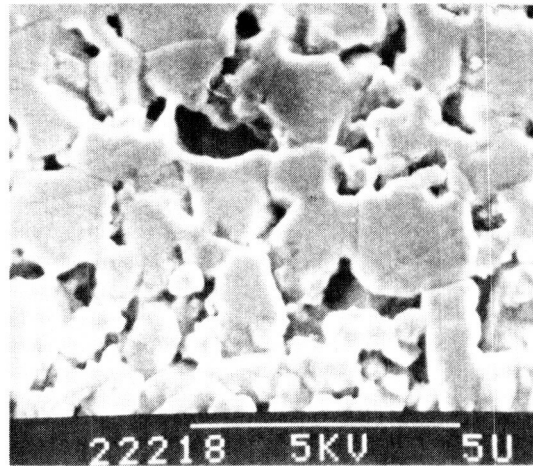
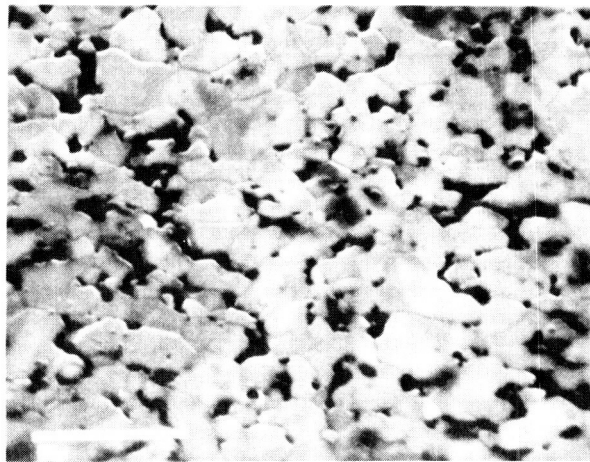


Figure 73. SEM micrograph of polished section of undoped sintered SiC. After etching many grain boundaries can be seen, but the uncertainty as to which are on the plane of polish and the presence of etched polishing scratches and surface roughness, make the accuracy of the grain boundary area evaluation doubtful.



A



B

Figure 74. SEM micrographs showing the difference in etching behavior of SiC containing sintering aids sintered for (A) 0 minutes and (B) 30 minutes at 2050 °C. Both samples are 80% dense.

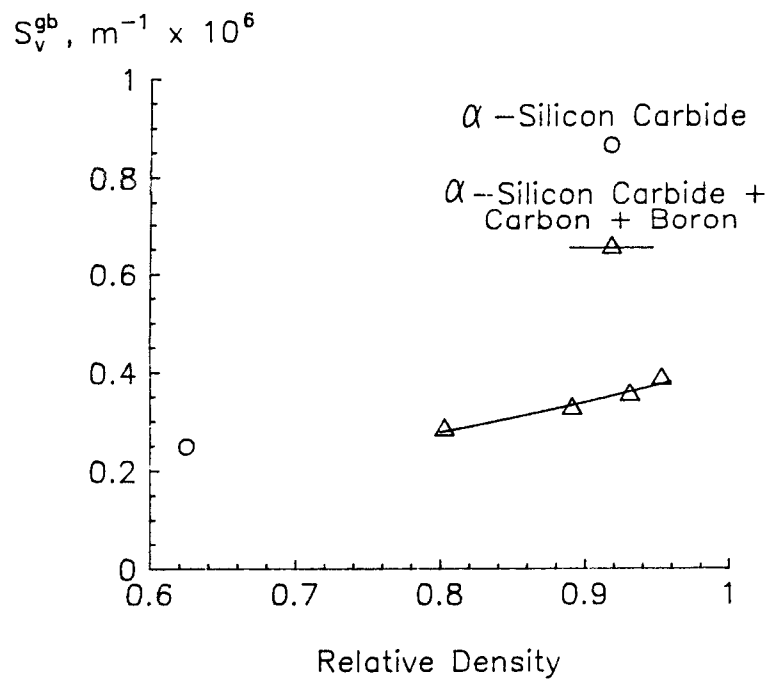


Figure 75. The grain boundary area of the SiC containing sintering aids is seen to be still increasing, indicating little or no grain growth, but this diagram provides no comparative information about the two materials.

no comparison between the two materials is possible. The grain boundary area of the carbon and boron doped samples is increasing over the entire range of densities evaluated, indicating that final stage coarsening is not yet occurring.

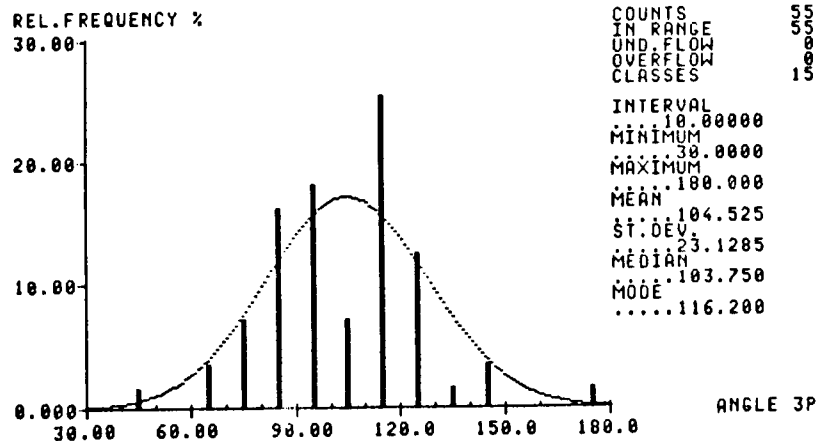
7.3 EVALUATION OF DIHEDRAL ANGLES

Prochazka has suggested that sintering of SiC may be inhibited by a high grain boundary energy to surface energy ratio,⁽⁹⁵⁾ but Greskovich and Rosolowski⁽⁴⁶⁾ found dihedral angles $\geq 100^\circ$ in pure SiC, implying no energy limitations. A very limited number of dihedral angles were measured in a sample of each material (Figure 76). While the number of angles is too small for a statistical comparison, in both cases, the mean angle size is $\geq 90^\circ$, supporting the contention that surface energy considerations are not controlling the densification of SiC.

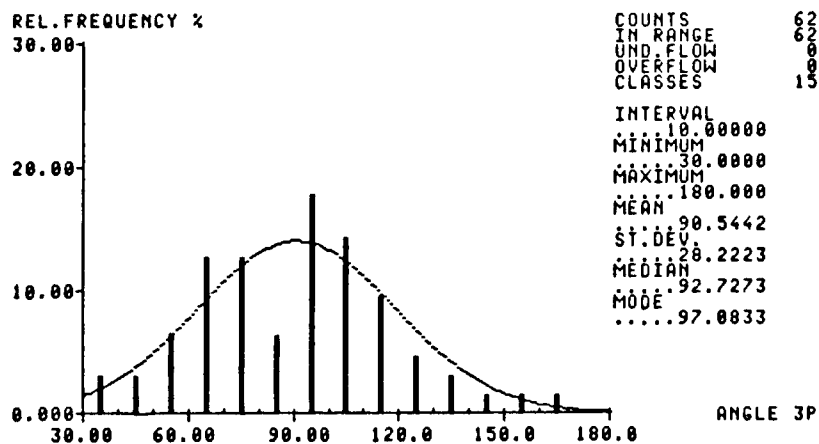
7.4 CONCLUSIONS REGARDING SiC

Silicon carbide provides a good example of the extremes of the surface area vs. density plot proposed by Burke *et al.*⁽⁵⁵⁾ The behavior of the undoped SiC which only coarsens can be clearly distinguished from that of the SiC with sintering aids which also concurrently densifies. Since nearly all of the samples are $< 90\%$ dense, the version of the diagram obtained by BET measurement of the surface area is most accurate.

It can be seen from the trajectory of the doped material that considerable early coarsening occurs; thus, if a very small final grain size is required, additional processing variations, e.g., hot pressing⁽¹⁶⁾ or hot isostatic pressing,⁽¹¹⁸⁾ will be needed in addition to sintering aids. This particular diagram



A



B

Figure 76. Histograms of dihedral angles measured on samples held 0 minutes at the sintering temperature. (A) SiC (B) SiC + C + B. In both cases angles are large enough to exclude energy considerations as a reason for the lack of densification of pure SiC.

provides little information on the behavior of the undoped material. The cluster of points at the same surface area indicates a surprising lack of additional coarsening after reaching the sintering temperature. This behavior is confirmed by the plot of surface area against sintering time. Further investigation by additional stereological methods, for instance, more detailed grain shape measurements, may help to shed light on the reasons for the lack of either densification or coarsening in this material.

No comparison of the grain boundary area changes of the two materials could be made, but it was shown that little coarsening of the grains occurs over the range of densities and sintering times evaluated for the doped SiC.

Again the difficulties in assessing coarsening behavior during the initial and intermediate stages of sintering are evident. The S_m vs. density diagram by BET analysis is easily obtained, but provides little information beyond that generally known about SiC: without sintering aids, SiC does not densify, but it can reach nearly full density with the addition of appropriate amounts of carbon and boron. Stereological techniques are obviously not applicable to materials that cannot be suitably polished and etched. Since the higher density doped SiC samples can be satisfactorily prepared, it should be possible to use both the pore/solid and the grain boundary surface area vs. density diagrams, and whatever other stereological measurements are found to be relevant to those results, to gain further understanding of the role of carbon and boron and the effect of other sintering additives on the microstructural evolution of sintered SiC.

CHAPTER 8

CONCLUSIONS

The objective of this study was to investigate experimental techniques applicable to the study of coarsening during the sintering of ceramics, the principal approach being the diagram representing the path of surface area change with densification proposed by Burke *et al.*⁽⁵⁵⁾ This diagram allows one to compare the ratio of the coarsening rate to the densification rate for different materials or processes.

In the case of Al_2O_3 , there is no evidence that the addition of MgO as a sintering aid modifies any of the diffusion processes that would change the rate of either coarsening or densification during initial or intermediate stage sintering. It is clear, however, that MgO does enhance grain boundary pinning in fully dense regions. It is also clear that, although the densification:coarsening ratio will, in the ideal case, determine the final sintered density and grain size, in the nonideal case of a typical powder compact, other factors are also significant, e.g., the packing inhomogeneities found here to be importantly affected by the presence of MgO .

In Y_2O_3 the effect of MgO was again seen to be coarsening control within fully dense regions by grain boundary pinning. Determination of the effect of MgO on the densification:coarsening ratio and further analysis was not feasible due to the apparent reactivity of Y_2O_3 with other elements present in the sintering and/or etching environments.

The difference in densification behavior of SiC with and without boron and carbon sintering aids is clearly seen in the Burke diagram. Further understanding of those differences was limited by the inability to suitably etch the undoped

specimens. However, the stereology methods should be useful in evaluating the coarsening behavior caused by different processing methods or additives in high density SiC when significant microstructural changes may occur, e.g., abnormal grain growth during the $\beta \rightarrow \alpha$ transformation.

The Burke diagram is found to be a valuable tool for an initial assessment of what is happening regarding the coarsening and densification behavior. It is especially useful in the earlier stages of sintering due to the ease of surface area measurement by BET when other techniques are unavailable or impractical, e.g., the microscopy methods that require considerable sample preparation and are inaccurate due to problems observing very small particles in porous compacts. The variation of the diagram, not previously applied to ceramics, in which grain boundary area is measured by quantitative microscopy can also provide significant information not available by other means. Both diagrams provide guidance as to the direction to look for further information. For example, in the case of Al_2O_3 , when it was seen that the significant effect of MgO was on the amount of grain boundary area, not the skeletal pore/solid surface area, analysis of the two types of grain boundaries (those connected to pores and those in fully dense regions) led to the understanding that MgO is influencing grain boundary movement in fully dense regions. Although assumptions can reasonably be made about the mechanisms involved, in this case, grain boundary pinning by solute segregation, definitive information about why the observed behavior occurs must be obtained by other means, e.g., surface analysis (Auger electron spectroscopy, secondary ion mass spectroscopy), diffusion studies, etc., beyond the scope of this thesis.

Several factors were found that may limit the usefulness of the surface area/density approach. They include: 1. Materials that readily react with other species may be difficult to characterize due to the presence of undesirable phases. More importantly, such reactive behavior may destroy the purity of the starting sample and completely mask the process of interest. 2. It may also be difficult

to prepare samples with the range of properties needed to adequately understand the effects of interest. 3. The samples must be able to be suitably polished and etched for observation.

In summary, the surface area/density diagram approach to studying coarsening behavior during sintering, while not without its difficulties, is a useful technique when suitable samples are available, and can provide information not available by other methods.

REFERENCES

1. J.E. Burke and J.H. Rosolowski, "Sintering," Chapter 10 in Treatise on Solid State Chemistry, v. 4: Reactivity of Solids, ed. N.B. Hannay, Plenum Press, New York (1976).
2. J.E. Burke, "Sintering and Microstructure Control," Chapter 18 in Chemical and Mechanical Behavior of Inorganic Materials, eds. A.W. Searcy, D.V. Ragone and U. Colombo, Wiley-Interscience, New York (1970).
3. R.L. Coble and J.E. Burke, "Sintering of Ceramics," in Progress in Ceramic Science, v. 3, ed. J.E. Burke, Pergamon, Oxford (1963) 197.
4. A.L. Stuijts, "Synthesis of Materials from Powders by Sintering," in Annual Reviews of Materials Science, v. 3, eds. R.A. Huggins, R.H. Bube and R.W. Roberts, Annual Reviews, Inc., Palo Alto (1973) 363.
5. F. Thummler and W. Thomma, "The Sintering Process," in Metallurgical Reviews 12, Metals and Metallurgy Trust, London (1967) 69.
6. H.E. Exner, "Principles of Single Phase Sintering," in Reviews on Powder Metallurgy and Physical Ceramics v. 1, ed., F.U. Lenel, Freund Publishing House, Tel Aviv (1979) 7.
7. G.C. Kuczynski, M.A. Hooten and C.F. Gibbon, eds., Sintering and Related Phenomena, Gordon and Breach, New York (1967).
8. G.C. Kuczynski, ed., Sintering and Related Phenomena, Mat. Sci. Res. 6, Plenum Press, New York (1973).
9. G.C. Kuczynski, ed., Sintering and Catalysis, Mat. Sci. Res. 10, Plenum Press, New York (1975).
10. G.C. Kuczynski, ed., Sintering Processes, Mat. Sci. Res. 13, Plenum Press, New York (1980).

11. F.R.N. Nabarro, "Deformation of Crystals by the Motion of Single Ions," in The Strength of Solids, London Physical Society, London (1948) 75.
12. C. Herring, "Diffusional Viscosity of a Polycrystalline Solid." J. Appl. Phys. 21 (1950) 437.
13. R.L. Coble, "A Model for Boundary Diffusion Controlled Creep in Polycrystalline Materials." J. Appl. Phys. 31 (1963) 1679.
14. R.W. Davidge. Mechanical Behavior of Ceramics, Cambridge University Press, Cambridge (1979).
15. F. Garofalo. Fundamentals of Creep and Creep Rupture in Metals, Macmillan, New York (1965).
16. R.L. Coble, "Mechanisms of Densification During Hot Pressing," in Sintering and Related Phenomena, Mat. Sci. Res. 6, eds. G.C. Kuczynski, N.A. Hooten and C.F. Gibbon, Gordon and Breach, New York (1967) 329.
17. F.B. Swinkels and M.F. Ashby, "A Second Report on Sintering Diagrams." Acta Met. 29 (1981) 259.
18. R.L. Coble, "Initial Sintering of Alumina and Hematite." J. Am. Ceram. Soc. 41 (1958) 55.
19. G.C. Kuczynski, "Self-diffusion in Sintering of Metallic Particles." Trans. AIME 185 (1949) 169.
20. W.D. Kingery and M. Berg, "Study of the Initial Stages of Sintering Solids by Viscous Flow, Evaporation-Condensation, and Self-Diffusion." J. Appl. Phys. 26 (1955) 1205.
21. C. Herring, "Effect of Change of Scale on Sintering Phenomena." J. Appl. Phys. 21 (1950) 301.
22. R.M. German and Z.A. Munir, "A Kinetic Model for the Reduction in Surface Area During Initial Stage Sintering," in Sintering and Catalysis, Mat. Sci. Res. 10, ed. G.C. Kuczynski, Plenum Press, New York (1975) 249.
23. D.L. Johnson and I.B. Cutler, "Diffusion Sintering: I, Initial Stage Sintering

- Models and Their Application to Shrinkage of Powder Compacts". J. Am. Ceram. Soc. 46 (1963) 541.
24. H.E. Exner, G. Petzow and P. Wellner, "Problems in the Extension of Sintering Theories to Real Systems," in Sintering and Related Phenomena, Mat. Sci. Res. 6, Plenum Press, New York (1973) 351.
 25. D.L. Johnson, "New Method of Obtaining Volume, Grain-Boundary and Surface Diffusion Coefficients from Sintering Data". J. Appl. Phys. 40 (1969) 192.
 26. R. Raj and M.F. Ashby, "On Grain Boundary Sliding and Diffusional Creep." Met. Trans. 2 (1971) 1113.
 27. R.L. Coble and T.K. Gupta, "Intermediate Stage Sintering," in Sintering and Related Phenomena, eds. G.C. Kuczynski, N.A. Hooten and C.F. Gibbon, Gordon and Breach, New York (1967) 423.
 28. R.L. Coble, "Sintering Crystalline Solids. I. Intermediate and Final Stage Sintering Models." J. Appl. Phys. 32 (1961) 787.
 29. R.L. Coble, "Intermediate-Stage Sintering: Modification and Correction of a Lattice-Diffusion Model." J. Appl. Phys. 36 (1965) 2327.
 30. R.L. Coble, "The Status of Understanding Diffusion Controlled Solid State Sintering, Hot Pressing and Creep," in Reactivity of Solids, Plenum Press, New York (1977) 669.
 31. C.H. Hsueh, A.G. Evans and R.L. Coble, "Microstructure Development During Final/Intermediate Stage Sintering - I. Pore/Grain Boundary Separation." Acta Met. 30 (1982) 1269.
 32. J.H. Rosolowski and C. Greskovich, "Analysis of Pore Shrinkage by Volume Diffusion During Final Stage Sintering." J. Appl. Phys. 44 (1973) 1441.
 33. M.F. Ashby, "A First Report on Sintering Diagrams." Acta Met. 22 (1974) 275.
 34. W.D. Kingery, H.K. Bowen and D.R. Uhlmann. Introduction to Ceramics,

Wiley, New York (1976).

35. S.J. Bennison and M.P. Harmer, "Effect of MgO on the Kinetics of Grain Growth in Al_2O_3 ." *J. Am. Ceram. Soc.* 66 (1983) C-90.
36. J.W. Cahn, "The Impurity-Drag Effect in Grain Boundary Motion." *Acta Met.* 10 (1962) 789.
37. R.J. Brook, "The Impurity-drag Effect and Grain Growth Kinetics." *Scripta Met.* 2 (1968) 375.
38. R.J. Brook, "Controlled Grain Growth," in Treatise on Material Science and Technology. Vol.2, ed. F.F.Y. Wang, Academic Press, New York (1976) 331.
39. F.A. Nichols, "Theory of Grain Growth in Porous Compacts." *J. Appl. Phys.* 37 (1966) 4599.
40. C.S. Smith, "Grains, Phases, and Interfaces: An Interpretation of Microstructure." *Trans. AIME* 175 (1948) 15.
41. D.A. Porter and K.E. Easterling. Phase Transformations in Metals and Alloys, Van Nostrand Reinhold, Wokingham, Berks. (1981).
42. R.J. Brook, "Pore-Grain Boundary Interactions and Grain Growth." *J. Am. Ceram. Soc.* 52 (1969) 56.
43. C. Greskovich and K.W. Lay, "Grain Growth in Very Porous Al_2O_3 Compacts." *J. Am. Ceram. Soc.* 55 (1972) 142.
44. K.W. Lay, "Grain Growth During Sintering," in Sintering and Related Phenomena, *Mat. Sci. Res.* 6, ed. G.C. Kuczynski, Plenum Press, New York (1973) 65.
45. N.J. Shaw and A.H. Heuer, "On Particle Coarsening During Sintering of Silicon." *Acta Met.* 31 (1983) 55.
46. C. Greskovich and J.H. Rosolowski, "Sintering of Covalent Solids." *J. Am. Ceram. Soc.* 59 (1976) 336.
47. R.M. Cannon. Seminars given at Case Western Reserve University,

Cleveland, OH, USA, June, 1980

48. M.F. Yan, "Microstructural Control of Processing of Electronic Ceramics." *Mat. Sci. & Engr.* 48 (1981) 53.
49. R.J. Brook, "Fabrication Principles for the Production of Ceramics with Superior Mechanical Properties." *Proc. Brit. Ceram. Soc.* 32 (1982) 7.
50. R.J. Brook, E. Gilbert, D. Hind and J. Vieira, "Hot Pressing Dilatometry in the Study of Sintering Mechanisms," in Sintering - Theory and Practice, *Mat. Sci. Monographs* 14, eds. D. Kolar, S. Pejovnik and M.M. Ristic, Elsevier, Amsterdam (1982) 585.
51. R.J. Brook, E. Gilbert, N.J. Shaw and U. Eisele, "Solid Solution Additives and the Sintering of Ceramics." *Powder Met.* 28 (1985) 105.
52. R.T. DeHoff, R.A. Rummel, H.P. La Buff and F.N. Rhines, "The Relationship Between Surface Area and Density in the Second-Stage Sintering of Metals," in Modern Developments in Powder Metallurgy v. 1, ed. H.H. Hauser, Plenum Press, New York (1966) 310.
53. E.H. Aigeltinger and R.T. DeHoff, "Quantitative Determination of Topological and Metric Properties During Sintering of Copper." *Met. Trans. A* 6 (1975) 1853.
54. A.W. Hey and D.T. Livey, "Sintering Data on Various Beryllium Oxide Powders," in Special Ceramics 1962, Academic Press, London (1962) 117.
55. J.E. Burke, K.W. Lay and S. Prochazka, "The Effect of MgO on the Mobility of Grain Boundaries and Pores in Aluminum Oxide," in Sintering Processes, *Mat. Sci. Res.* 13, (1980) 417.
56. J.P. Jernot, PhD Thesis, University of Caen, France, 1982.
57. J.M. Dynys, R.L. Coble, W.S. Coblenz and R.M. Cannon, "Mechanisms of Atom Transport during Initial Stage Sintering of Al_2O_3 ," in Sintering Processes, *Mat. Sci. Res.* 13, (1980) 391.

58. F.N. Rhines, R.T. DeHoff and R.A. Rummel, "Rate of Densification in the Sintering of Uncompacted Metal Powders," in Agglomeration, ed. W.A. Knepper, Interscience, London (1962) 351.
59. E.H. Exner. Private communication, April, 1983.
60. S. Prochazka. Private communication to R.J. Brook, April, 1982.
61. J.W. Cahn, "A Model for Connectivity in Multiphase Structures." Acta Met. 14 (1966) 477.
62. R.M. German and Z.A. Munir, "Morphology Relations During Surface-Transport Controlled Sintering." Met. Trans. B 6, (1975) 289.
63. R.M. German and Z.A. Munir, "Morphology Relations During Bulk-Transport Sintering." Met. Trans. A 6 (1975) 2229.
64. R.M. German and Z.A. Munir, "The Identification of the Initial-Stage Sintering Mechanism: A New Approach," in Sintering and Catalysis, Mat. Sci. Res. 10, ed. G.C. Kuczynski, Plenum Press (1975) 259.
65. R.M. German and Z.A. Munir, "Surface Area Reduction During Isothermal Sintering." J. Am. Ceram. Soc. 59 (1976) 379.
66. E.R. Weibel. Stereological Methods. vol. 1. Practical Methods for Biological Morphometry, Academic Press, London (1979).
67. R.T. DeHoff and E.H. Aigeltinger, "Experimental Quantitative Microscopy with Special Applications to Sintering," in Perspectives in Powder Metallurgy 5, ed. J.S. Hirschhorn, Plenum Press, New York (1970) 81.
68. E.H. Aigeltinger and H.E. Exner, "Stereological Characterization of the Interaction Between Interfaces and its Application to the Sintering Process." Met. Trans. A 8 (1977) 421.
69. R.L. Coble, "Sintering Crystalline Solids. II. Experimental Test of Diffusion Models in Powder Compacts." J. Appl. Phys. 32 (1961) 793.
70. J.G.J. Peelen, "Influence of MgO on the Evolution of the Microstructure of Al_2O_3 ," in Sintering and Catalysis, Mat. Sci. Res. 10, ed., G.C. Kuczynski,

Plenum Press, New York (1975) 443.

71. J.G.J. Peelen, Alumina: Sintering and Optical Properties. PhD Thesis, Technical University of Eindhoven, The Netherlands (1977).
72. W.C. Johnson and D.F. Stein, "Additive and Impurity Distributions at Grain Boundaries in Sintered Alumina." J. Am. Ceram. Soc. 58 (1975) 485.
73. D.R. Clarke, "Grain Boundary Segregation in an MgO-Doped Al_2O_3 ." J. Am. Ceram. Soc. 63 (1980) 339.
74. A.H. Heuer, "The Role of MgO in the Sintering of Alumina." J. Am. Ceram. Soc. 62 (1979) 317.
75. M.J. Bannister, "Comment on 'The Role of MgO in the Sintering of Alumina'." J. Am. Ceram. Soc. 63 (1980) 229.
76. A.H. Heuer, "Reply to 'Comment on 'The Role of MgO in the Sintering of Alumina'.'" J. Am. Ceram. Soc. 63 (1980) 230.
77. S.J. Bennison and M.P. Harmer, "Grain Growth Kinetics for Alumina in the Absence of a Liquid Phase." J. Am. Ceram. Soc. 68 (1985) C22.
78. A.E. Paladino and R.L. Coble, "Effect of Grain Boundaries on Diffusion-Controlled Processes in Aluminum Oxide." J. Am. Ceram. Soc. 46 (1963) 133.
79. M.P. Harmer and R.J. Brook, "The Effect of MgO Additions on the Kinetics of Hot Pressing in Al_2O_3 ." J. Mat. Sci. 15 (1980) 3017.
80. C. Monty and J. Le Duigou, "The Influence of the Addition of MgO on the Surface Mass Transport of Alumina." High Temp. - High Press. 14 (1982) 709.
81. R.A. LeFever and J. Matsko, "Transparent Yttrium Oxide Ceramics." Mat. Res. Bull. 2 (1967) 865.
82. C. Greskovich and J.P. Chernoch, "Improved Polycrystalline Ceramic Lasers." J. Appl. Phys. 45 (1974) 4495.
83. W.H. Rhodes and J. Reid, "Transparent Yttria Ceramics and Method for

- Producing Same." US Patent #4,098,612 (1978).
84. L.A. Brissette, P.L. Burnett, R.M. Spriggs and T. Vasilos, "Thermomechanically Deformed Y_2O_3 ." J. Am. Ceram. Soc. 49 (1966) 165.
 85. S.K. Dutta and G.E. Gazza, "Transparent Y_2O_3 by Hot-Pressing." Mat. Res. Bull. 4 (1969) 791.
 86. L.R. Furlong and L.P. Domingues, "Sintering of Yttrium Oxide." Bull. Am. Ceram. Soc. 45 (1966) 1051.
 87. P.J. Jorgensen and R.C. Anderson, "Grain-Boundary Segregation and Final-Stage Sintering of Y_2O_3 ." J. Am. Ceram. Soc. 50 (1967) 553.
 88. G. Toda, I. Matsuyama and Y. Tsukuda, "Method for Producing Highly Pure Sintered Polycrystalline Yttrium Oxide Body Having High Transparency." US Patent # 3,873,657 (1975).
 89. W. H. Rhodes, "Transparent Yttria Ceramics and Method for Producing Same." US Patent # 4,115,134 (1978).
 90. W.H. Rhodes, "Controlled Transient Solid Second-Phase Sintering of Yttria." J. Am. Ceram. Soc. 64 (1981) 13.
 91. W.H. Rhodes and J. Reid, "Transparent Yttria Ceramics Containing Magnesia or Magnesium Aluminate." US Patent # 4,174,973 (1979).
 92. "MgO - Y_2O_3 Phase Diagram." Phase Diagrams for Ceramists v. IV, eds., R.S. Roth, T. Negas and L.P. Cook, Am. Ceram. Soc., Columbus, OH (1981) 101.
 93. S. Prochazka, "Sintering of Silicon Carbide," in Ceramics for High-Performance Applications, eds., J.J. Burke, A.E. Gorum and R.N. Katz, Brook Hill, Chestnut Hill, MA (1974) 239.
 94. S. Prochazka and R.M. Scanlan, "Effect of Boron and Carbon on Sintering of SiC." J. Am. Ceram. Soc. 58 (1975) 72.
 95. S. Prochazka, "The Role of Boron and Carbon in the Sintering of Silicon Carbide," in Special Ceramics 6, ed., P. Popper, Brit. Ceram. Res. Assoc.,

- Stoke-on-Trent (1975) 171.
96. E.R. Maddrell, "Pressureless Sintering of Silicon Carbide." *J. Mat. Sci. Lett.* 6 (1987) 486.
 97. A.H. Heuer, G.A. Fryburg, L.U. Ogbuji, T.E. Mitchell and S. Shinozaki, " $\beta \rightarrow \alpha$ Transformation in Polycrystalline SiC: I, Microstructural Aspects," *J. Am. Ceram. Soc.* 61 (1978) 406.
 98. G.R. Sawyer and T.F. Page, "Microstructural Characterization of 'REFEL' (reaction-bonded) Silicon Carbides." *J. Mat. Sci.* 13 (1978) 885.
 99. J.B. Hurst and M.L. Millard, "Evaluation of α -SiC Sintering Using Statistical Methods." *J. Am. Ceram. Soc.* 68 (1985) C-178.
 100. S.K. Roy and R.L. Coble, "Solubilities of Magnesia, Titania, and Magnesium Titanate in Aluminum Oxide." *J. Am. Ceram. Soc.* 51 (1968) 1.
 101. R.C. Anderson, "Thoria and Yttria," in High Temperature Oxides, ed., A.M. Alper, Academic Press, London (1970) 1.
 102. "Standard Test Method for Water Absorption, Bulk Density, Apparent Specific Gravity of Fired Whiteware Products: ASTM C 373-72." *Am. Soc. for Testing and Materials*, Philadelphia.
 103. S. Brunauer, P. Emmett and E. Teller, "Adsorption of Gases in Multimolecular Layers." *J. Am. Chem. Soc.* 60 (1938) 309.
 104. T. Allen, "Gas Adsorption," in Particle Size Measurement, 3rd ed., Chapman and Hall, London (1981) 465.
 105. H.E. Exner. Private communication. January, 1983.
 106. S. Prochazka. Private communication. March, 1984.
 107. E.E. Underwood. Quantitative Stereology, Addison-Wesley, Reading, MA (1970).
 108. R.T. DeHoff and F.N. Rhines. Quantitative Microscopy, McGraw-Hill, New York (1968).
 109. E.E. Underwood, A.R. Colcord and R.C. Waugh, "Quantitative Relationships

- for Random Microstructures," in Ceramic Microstructures, eds., R.M. Fulrath and J.A. Pask, Wiley, New York (1968) 25.
110. E. Gilbert. Computer program to generate stereology grid, Leeds (1982).
111. MOP - Videoplan Operator's Manual, Kontron Elektronik GmbH, Eching (1983).
112. P.G. Shewmon, "The Movement of Small Inclusions in Solids by a Temperature Gradient." Trans AIME 230 (1964) 1134.
113. Private communication to R.J. Brook.
114. F.F. Lange and M.M. Hirlinger, "Hindrance of Grain Growth in Al_2O_3 by ZrO_2 Inclusions." J. Am. Ceram. Soc. 67 (1984) 164.
115. A.G. Evans, "Considerations of Inhomogeneity Effects in Sintering." J. Am. Ceram. Soc. 65 (1982) 497.
116. M. Hillert, "On the Theory of Normal and Abnormal Grain Growth." Acta Met. 13 (1965) 227.
117. W.H. Rhodes. Private communication. September, 1984.
118. S. Dutta, "Strength Optimization of α -SiC by Improved Processing." NASA CP-2427, NASA, Cleveland, OH. (1986) 89.



National Aeronautics and
Space Administration

Report Documentation Page

1. Report No. NASA TM-100235	2. Government Accession No.	3. Recipient's Catalog No.	
4. Title and Subtitle Structure and Grain Coarsening During the Processing of Engineering Ceramics		5. Report Date November 1987	
		6. Performing Organization Code	
7. Author(s) Nancy J. Shaw		8. Performing Organization Report No. E-3860	
		10. Work Unit No. 505-63-01	
9. Performing Organization Name and Address National Aeronautics and Space Administration Lewis Research Center Cleveland, Ohio 44135-3191		11. Contract or Grant No.	
		13. Type of Report and Period Covered Technical Memorandum	
12. Sponsoring Agency Name and Address National Aeronautics and Space Administration Washington, D.C. 20546-0001		14. Sponsoring Agency Code	
15. Supplementary Notes This report was a thesis submitted in fulfillment of the requirements for the degree of Doctor of Philosophy to The University of Leeds, Dept. of Ceramics, Leeds LS2 9JT, United Kingdom in October 1987.			
16. Abstract In the present work, studies have been made of three host/studies systems - Al_2O_3 , Y_2O_3/MgO , and $SiC/C/B$ - both to explore a surface area/density diagram approach to examining the coarsening processes during sintering and to explore an alternative coarsening parameter, namely, the grain boundary surface area (raising it at a given value of the density) and not the pore surface area; therefore, pinning of the grain boundaries by solid-solution drag is the only function evidenced by these results. The importance of such pinning even at densities as low as 75 percent of theoretical is linked to the existence of microstructural inhomogenities. The early stages of sintering of Y_2O_3 powder have been examined using two different techniques, BET surface area analysis and direct observation of the particles using transmission electron microscopy. Each technique has given some insight into the process occurring and, used together, they have provided some indication of the effect of MgO on coarsening during sintering. Attempts to further elucidate effects of MgO on the coarsening behavior of Y_2O_3 by the surface area/density diagram approach were unsuccessful due to masking effects of contaminating reactions during sintering and/or thermal etching. The behavior of the undoped SiC which only coarsens can be clearly distinguished by the surface area/density diagram from that of $SiC/C/B$ which also concurrently densifies. Little additional information was obtainable by this method due to unfavorable sample etching characteristics. The advantages, disadvantages, and difficulties of application of these techniques to the study of coarsening during sintering are discussed.			
17. Key Words (Suggested by Author(s)) Sintering; Quantitative Microscopy; Alumina; Silicon Carbide; Stereology; Coarsening		18. Distribution Statement Unclassified - Unlimited Subject Category 27	
19. Security Classif. (of this report) Unclassified	20. Security Classif. (of this page) Unclassified	21. No of pages 169	22. Price* A08